# 論文 / 著書情報
# Article / Book Information

| | |
|---|---|
| 題目(和文) | |
| Title(English) | Metallization of 3D Complex Polymer Structure by Supercritical Carbon Dioxide Catalyzation |
| 著者(和文) | CHENG PO-WEI |
| Author(English) | Po-Wei Cheng |
| 出典(和文) | 学位:博士(工学),<br>学位授与機関:東京工業大学,<br>報告番号:甲第12550号,<br>授与年月日:2023年9月22日,<br>学位の種別:課程博士,<br>審査員:曽根 正人,CHANG TSO-FU,細田 秀樹,木村 好里,多田 英司,田原 正樹,HSU YUNG JUNG |
| Citation(English) | Degree:Doctor (Engineering),<br>Conferring organization: Tokyo Institute of Technology,<br>Report number:甲第12550号,<br>Conferred date:2023/9/22,<br>Degree Type:Course doctor,<br>Examiner:,,,,,, |
| 学位種別(和文) | 博士論文 |
| Type(English) | Doctoral Thesis |

# Metallization of 3D Complex Polymer Structure by Supercritical Carbon Dioxide Catalyzation

Department of Materials Science and Engineering

Tokyo Institute of Technology

**Po–Wei Cheng**

May, 2023

# *Table of content*

CHAPTER 1

# *General introduction*

## 1.1 Background

### *1.1.1 Rapid prototyping and flexible electronic components*

Rapidly manufacturing electronic components is pursued in this generation. The demands of applications like integration circuits [1-1], Physical sensor [1-2], wearable devices [1-3], and bioengineering [1-4]. One strategy is integration of various functional materials to realize a multi-functional composite material possessing the desired properties. One common constituent in the composite material is a polymer-based material, and examples of the polymers are polyimide [1-5], polyamide 6 [1-6], polypropylene [1-7], 3D-printed polymer [1-8,1-9] and polyethylene terephthalate (PET) [1-10–1-12]. Three-dimensional (3D)-printed polymer has attracted a great attention due to its high degree of freedom and precise resolution in the design of complex 3D structures. 3D-printing technology is also known as rapid prototyping. The demand structure can be rapidly printed without the complex steps in conventional mold production. Since the invention of the first 3D printer by Dr. Hideo Kodama in 1981 [1-13], a variety of 3D printers have been released for specific requirements continuously.

3D printers could be distinguished by the basic working methods such as the

material jetting and material with light (UV: ultraviolet) exposed. Examples of the material jetting type are Fused Deposition Modeling (FDM) and Direct Ink Writing (DIW) [1-14]. FDW is commonly and widely used. The first step in FDW is melting the thermoplastic material from a solid state to a molten state, and consequently the material is injected out through a nozzle to form successive object layers. The type of material with light (UV) exposed would form a layer to layer structure, and the examples are PolyJet 3D printing, Stereolithography (SLA), Digital Light Processing (DLP) and Liquid-Crystal Display (LCD) UV-curing printer as shown in Fig. 1.1. The LCD UV-Curing 3D printers would construct the layer to layer structure by exposing the printed layer to UV light to harden and maintain the shape of the structure, then the next layer would be printed on top of the solidified layer [1-15].

On the other hand, the demand for flexible functional materials is also high in electronic devices. PET (polyethylene terephthalate) is a promising candidate because of the high chemical stability, biocompatibility, flexibility, low cost and decent mechanical strengths [1-16]. The high chemical stability is a double-edged sword, which make it difficult to integrate with other functional materials.

### *1.1.2 Methodology for the integration of material for the applications*

Most polymer materials are electrically non-conductive which leads to difficulties in the integration. Also, electrical conductivity is a fundamental property for conductors in electronic devices. A number of integration processes are developed to combine electrically non-conductive materials with various functional materials, such as sputtering [1-17], ink printing [1-18], chemical vapor deposition [1-19], chemical fluid deposition [1-20,1-21], cold-spray coating [1-22] and electroless plating processes [1-23–

1-29]. Among all of these processes, the most effective integration process is suggested to be the electroless plating process. This is mostly because of its low cost, moderate deposition rate and the ability to deposit various metal coatings on surfaces having complex structures, which are all advantageous in rapid fabrication of electronic components.

### *1.1.3 Conventional electroless plating*

Electroless plating is also known as chemical or autocatalytic plating [1-30]. It is often compared with electroplating. In electroplating, the electrical current is driven by an external power supply, hence the substrate has to be electrically conductive. In electroless plating, the electrical current to carry out the reduction reaction is generated by reducing agents instead of an external power supply. This then allows electrodeposition of materials on an electrically non-conductive substrate.

In electroless plating, the reduction reaction involves the autocatalytic conversion of metastable redox pairs, created by dissolved reducing agents and metal complexes in the solution. This process allows the deposition of metals on a surface in a conformal manner. The overall reaction involves two coupled redox reactions: the oxidation of a reducing agent and the reduction of a metal complex [1-31] (as illustrated in Fig. 1-2). There are three common steps in an electroless plating process: a pretreatment step, a catalyzation step, and a metal deposition step. Purpose of the pretreatment step are cleaning and roughening of the substrate surface to enhance interactions between the substrate surface and the deposited metal coating.

In the catalyzation step, catalyst seeds needed for the later metal deposition step are formed on the electrically non-conductive substrate surface. Conventionally, the

catalyst seeds are deposited by treating the surface with solutions containing $Sn^{2+}$ ions ($SnCl_2$) and $Pd^{2+}$ ($PdCl_2$) ions successively . In this way, $Sn^{2+}$ ions adsorbed on the surface would be oxidized to allow reduction of the $Pd^{2+}$ ions to form palladium catalyst seeds on the surface, the following reaction:

$$Sn^{2+} + Pd^{2+} \rightarrow Sn^{4+} + Pd \qquad (1)$$

Hence, roughening of the surface in the pretreatment step is critical to improve the interaction.

Then, in the metal deposition step, with presences of reducing agents in the solution, reduction of the metal ions would be initiated from the catalyst seeds and gradually form a metal coating covering the entire surface, as shown in Fig.1-3. The general composition of the electroless plating solution includes (1) metal ions ( Ni, Pt, and Au) to be reduced, (2) reducing agents ( hypophosphite, and hydrazine) act as the source of the electrochemical energy to trigger reduction of the metal ions, (3) complexing agents (ethylenediaminetetraacetic acid (EDTA) ) to ensure the reduction reaction only takes place on the catalyst surface, (4) bath stabilizer (sulphate, nitrate and chloride) to stabilize the bath from decomposition by shielding the catalytically active deposition [1-32].

The catalyst (Ni, Cu, Pd, Ag, Au) plays a crucial role in electroless plating reaction [1-33]. The catalyst is responsible for initiating and facilitating the redox reactions that lead to the deposition of the metal on the substrate. Transition metals are often used as the catalyst in electroless plating because they possess unpaired d-electrons or empty d-orbitals that can facilitate the adsorption of reaction molecules during catalysis. This interaction can lead to the activation of chemical bonds and the reduction of the activation energy required for the reaction to occur [1-34].

(1) Ni-P metallization

Ni-P has unique properties like excellent corrosion, wear resistance, ductility, lubrication, soldering, and electrical conductivity [1-35], and these properties makes it widely accepted in engineering applications. Reactions involved in Ni-P electroless plating are provide in the following [1-36]:

$$Ni^{2+}_{ads} + H_2PO^-_{2\,ads} + H_2O \rightarrow Ni^0 + 3H^+ + HPO^{2-}_3 \quad (2)$$

$$H_2PO^-_{2\,ads} + H_2O \rightarrow HPO^{2-}_3 + H^+ + 2H_{ads} \quad (3)$$

$$H_2PO^-_{2\,ads} + H_{ads} \rightarrow P^0 + H_2O + OH^- \quad (4)$$

$$2H_{ads} \rightarrow H_2 \quad (5)$$

The phosphorus content can be controlled to form different properties of deposited Ni-P. They can be classified into [1-37]:

(i) 3-5% P (low phosphorus). Sufficient wear resistance and corrosion resistance in concentrated caustic soda.

(ii) 6-9% P (medium phosphorus). Eligible corrosion protection and abrasion resistance for most applications.

(iii) 10-14% P (high phosphorus). Excellent ductile, high corrosion resistance against chlorides, and simultaneous mechanical stress.

Additionally, Ni-P is widely regarded as the most suitable sacrificial metal layer for the electroless plating of Au. Doped phosphorus can enhance Ni-P alloys by bonding free electrons around nickel atoms, causing a shift from a metallic to an amorphous crystal structure. This enhances the electronegativity of the phosphorus atoms, allowing them to attract oxidative cations such as $Au^{+3}$ [1-38].

(2) Au metallization

Gold is a highly sought-after metal due to its unique physical, chemical, optical, electronic and catalytic properties [1-39]. With the growing demand for gold in nanotechnology, effectively utilizing gold is a crucial issue. Electroless gold plating process occurs through two mechanisms: gold cementation by immersion replacement of the substrate metal, and gold reduction by a catalytically oxidized reducing agent. Gold cementation solutions do not contain dissolved reducing agents, and as a result, the thickness of the gold film in such solutions typically does not exceed 0.1 μm. In contrast, solutions with a reducing agent enable the deposition of thicker and non-porous gold films [1-40]. In the conventional gold deposition, $CN^-$ is commonly used as a complexing agent for $Au^+$ to form $KAu(CN)_2$. However, the use of cyanide as a complexing agent in these baths is highly toxic. As a result, non-cyanide baths are developed to replace $KAu(CN)_2$, and examples of the alternatives are Au(III) chloride complex ($KAuCl_4$) and Au(III)–DMH complex. The reaction equation is provided in the following [1-41]:

$$2Au^{3+} + 3Ni \rightarrow 3Ni^{2+} + 2Au \quad (6)$$

(3) Pt metallization

Platinum can be prepared with a well-defined nanostructure and has gathered significant scientific attention due to its intriguing properties for a multitude of applications, such as highly active catalysts [1-42], actuators [1-43], nanodevices [1-44], electrodes [1-45], and high biocompatibility sensors [1-46]. Electroless Pt plating is typically achieved using either hydrazine ($N_2H_4$) or borohydride as the reducing agent, with $N_2H_4$ being the most commonly used due to its ability to produce a Pt metallization film without any co-deposition. The Pt ion source in the metallization

solution is often $(NH_3)_2Pt(NO_2)_2$, which has been widely utilized for this purpose. The reaction equation is provided in the following :

$$2(NH_3)_2Pt(NH_3)_2 + N_2H_4 \cdot H_2O \rightarrow 2Pt + 5N_2 + 9H_2O \quad (7)$$

*1.1.4 Supercritical carbon dioxide assisted electroless plating*

In the conventional pretreatment and catalyzation steps, toxic and strong acids are used to treat the polymer surfaces. The polymer substrates often suffer undesired damage and contamination by the strong acids. In addition, the interaction between the polymer substrates and metal coating is insufficient to ensure proper reliability of the metallized polymer. A catalyzation method utilizing supercritical carbon dioxide (sc-$CO_2$) as the solvent is developed to eliminate usages of the strong acids and enhancement of the interaction [1-47].

Supercritical carbon dioxide (sc-$CO_2$) is a state of carbon dioxide when both the temperature and pressure are above its critical point (31.0°C, 7.4 MPa) [1-48]. Illustration of the apparatus is shown in Fig. 1-4. Supercritical fluids exhibit physical properties (Density, Diffusion, Viscosity) that are intermediates between those of gases and liquids, and these properties can be easily tuned by controlling the pressure and temperature [1-49]. Additionally, sc-$CO_2$ offers several advantages over non-polar organic solvents, such as great self-diffusivity, low viscosity, zero surface tension, and non-toxicity. As a result, sc-$CO_2$ has become a popular substitute for non-polar organic solvents in electroless plating. In the sc-$CO_2$ assisted electroless plating process, the pretreatment step is not needed since sc-$CO_2$ used in the catalyzation step is effective in cleaning the substrate surface, and the interaction between the substrate and the metal coating is enhanced by having catalyst seeds embedded inside the polymer substrate to anchor the metal coatings

on the substrate surface. The mechanism is similar to the root system of plants, which huge trees stand tightly on the ground because of the roots extending deep into the soil in Fig. 1-5.

### *1.1.5 Crystallinity of polymers*

Crystallinity is an important factor that affects the properties and behavior of polymers. The degree of crystallinity refers to the extent to which a polymer's molecular chains are arranged in an ordered, crystalline structure. Here are some ways in which crystallinity can impact polymers [1-50–1-54]:

1. Mechanical properties

   Crystalline regions in polymers provide additional strength and stiffness compared to amorphous regions. As the degree of crystallinity increases, the polymer tends to have higher tensile strength, modulus of elasticity, and resistance to deformation. This is because the regular packing of polymer chains in crystalline regions allows for more efficient stress transfer.

2. Thermal properties

   Crystalline regions have a higher melting point and heat resistance compared to amorphous regions. Polymers with higher crystallinity generally exhibit higher melting temperatures, greater thermal stability, and improved resistance to thermal degradation. The presence of crystalline domains can also affect the thermal expansion behavior of the polymer.

3. Optical properties

Crystalline regions in polymers can affect their optical properties, such as transparency, refractive index, and birefringence. The arrangement of polymer chains in the crystalline structure can lead to variations in light transmission and scattering, resulting in different optical characteristics.

4. Barrier properties

Crystalline regions can hinder the diffusion of gases and liquids through the polymer matrix, thereby improving its barrier properties. Polymers with higher crystallinity tend to have lower permeability to gases and liquids, making them suitable for applications requiring gas or moisture barriers.

5. Processing and mechanical behavior

The presence of crystalline regions can affect the processing behavior of polymers. Higher crystallinity can result in increased melt viscosity, which may impact processing methods such as molding or extrusion. Additionally, the presence of crystalline regions can influence the polymer's response to mechanical stress, including its elasticity, creep resistance, and toughness.

It's important to note that the crystallinity of a polymer can be influenced by various factors, including polymer composition, processing conditions, cooling rates, and post-treatment methods. By controlling these factors, it is possible to tailor the crystallinity and, subsequently, the properties of the polymer to meet specific application requirements.

## 1.2 Thesis objective

With the increasing demand for electronic components, there is a growing emphasis on accelerating the manufacturing process. Composite materials have emerged as the preferred choice in this endeavor. However, the compatibility issues between commonly used polymers and metals as composite materials remain a challenge. Among various integration techniques, electroless plating has been identified as holding the highest potential due to its ability to provide uniform coatings on complex surfaces, easy control of coating rate, and relatively low cost. However, concerns still exist regarding the adhesion and mechanical properties of metallic polymer composites for practical applications.

Recently, several methods have been proposed to enhance the adhesive properties of metallized polymers. The hydrophobic nature of polymers such as PET and 3D-printed polymers poses a challenge for interactions between metal ions in electroless plating solutions. To address this issue, chemical solutions rich in hydrophilic functional groups, such as hydroxyl and carbonyl groups, are used to improve adhesion [1-55–1-58]. By immersing the hydrophobic surface in a hydrophilic chemical solution, the surface properties can be modified from hydrophobic to hydrophilic. This modification enables better interaction with the electroless plating solution, resulting in improved adhesion between the metal and polymer substrate. However, when the polymer substrates have low chemical resistance, there is still a concern regarding the potential risk of damage when using a chemical solution.

In this thesis, my main focus was on sc-$CO_2$ assisted electroless plating, where I proposed specific approaches to address the aforementioned issues. I explored the

application potential of sc-$CO_2$ assisted electroless plating by depositing different metals such as Ni-P, Au, and Pt on 3D-printed polymers and PET materials.

### 1.3 Thesis overview

To accomplish the objectives of this thesis, the following chapters are established.

**In Chapter 1**, backgrounds of 3D-printed polymer and PET, conventional electroless plating, sc-$CO_2$ assisted electroless plating. After the background, the motivation and objective of this thesis are described.

**In Chapter 2**, extending the results of chapter 2, sc-$CO_2$ assisted functionalization of PET toward flexible catalytic electrodes was fabricated, the Au/Ni-P/PET composite material was achieved due to great contribution of sc-$CO_2$ assisted catalyzation.

**In Chapter 3**, the mechanical properties of Pt/PET assisted by sc-$CO_2$-catalyzation were demonstrated. The fracture strength was determined by measuring the stress value at the point of short circuit. This method of evaluation is more relevant to the performance of flexible electronic components.

**In Chapter 4**, Ni-P/3D-printed polymer structures was achieved by sc-$CO_2$-assisted electroless plating process to demonstrate the potential for rapid fabrication of electronic components.

**In Chapter 5**, extend the result of chapter 5, further mechanical properties were discussed. Because gold possesses better chemical stability and the smaller ductility difference between gold and 3D-printed polymers than between Ni-P and 3D-rinted polymers. Au/Ni-P/3D-printed polymer is a promising material toward additive manufacturing of electronic components.

**In Chapter 6**, the surface roughness difference with 3D-printed structures was utilized to achieve pattern in electroless plating. The circuit integrated with electronic components is possible to be fabricated.

**In Chapter 7**, effects of the sc-$CO_2$ assisted catalyzation process on the fabrication of Ni-P/PET composite films are demonstrated through crystallinity to discuss the mechanism of diffusion. The focus on the crystallinity changes of sc-$CO_2$ treated PET and sc-$CO_2$ treated PET with organometallic compounds is described.

**In Chapter 8**, general conclusions and the future work of this study are provided.

## 1.4 Figures

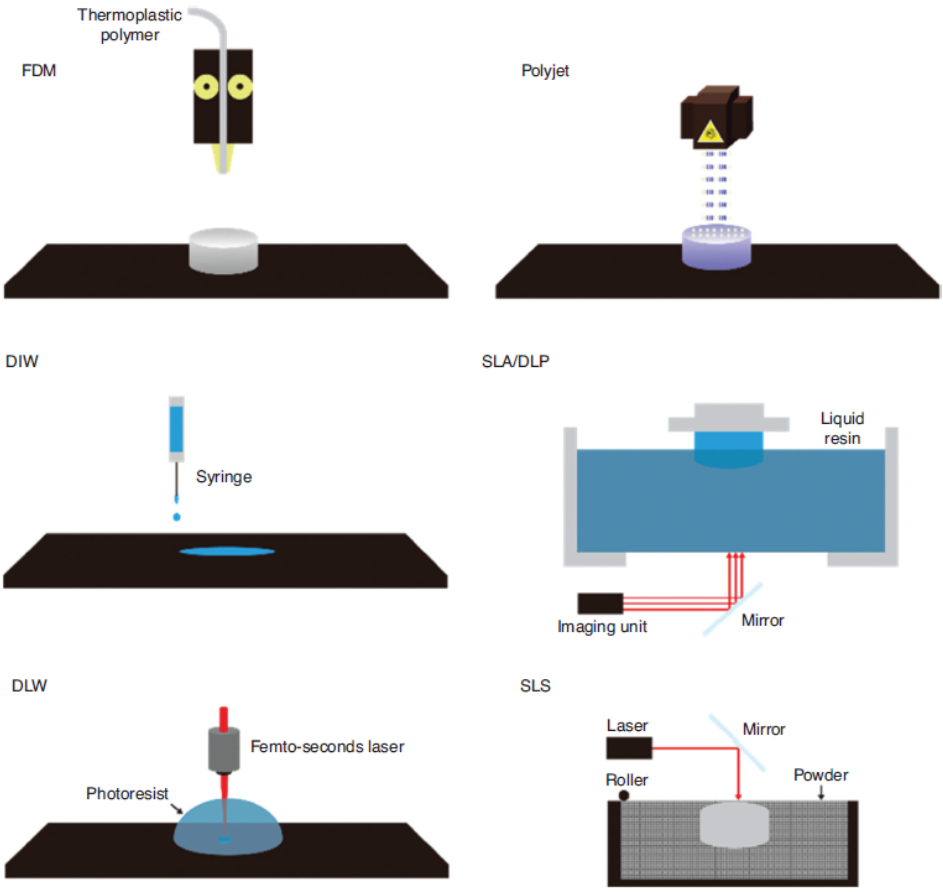


**Figure 1-1**. Schematics of the 3D printing methods: Fused deposition modeling (FDM), PolyJet (or Material jetting), Direct ink writing (DIW), Stereolithography(SLA)/Digital light projector (DLP), Direct laser writing (DLW), Selective Laser Sintering (SLS) [1-15].

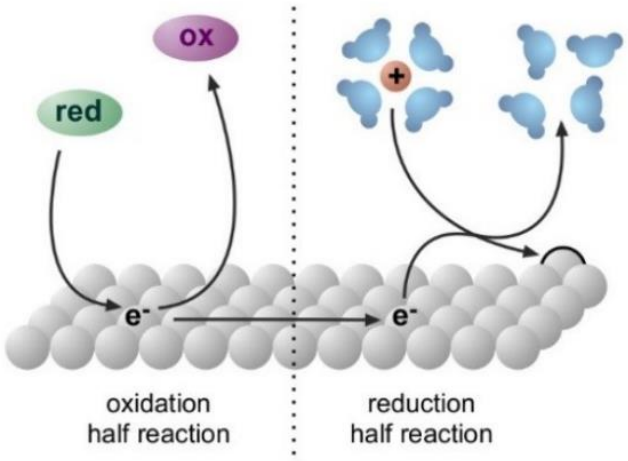


**Figure 1-2.** The overall reaction of electroless plating involves two coupled redox reactions [1-31].

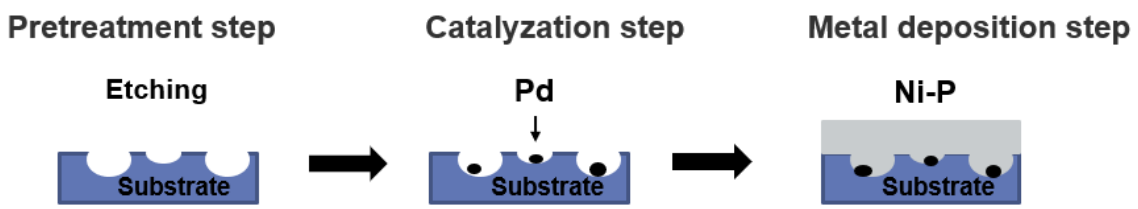


**Figure 1-3.** Conventional electroless plating process.

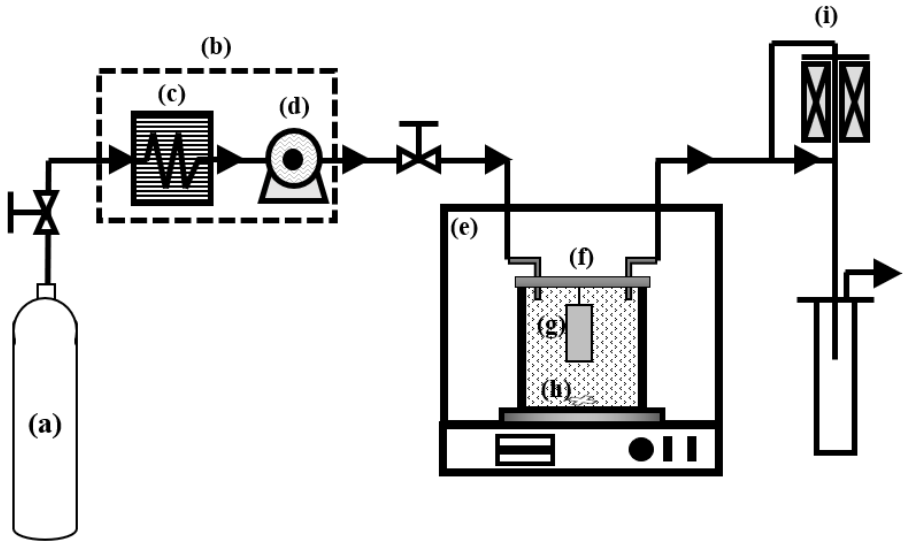


**Figure 1-4.** High pressure apparatus: (a) $CO_2$ gas tank, (b) $CO_2$ liquidization unit, (c) compressor, (d) high pressure pump, (e) box oven, (f) reaction cell, (g) substrate, (h) magnetic stirrer and (i) back pressure regulator

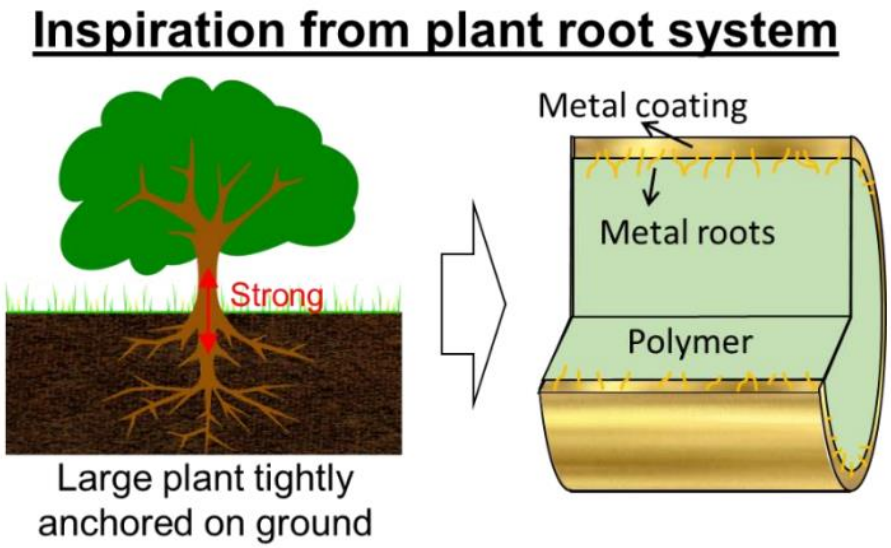


**Figure 1-5.** Metallization of polymer inspired by the root system of plants.

## 1.5 References


[1-1] A. Gorelov, F. Vasilyev, 3D printed solder masks for printed circuit boards. Rapid Prototype J. 25 (2019) 1224. http://dx.doi.org/10.21533/pen.v9i4.2337

[1-2] T.Q. Trung, N.-E. Lee, Flexible and Stretchable Physical Sensor Integrated Platforms for Wearable Human-Activity Monitoringand Personal Healthcare. Adv. Mater. 28 (2016) 4338-4372. https://doi.org/10.1002/adma.201504244

[1-3] Y. Chen, Z. Wang, R. Xu, W. Wang, D. Yu, A highly sensitive and wearable pressure sensor based on conductive polyacrylonitrile nanofibrous membrane via electroless silver plating. J. Chem. Eng. 394 (2020) 12490. https://doi.org/10.1016/j.cej.2020.124960

[1-4] H.E. Jazayeri, M. Rodriguez-Romero, M. Razavi, M. Tahriri, K. Ganjawalla, M. Rasoulianboroujeni, M.H. Malekoshoaraie, K. Khoshroo and L. Tayebi, The cross-disciplinary emergence of 3D printed bioceramic scaffolds in orthopedic bioengineering. Ceram. Int. 44 (2018) 1. https://doi.org/10.1016/j.ceramint.2017.09.095

[1-5] T.-F.M. Chang, C.-C. Wang, C.-Y. Yen, S.-H. Chen, C.-Y. Chen, M. Sone, Metallization of polyimide films with enlarged area by conducting the catalyzation in supercritical carbon dioxide. Microelectron. Eng. 153 (2016) 1–4. https://doi.org/10.1016/j.mee.2015.12.006

[1-6] H. Adachi, K. Taki, S. Nagamine, A. Yusa, M. Ohshima, Supercritical carbon dioxide assisted electroless plating on thermoplastic polymers. J. Supercrit. Fluids 49 (2009) 265–270. https://doi.org/10.1016/j.supflu.2008.12.010

[1-7] S. Tengsuwan, M. Ohshima, Supercritical carbon dioxide-assisted electroless nickel plating on polypropylene—The effect of copolymer blend morphology

on metal–polymer adhesion. J. Supercrit. Fluids 85 (2014) 123–134. https://doi.org/10.1016/j.supflu.2013.11.012

[1-8] S.C. Joshi, A.A. Sheikh, 3D printing in aerospace and its long-term sustainability. Virtual Phys Prototyp. 10 (2015) 175. https://doi.org/10.1080/17452759.2015.1111519

[1-9] P.-W. Cheng, C.-Y. Chen, T. Ichibayashi, T.-F.M. Chang, M. Sone, S. Nishimura, Metallization of 3D-printed polymer structures via supercritical carbon dioxide-assisted electroless plating. MRS Commun. 11 (2021) 278-282. https://doi.org/10.1557/s43579-021-00022-2

[1-10] E. Barnard, J.J.R. Arias, W. Thielemans, Chemolytic depolymerisation of PET: a review. Green Chem. 23 (2021) 3765-3789. https://doi.org/10.1039/D1GC00887

[1-11] M. Mitsumoto, C.-Y. Chen, W.-T. Chiu, T.-F.M. Chang, Y. Watanabe, A. Jinno, H. Kurosu, M. Sone. Supercritical carbon dioxide-assisted platinum metallization of polyethylene terephthalate textile toward wearable device, Micro Nano Eng. 15 (2022) 100132. https://doi.org/10.1016/J.MNE.2022.100132

[1-12] P.-W. Cheng, C.-Y. Chen, T. Ichibayashi, T.-F.M. Chang, M. Sone, S. Nishimura, Supercritical carbon dioxide-assisted functionalization of polyethylene terephthalate (PET) toward flexible catalytic electrodes. J. Supercrit. Fluids. 180 (2022) 105455. https://doi.org/10.1016/J.SUPFLU.2021.105455.

[1-13] C. A.G. Lengua MD, History of Rapid Prototyping. In: Farooqi, K. (eds) Rapid Prototyping in Cardiac Disease. Springer, Cham. (2017) pp 3-7. https://doi.org/10.1007/978-3-319-53523-4_1

[1-14] P. Jiang, Z. Ji, X. Wang, and F. Zhou, Surface functionalization - a new functional dimension added to 3D printing. J. Mater. Chem. C8 (2020) 12380. https://doi.org/10.1039/D0TC02850A

[1-15] H.Y. Jeong, E. Lee, S.C. An, Y. Lim, Y.C. Jun, 3D and 4D printing for optics and metaphotonics. Nanophotonics 9 (2020) 1139. https://doi.org/10.1515/nanoph-2019-0483

[1-16] H. Park, Y.J. Lee, M. Kim, K.M. Kim, Safety of polyethylene terephthalate food containers evaluated by HPLC, migration test, and estimated daily intake. J. Food Sci. 73 (2008) T83–T89. https://doi.org/10.1111/j.1750-3841.2008.00840.x

[1-17] A.Y. Chen, Y. Bu, Y.T. Tang, Y. Wang, F. Liu, X.F. Xie, J.F. Gu. Deposition-rate dependence of orientation growth and crystallization of Ti thin films prepared by magnetron sputtering, Thin Solid Films 574 (2015) 71-77. https://doi.org/10.1016/j.tsf.2014.10.053

[1-18] E. Kondoh, K. Suzuki, L. Jin, S. Hamada, S. Shima, H. Hiyama. Density evaluation of sub-100 nm particles by using ellipsometry, ICPT 2017; Int. Conf. Planarization/CMP Technol. (2017) pp. 1–5.

[1-19] E. Kondoh, Y. Kawano, N. Takeyasu, T. Ohta. Interconnection formation by doping chemical-vapor-deposition aluminum with copper simultaneously: Al-Cu CVD, J. Electrochem. Soc. 141 (1994) 3494. https://doi.org/10.1149/1.2059359

[1-20] J.J. Watkins, J.M. Blackburn, T.J. McCarthy, Chemical fluid deposition: reactive deposition of platinum metal from carbon dioxide solution. Chem. Mater. 11 (1999) 213–215. https://doi.org/10.1021/cm981016f

[1-21] J.M. Blackburn, D.P. Long, A. Cabanas, J.J. Watkins, Deposition of conformal copper and nickel films from supercritical carbon dioxide. Science 294 (2001) 141–145. https://doi.org/10.1126/science.1064148

[1-22] V.N.V. Munagala, R. Chakrabarty, J. Song, R.R. Chromik, Effect of metal powder properties on the deposition characteristics of cold-sprayed Ti6Al4V-TiC coatings: an experimental and finite element study. Surf. Interfaces 25 (2021) 101208. https://doi.org/10.1016/j.surfin.2021.101208

[1-23] C.-Y. Chen, K.-Y. Lin, W.-T. Tsai, J.-K. Chang, C.-M. Tseng, Electroless deposition of Ni nanoparticles on carbon nanotubes with the aid of supercritical CO2 fluid and a synergistic hydrogen storage property of the composite. Int. J. Hydrogen Energy 35 (2010) 5490–5497. https://doi.org/10.1016/j.ijhydene.2010.03.035

[1-24] H. Bi, K.C. Kou, A.E. Rider, K. Ostrikov, H.W. Wu, Z.C. Wang, Low-phosporous nickel-coated carbon microcoils: Controlling microstructure through an electroless plating process. Appl. Surf. Sci. 255 (2009) 6888-6893. https://doi.org/10.1016/j.apsusc.2009.03.009

[1-25] H.-Y. Wang, S.-T. Chung, Y.-C. Chuang, W.-T. Tsai, Electroless Ni–B deposition from an emulsified supercritical carbon dioxide bath. Thin Solid Films 518 (2010) 7505–7508. https://doi.org/10.1016/j.tsf.2010.05.034

[1-26] W.-T. Chiu, C.-Y. Chen, T.-F.M. Chang, T. Hashimoto, H. Kurosu and M. Sone, Ni–P and $TiO_2$ codeposition on silk textile via supercritical $CO_2$

promoted electroless plating for flexible and wearable photocatalytic devices. Electrochim. Acta 294 (2019) 68. https://doi.org/10.1016/j.electacta.2018.10.076

[1-27] K. Tokuoka, C.-Y. Chen, T.-F.M. Chang, W.-T. Chiu, H. Kurosu, M. Sone, Metallization of PET textile utilizing supercritical $CO_2$ catalyzation. Microelectron Eng 223 (2020) 111233. https://doi.org/10.1016/j.mee.2020.111233

[1-28] M. Sano, Y. Tahara, C.-Y. Chen, T.-F. M. Chang, T. Hashimoto, H. Kurosu, T. Sato, M. Sone, Application of supercritical carbon dioxide in catalyzation and Ni-P electroless plating of nylon 6, 6 textile. Surf. Coat. Technol. 302 (2016) 336-343. https://doi.org/10.1016/j.surfcoat.2016.06.037

[1-29] P.-W. Cheng, T. Kurioka, C.-Y. Chen, T.-F. M. Chang, W.-T. Chiu, H. Hosoda, K. Takase, H. Ishihata, H. Kurosu, M. Sone, Platinum Metallization of Polyethylene Terephthalate by Supercritical Carbon Dioxide Catalyzation and the Tensile Fracture Strength. Materials 16 (2023) 2377. https://doi.org/10.3390/ma16062377

[1-30] C. Liao, M. Gu, Electroless deposition of polyaniline film via autocatalytic polymerization of aniline. Thin Solid Films 408 (2002) P37-42. https://doi.org/10.1016/S0040-6090(02)00066-4

[1-31] F. Muench, Electroless Plating of Metal Nanomaterials. ChemElectroChem 8 (2021) 2993–3012. https://doi.org/10.1002/celc.202100285

[1-32] D. Barker, Electroless Deposition of Metals. Trans. Inst. Met. 71:3 (2017) 121-124. https://doi.org/10.1080/00202967.1993.11871003

[1-33] D. Barker, Electroless deposition of metals. Surf. technol. 12 (1981) P77- 88. https://doi.org/10.1016/0376-4583(81)90138-2

[1-34] H. Chen, Q. Wu, Y. Wang, Q. Zhao, X. Ai, Y. Shen, X. Zou, d–sp orbital hybridization: a strategy for activity improvement of transition metal catalysts. Chem. Commun. 58 (2022) 7730-7740. https://doi.org/10.1039/D2CC02299K.

[1-35] H.H. Masallb, K.F. Al-Sultani, A. R.K.A. Ali, Improving Surface Properties of Inconel 600 Alloy by Electroless Ni-P Deposition. QJES. 13 (2019) 254-259. https://doi.org/10.30772/qjes.v12i4.642

[1-36] A. Małecki, A. Micek-Ilnicka, Effect of adding Lanthanum ($La3^{+}$) on surface performance of Ni-P electroless plating coatings on RB400 support anchor rod steel. Surf. Coat. Technol. 123 (2000) 72-77. https://doi.org/10.20964/110343

[1-37] J. Sudagar, J. Lian, W. Sha, Electroless nickel, alloy, composite and nano coatings – A critical review. J. Alloys Compd. 571 (2013) 183-204. https://doi.org/10.1016/j.jallcom.2013.03.107

[1-38] G. Cui, J. Zhao, S. Liu, G. Wu, Structural and Corrosion Properties of $NiP_x$ Metallic Glasses: Insights from EIS and DFT. J. Phys. Chem. C 115 (2011) 21169-21176.https://doi.org/10.1021/jp205751v

[1-39] H. Jia, X. Gao, Z. Chen, G. Liu, X. Zhang, H. Yan, H. Zhou, L. Zheng, The high yield synthesis and characterization of gold nanoparticles with superior stability and their catalytic activity. CrystEngComm 14 (2012) 7600-7606. https://doi.org/10.1039/c2ce25840d

[1-40] O.N. Vrublevskaya, T.N. Vorobyova, H.-K. Lee, S.-B. Koo, Electroless gold plating from tetrachloroaurate solutions containing hexacyanoferrate(II) ions. Trans. Inst. Met. 85:5 (2007) 254-259. https://doi.org/10.1179/174591907X229662

[1-41] B. Wu, B. Tan, G. Tan, M. Zeng, J. Luo, G. Hu, J. Luo, Z. Hao, S. Lai, B. Liu, Electroless deposition of Ni–P/Au coating on Cu substrate with improved corrosion resistance from Au(III)–DMH based cyanide-free plating bath using hypophosphite as a reducing agent. RSC Adv. 11 (2021) 39153-39168. https://doi.org/10.1039/d1ra07952b

[1-42] T. Yu, D.Y. Kim, H. Zhang, Y. Xia, Platinum concave nanocubes with high-index facets and their enhanced activity for oxygen reduction reaction. Angew. Chem. Int. Ed. 50 (2011) 2773–2777. https://doi.org/10.1002/anie.201007859

[1-43] J. Weissmuller, R.N. Viswanath, D. Kramer, P. Zimmer, R. Wurschum, H. Gleiter, Charge-induced reversible strain in a metal. Science 300 (2003) 312–315. https://doi.org/10.1126/science.1081024

[1-44] J. J. Yang, J. Borghetti, D. Murphy, D.R. Stewart, R.S. Williams, A family of electronically reconfigurable nanodevices. Adv. Mater. 21 (2009) 3754–3758. https://doi.org/10.1002/adma.200900822

[1-45] M. Michel, A. Taylor, R. Sekol, P. Podsiadlo, P. Ho, N. Kotov, L. Thompson, High-performance nanostructured membrane electrode assemblies for fuel cells made by layer-by-layer assembly of carbon nanocolloids. Adv. Mater. 19 (2007) 3859–3864. https://doi.org/10.1002/adma.200701219

[1-46] C. Pang, G.Y. Lee, T.I. Kim, S.M. Kim, H. N. Kim, S.H. Ahn, K.Y. Suh, A flexible and highly sensitive strain-gauge sensor. Nature Materials 11 (2012) 795–801. https://doi.org/10.1038/nmat3380

[1-47] J.A. Hyatt, Liquid and Supercritical Carbon Dioxide as Organic Solvents, J. Org. Chem. 49 (1984) 5097-5101. https://doi.org/10.1021/jo00200a016

[1-48] M. McHugh, V. Krukonis, Supercritical fluid extraction: principles and practice. Elsevier (2013).

[1-49] X. Lou, H.-G. Janssen, C.A. Cramers, Temperature and pressure effects on solubility in supercritical carbon dioxide and retention in supercritical fluid chromatography. J. Chromatogr. A 785 (1997) 57-64. https://doi.org/10.1016/S0021-9673(97)00693-6

[1-50] R. B. Richards, Polyethylene-structure, crystallinity and properties. J. Chem. 1 (1951) 370-376. https://doi.org/10.1002/jctb.5010010812

[1-51] D. Mileva, D. Tranchida, M. Gahleitner, Designing polymer crystallinity: An industrial perspective. Polym. Crystallization 1 (2018) e10009. https://doi.org/10.1002/pcr2.10009

[1-52] T. J. Bessell, D. Hull, J. B. Shortall, The effect of polymerization conditions and crystallinity on the mechanical properties and fracture of spherulitic nylon 6. J Mater Sci 10 (1975) 1127-1136. https://doi.org/10.1007/BF00541393

[1-53] M. A. Kennedy, A. J. Peacock, L. Mandelkern, Tensile Properties of Crystalline Polymers: Linear Polyethylene. Macromolecules 27 (1994) 5297-5310. https://doi.org/10.1021/ma00097a009

[1-54] M. Takayanagi, S. Uemura, S. Minami, Application of equivalent model method to dynamic rheo-optical properties of crystalline polymer. J. Polym. Sci., Part C: Polym. Symp. 5 (1964) 113-122. https://doi.org/10.1002/polc.5070050111

[1-55] J. Xiao, D. Zhang, M, Zheng, Y. Bai, Y. Sun. L. Zhang, Q. Guo, J. Yang, 3D printing of metallic structures using dopamine-integrated photopolymer. J. Mater. Res. Technol. 19 (2022) 1355-1366. https://doi.org/10.1016/j.jmrt.2022.05.009

[1-56] J. Huang, C. Gui. H. Ma, P. Li, W. Wu. Z. Chen, Surface metallization of PET sheet: Fabrication of Pd nanoparticle/polymer brush to catalyze electroless nickel plating. Compos. Sci. Technol. 202 (2021) 108547. https://doi.org/10.1016/j.compscitech.2020.108547

[1-57] R. Zhang, C. Gui, J. Huang, G. Yang, Rational design of Ag nanoparticle/polymer brush and its application in electroless deposition to fabricate adhesion-enhanced copper pattern for functional flexible electronics. J Taiwan Inst. Chem. Eng. 125 (2021) 424-433. https://doi.org/10.1016/j.jtice.2021.06.034

[1-58] L. Li, D. Chen, Y. Long, F. Wang, Z. Kang, Silane modification of semi-curing epoxy surface: High interfacial adhesion for conductive coatings. Prog. Org. 174 (2023) 107228. https://doi.org/10.1016/j.porgcoat.2022.107228

CHAPTER 2

# *Sc-$CO_2$ assisted functionalization of Polyethylene Terephthalate (PET) toward flexible catalytic electrodes*

## 2.1 Introduction

The flexible catalytic electrode was a composite of Au/Ni-P/ PET. Sc-$CO_2$ was used as the solvent in the catalyzation step of an electroless plating process. $Pd(hfa)_2$ was used as the source of the palladium catalyst for the high solubility in sc-$CO_2$. After the catalyzation step, Ni-P was firstly deposited on the catalyzed PET as the sacrificial layer for later gold deposition. A tape adhesion test, which could reveal the positive contribution of the sc-$CO_2$ catalyzation on reliability of the metallized PET. After deposition of the gold layer, the flexible Au/Ni-P/PET composite was evaluated as the catalytic electrode in oxidation of urea, ascorbic acid and glucose to demonstrate the applicability in flexible biosensors.

## 2.2 Experimental

### *2.2.1 Material*

PET films provided by Toray Industries, Inc. were cut into small pieces having dimensions of 2.0 cm x 2.0 cm to be used as the substrate. A conventional catalyzation step was conducted as comparisons with the sc-$CO_2$ catalyzation step. For the conventional catalyzation step, a commercially available catalyzation solution (ICP Accera KCR, Okuno Chemical Industries Co., Ltd.) was used. $CO_2$ used in the sc-$CO_2$ catalyzation step was provided by Nippon Tansan Gas Co., Ltd. and had a purity of 99.99%. $Pd(hfa)_2$ (<=100%), $KAuCl_4$ (99.995%), urea (99.0-100.5%), L-Ascorbic acid (99%), D-(+)-Glucose (≥99.5%) and phosphate buffered saline (PBS, P5493) were purchased from Sigma-Aldrich. The Ni-P electroless plating solution was a commercially available solution (Top Nicoron VS-LF, Okuno Chemical Industries Co., Ltd) having a composition of nickel chloride (9 wt%), sodium hypophosphite (12 wt%), complexing agent (12 wt%), and ion-exchanged water (67 wt%). The gold electroless plating solution was also a commercially available solution (Non Cyanide Electroless Gold Solution, MATEX Japan Co., Ltd.), and the solution contained 2 g/L of gold and pH at 7. For the tape adhesion test, tapes with a model number of 810-1-18D Scotch Magic Tape by 3M were used.

### *2.2.2 Conventional and sc-$CO_2$ Catalyzation*

In the conventional catalyzation step, the PET film was immersed in the ICP Accera KCR solution for 30 min at 30°C. For the sc-$CO_2$ catalyzation step, a high pressure apparatus (Japan Spectra Company, Japan) was utilized. The reaction cell was made of stainless steel 316 with polyether ether ketone coating on the inner wall, and the inner volume was 50.0 ml. A piece of the PET film and 50.0 mg of $Pd(hfa)_2$ were placed in the

reaction cell before pressurizing $CO_2$ into the reaction cell. The catalyzation was conducted at 15.0 MPa and 80.0 °C for 2.0 hr. Density of $CO_2$ is 0.428 g/ml at 80.0 °C and 15.0 MPa [2-1]. 50.0 mg of $Pd(hfa)_2$ in the reaction cell implied the concentration in sc-$CO_2$ was 0.4 wt%.

*2.2.3* Metal deposition

No post-treatment was conducted after the catalyzation step. The catalyzed PET films were immersed into the Ni-P electroless plating solution at 70.0 °C for 3.0, 6.0, 9.0 and 12.0 min. For the gold deposition, Ni-P/PET composites with 3 min of the Ni-P deposition time were used. Before deposition of the gold layer, a sensitization step is needed. The sensitization was conducted by immersing the Ni-P/PET composite into a 0.1 mM $KAuCl_4$ solution at 30.0 °C for 2.0 hr to form gold particles on the surface. Then the sensitized Ni-P/PET composite was immersed in the gold electroless plating solution at 65°C for 60.0, 90.0 and 120.0 min to cover the Ni-P surface with gold.

*2.2.4* Characterization

Surfaces of the Ni-P/PET and the Au/Ni-P/PET composites were observed by a scanning electron microscope (SEM, S-4300SE, HITACHI). Crystal structures of the Ni-P/PET and the Au/Ni-P/PET composites were identified by X-ray diffraction (XRD, Ultima IV, Rigaku). Thickness of the Ni-P and gold layers were estimated by observing cross-section of the Ni-P/PET and the Au/Ni-P/PET composites, respectively, by the SEM. The electrical resistance was evaluated by a four-point probe (MCP-T37, Mitsubishi Chemical Analytech Co., Ltd.). For the tape adhesion test of the Ni-P/PET

composite, a piece of the 3M tape was firmly stuck to the sample surface while applying a 1 kg load. After removing the load, the 3M tape was peeled off to complete the tape adhesion test. The tape adhesion test was conducted for five samples prepared under the same conditions to ensure reliability of the result.

Amperometric curves generated from oxidation of urea, ascorbic acid and glucose were prepared to demonstrate the catalytic activity of the flexible Au/Ni-P/PET composites toward catalytic electrodes in biosensors. The amperometric measurement was performed with a three-electrode system and a potentiostat (1287A, Solartron Analytical). The counter electrode was a platinum plate having a surface area of 4.0 $cm^2$, and the reference electrode was a Ag/AgCl reference electrode. The applied potential was at +0.3, +0.35 V and +0.25 vs Ag/AgCl for oxidation of urea [2-2], ascorbic acid [2-3] and glucose [2-4], respectively. The supporting solution was 40 ml of the PBS. At the beginning of the amperometric measurement, the concentration of the biomolecules to be detected was at zero. The concentration step-wisely increased to were 25, 50 and 75 μM at a roughly 30 s interval for urea. The concentrations for ascorbic acid and glucose ascorbic acid were 2.5, 5.0 and 7.5 mM at the same 30 s interval. The tape adhesion test was also conducted for one of the Au/Ni-P/PET composite electrodes, and the electrode was used in the amperometric measurement of glucose to demonstrate the high reliability as flexible catalytic electrode.

## 2.3 Results and discussion

### *2.3.1 Metallization of PET*

A piece of the PET film is shown in Fig. 2-1(a). The PET film was transparent and smooth. After the conventional catalyzation step, the PET film was still transparent.

Metallization of the conventionally catalyzed PET was not successful. The PET film remained clear and transparent without any signs of metal-like features on the surface after the immersion in the Ni-P solution electroless plating solution for 12.0 min, and the gold deposition was also not possible since there was no Ni-P on the surface. For the sc-$CO_2$ catalyzed PET, the appearance did not change much as shown in Fig. 2-1(b). The sc-$CO_2$ catalyzed PET was transparent and showed a faint yellow color. The yellow color was suggested to be originated from the color of $Pd(hfa)_2$, which is yellow. Surface of the sc-$CO_2$ catalyzed PET film was covered with grey metal-like coatings after the Ni-P deposition step as shown in Fig. 2-1(c), and the color changed to golden color after the gold deposition step as shown in Fig. 2-1 (d).

Effects of the Ni-P deposition time on the surface morphology of the Ni-P/PET composite could be observed from the SEM images shown in Fig. 2-2. Cauliflower-like nodules were observed on the surfaces. This is a typical morphology of amorphous Ni-P prepared by electroless plating [2-5, 2-6]. In electroless plating, reduction of metal ions in the solution is driven by the reducing agents, and this reducing power is not high hence the particles tend to have anisotropic growth leading to the cauliflower-like morphology. The amount and average size of the cauliflower-like nodules increased as the Ni-P deposition time increased. The result indicated heterogenous nucleation was favored over homogeneous nucleation leading to formation of larger particles as the Ni-P deposition time prolonged.

The thickness of the Ni-P layer reached 0.51 μm after 3.0 min of the Ni-P deposition, and the thickness increased to 0.74, 1.04 and 1.37 μm when the Ni-P deposition time extended to 6.0, 9.0 and 12.0 min, respectively, as shown in Fig. 2-3. The Ni-P thickness was determined from the cross-sectional observations illustrated in Fig. 2-

3(b) to (e). The Ni-P thickness increased almost linearly as the Ni-P deposition time increased. When considering the Ni-P overall growth rate, the overall growth rate gradually decreased as the Ni-P deposition time increased. In electroless plating, an incubation time is required before reduction of the metal ions starts, and the reduction reaction rate slows down as the reaction proceeds because of consumption of the metal ions and the reducing agents in the solution [2-7].

XRD patterns of the Ni-P/PET composites obtained in this study are shown in Fig. 2-4. As mentioned before, Ni-P obtained by electroless plating is usually amorphous [2-6]. All XRD patterns had a broadened peak at $2\theta = 45°$, which were suggested to be contributed by the amorphous Ni-P. Signals at around $2\theta = 25°$ were caused by the PET. When compared with the PET XRD peak, intensity of the Ni-P broad peak gradually increased as the Ni-P deposition time increased, which indicated an increase in the Ni-P amount on the PET with the Ni-P deposition time. This increase corresponded well with the relationship between the Ni-P thickness and the Ni-P deposition time shown in Fig. 2-3(a).

Contribution of the sc-$CO_2$ catalyzation on the metallization of PET was quantified from electrical resistance of the Ni-P/PET composites as shown in Fig. 2-5. The electrical resistance reached 0.70 Ω when 3.0 min of the Ni-P deposition time was used, which suggested fully coverage of the Ni-P on the PET film. As the Ni-P deposition time prolonged to 6.0, 9.0 and 12.0 min, the electrical resistance decreased to 0.55, 0.27, and 0.23 Ω, respectively. The decrease in the electrical resistance was a result of the increased amount of Ni-P on the PET film. After the tape adhesion test, the electrical resistance slightly increased to 0.79, 0.76, 0.30 and 0.73 Ω for the samples with 3.0, 6.0, 9.0 and 12.0 min of the Ni-P deposition time, respectively. The increasing level of the electrical

resistance was the largest for the 12.0 min sample. The surface condition of the Ni-P layer with 12.0 min of the deposition time is suggested to be the main cause. As shown in Fig. 2-2, the average size of the particles on the surface and the surface roughness were the largest for the 12.0 min sample. The large particle size and rough surface both led to a higher chance of the metal coating to be damaged and ripped off from the Ni-P/PET composite during the tape adhesion test and eventually resulted the increased electrical resistance. However, the electrical resistances were still low suggesting that the Ni-P/PET composite retained a decent electrical conductivity after the tape adhesion test, which revealed the positive effect of the sc-$CO_2$ catalyzation on the metallization of PET.

*2.3.2 Characterization of Au/Ni-P/PET composite*

After the sensitization in 0.1 mM $KAuCl_4$ solution, gold was deposited on the Ni-P/PET composites. For the sc-$CO_2$ catalyzed and then Ni-P deposited Ni-P/PET composites, the entire surface changed to a golden color after 60.0 min of the gold deposition time. Surfaces of the Au/Ni-P/PET composites were covered with tiny particles as shown in Fig. 2-6. Rugged surfaces were observed when the gold deposition time was longer than 60.0 min.

The gold thickness was 1.02 μm after 60 min of the gold deposition, and the thickness slowly increased to 1.32 and 1.65 μm after 90 and 120 min, respectively, of the gold deposition as summarized in Fig. 2-7. Again, an incubation time was needed for formation of gold on the surface, and the gold growth rate was much smaller than the Ni-P growth rate. Gold ions are very active in solutions, and complexing agents are needed to stabilize the gold ions to allow it to be stored before usage. Consequently, reduction of gold ions would be limited by the complexing agents and resulted a slow growth rate. In

fact, the gold growth rate obtained in this study corresponded well with the information provided by the gold electroless plating solution supplier.

XRD patterns of the Au/Ni-P/PET composites are shown in Fig. 2-8. Signals at around 2θ = 40°, 45°, 65°, 78° and 83° were evidences of face-centered cubic (FCC) crystal structure of gold (JCPDS card No 46-1043). The peak at 2θ = 25° was contributed by the PET, and signals from the Ni-P were not identified. With 3.0 min of the Ni-P deposition time, the Ni-P thickness was expected to be at 0.51 μm. The gold thickness reached 1.02 after 60 min of the gold deposition time, hence, the amount of Ni-P left on the PET should be very low. The poor crystallinity of Ni-P would be another reason. On the other hand, relative intensity of the gold peaks increased as the gold deposition time increased. This also suggested an increase in the amount of gold on the surface.

Gold is one of the most electrically conductive materials. The electrical resistances of the Au/Ni-P/PET composites were all much lower than those of the Ni-P/PET composites, which the electrical resistance decreased by about 10 times after the gold deposition. The electrical resistances of the Au/Ni-P/PET composites are summarized in Fig. 2-9. The electrical resistance was 0.015 Ω for the composite with 60 min of the gold deposition, and the value further reduced to 0.012 and 0.010 Ω after 90 and 120 min of the gold deposition, respectively.

*2.3.3 Catalytic activity of Au/Ni-P/PET composite*

The catalytic activity of the Au/Ni-P/PET composite in oxidation of three common sensing-targets (urea, ascorbic acid and glucose) in biosensors were evaluated. After introducing the biomolecule into the PBS solution (25 μM for urea and 2.5 mM for ascorbic acid and glucose), a sudden increase in the current density was observed as

shown in Fig. 2-10 and Fig. 2-11(a) The increase of the current response represented the current generated from the oxidation reaction of the biomolecules. The current density increased again after adjustment of the concentration to a higher value (50 and 75 μM for urea and 5.0 and 7.5 mM for ascorbic acid and glucose). In oxidation of these three biomolecules, the current density increased immediately after introducing the biomolecules into the PBS solution, and then the current density gradually reduced to a steady-state level. The steady-state level was higher than the steady-state level at a lower concentration of the biomolecules. The gradual decrease in the current density is suggested to be caused by products produced from the oxidation reaction that adsorb on surface of the electrode and interfere with the main reaction [8]. Nevertheless, the overall current density was higher when a higher concentration of the specific biomolecule was introduced into the PBS solution, which revealed the catalytic activity of the flexible Au/Ni-P/PET composite electrode in the oxidation reaction. Regarding reliability of the Au/Ni-P/PET composite, after the tape adhesion test, the composite electrode still showed an obvious increase in the current density along an increase in the glucose concentration. The result confirmed the intactness of the Au/Ni-P/PET composite.

## 2.4 Chapter summary

Functionalization of PET films were achieved by an electroless plating process involving a sc-$CO_2$ catalyzation step to demonstrate the potential in preparation of flexible catalytic electrodes. Metallization of the PET catalyzed by conventional method was not successful. The sc-$CO_2$ catalyzation step was conducted in sc-$CO_2$ containing $Pd(hfa)_2$ as the source of the palladium catalyst for the later Ni-P deposition. The Ni-P layer was used as the sacrificial layer in deposition of the gold layer. By the sc-$CO_2$

catalyzation, the electrical resistance of the Ni-P/PET reached 0.27 Ω after 9.0 min of the Ni-P deposition time. The electrical resistance merely changed to 0.30 Ω after the tape adhesion test, which confirmed contributions of the sc-$CO_2$ catalyzation on the reliability of the Ni-P/PET composite. Gold was deposited on the Ni-P/PET composite also by an electroless plating process, and the electrical resistance was lowered to 0.015 Ω after 60.0 min of the gold deposition. The catalytic activity of the Au/Ni-P/PET composites in oxidation of urea, ascorbic acid and glucose were confirmed, which demonstrate the potential as flexible catalytic electrodes in biosensors.

## 2.5 References


[2-1] E.W. Lemmon, Thermophysical properties of fluid systems. NIST Chem. Webb (1998).

[2-2] S. Srivastava, P.R. Solanki, A. Kaushik, M.A. Ali, A. Srivastava, B.D. Malhotra, A self assembled monolayer based microfluidic sensor for urea detection. Nanoscale 3 (2011) 2971–2977. https://doi.org/10.1039/C1NR10240K

[2-3] M. Osial, M. Warczak, P.J. Kulesza, P. Krysiński, M. Gniadek, Hybrid polyindole gold nanobrush for electrochemical oxidation of ascorbic acid. J. Electroanal. Chem. 877 (2020) 114664. https://doi.org/10.1016/j.jelechem.2020.114664

[2-4] L.Y. Chen, X.Y. Lang, T. Fujita, M.W. Chen, Nanoporous gold for enzyme-free electrochemical glucose sensors. Scr. Mater. 65 (2011) 17–20. https://doi.org/10.1016/j.scriptamat.2011.03.025

[2-5] P.-W. Cheng, C.-Y. Chen, T. Ichibayashi, T.-F.M. Chang, M. Sone, S.Nishimura, Metallization of 3D-printed polymer structures via supercritical carbon dioxide-assisted electroless plating. MRS Commun. (2021) 1–5. https://doi.org/10.1557/s43579-021-00022-2

[2-6] K.-Y. Lin, T.-J. Yang, W.-T. Tsai, Synthesis of invar alloy powders by electroless plating. Mater. Sci. Eng. A 416 (2006) 226–231. https://doi.org/10.1016/j.msea.2005.10.028

[2-7] H. Ashassi-Sorkhabi, A. Mirmohseni, H. Harrafia, Evaluation of initial deposition rate of electroless Ni–P layers by QCM method. Electrochim. Acta 50 (2005) 5526–5532. https://doi.org/10.1016/j.electacta.2005.03.056

[2-8] Y. Ito, T.-F.M. Chang, Y.-A. Chien, C.-Y. Chen, P. Chakraborty, T. Nakamoto, M. Sone, Catalytic activity of atomic gold-decorated polyaniline support in glucose

oxidation. Electrochem 1 (2020) 394–399.

https://doi.org/10.3390/electrochem1040026

## 2.6 Figures

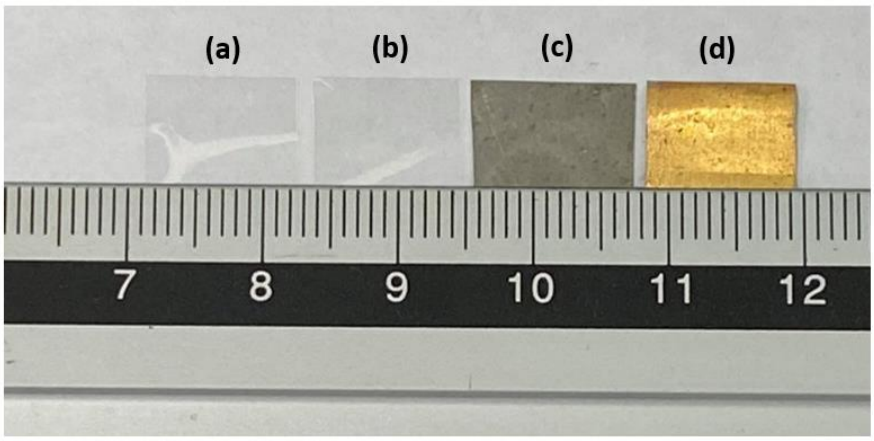


**Figure 2-1**. Image of the (a) PET film , (b) sc-$CO_2$ catalyzed PET films, (c) Ni-P/PET composite and (d) Au/Ni-P/PET composite. Unit of the major scale of the ruler shown in the figure is cm.

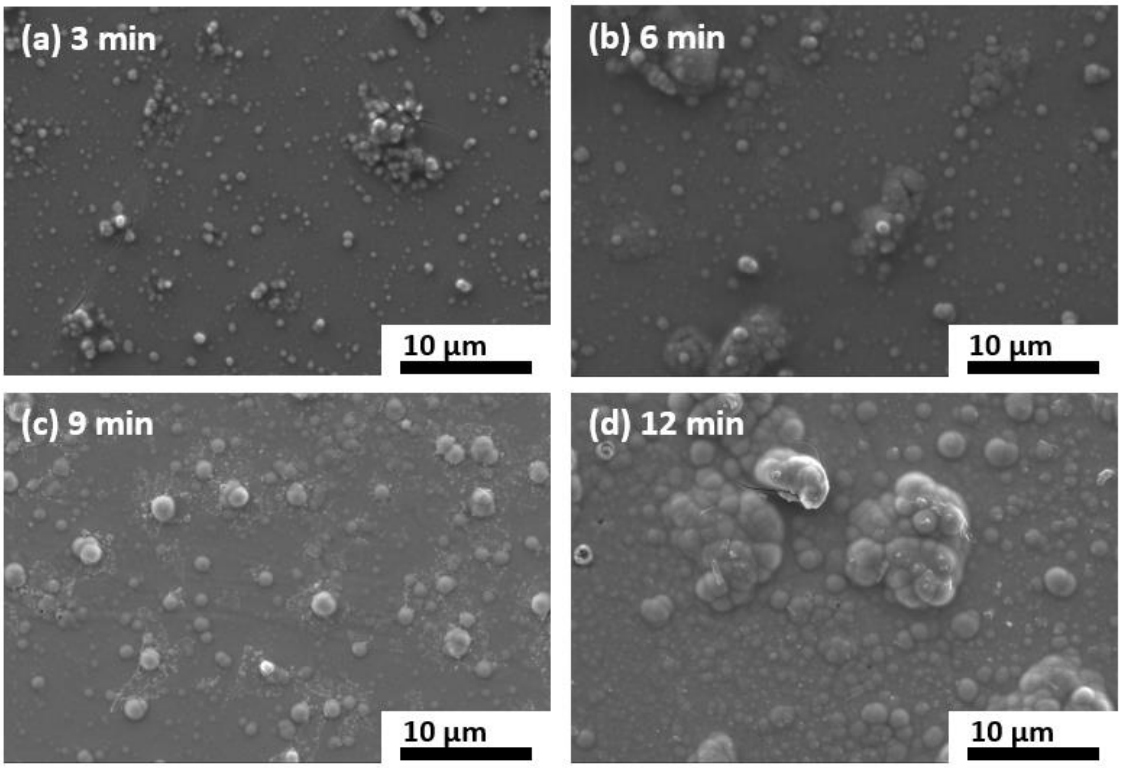


**Figure 2-2**. SEM observations of top views of the Ni-P/PET composites prepared with (a) 3.0, (b) 6.0, (c) 9.0 and (d) 12.0 min of the Ni-P deposition time.

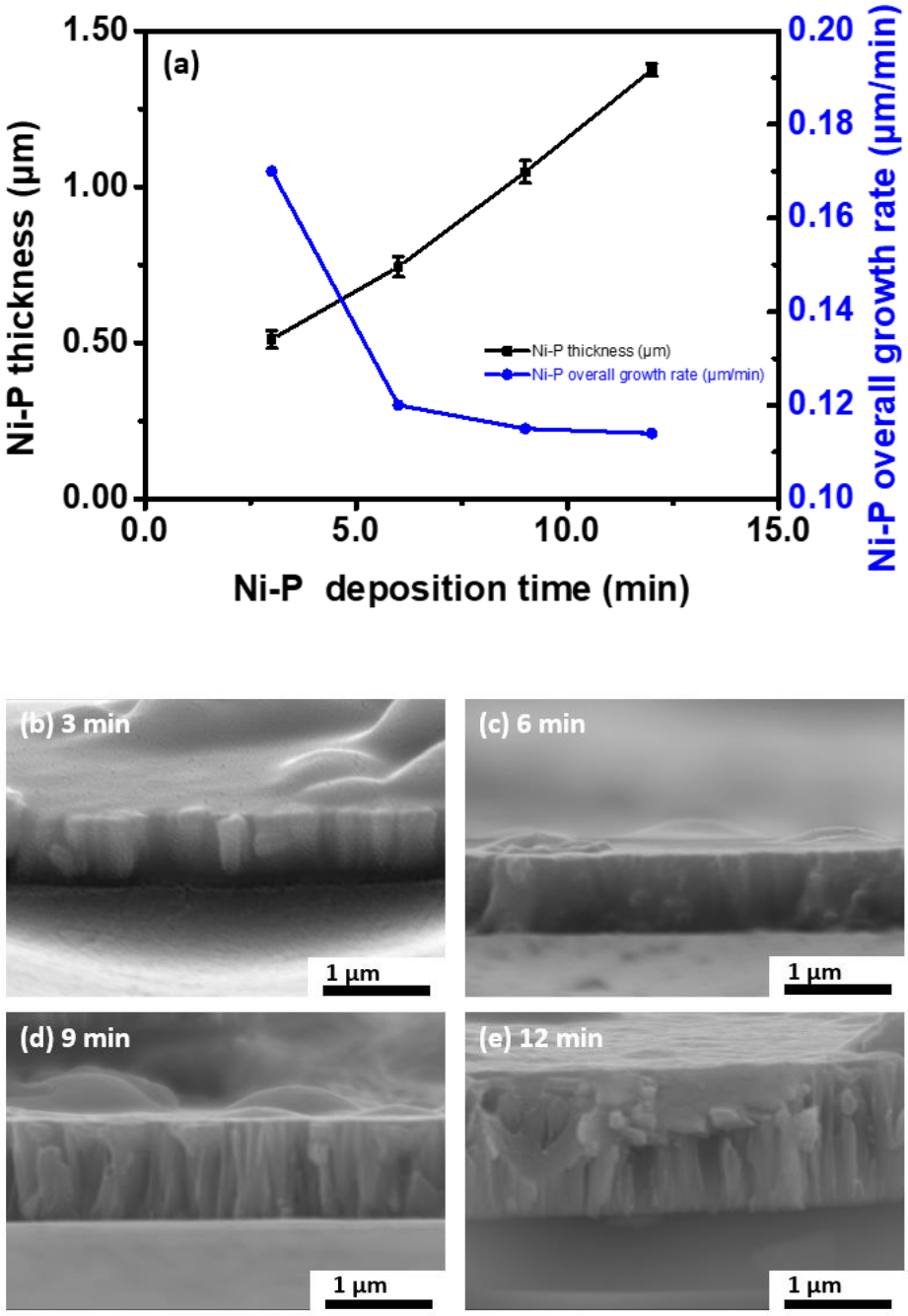


**Figure 2-3**. (a) a plot of the Ni-P deposition time versus the Ni-P layer thickness and the overall growth rate, and SEM observations of cross-sectional views of the Ni-P/PET composites prepared with (b) 3.0, (c) 6.0, (d) 9.0 and (e) 12.0 min of the Ni-P deposition time.

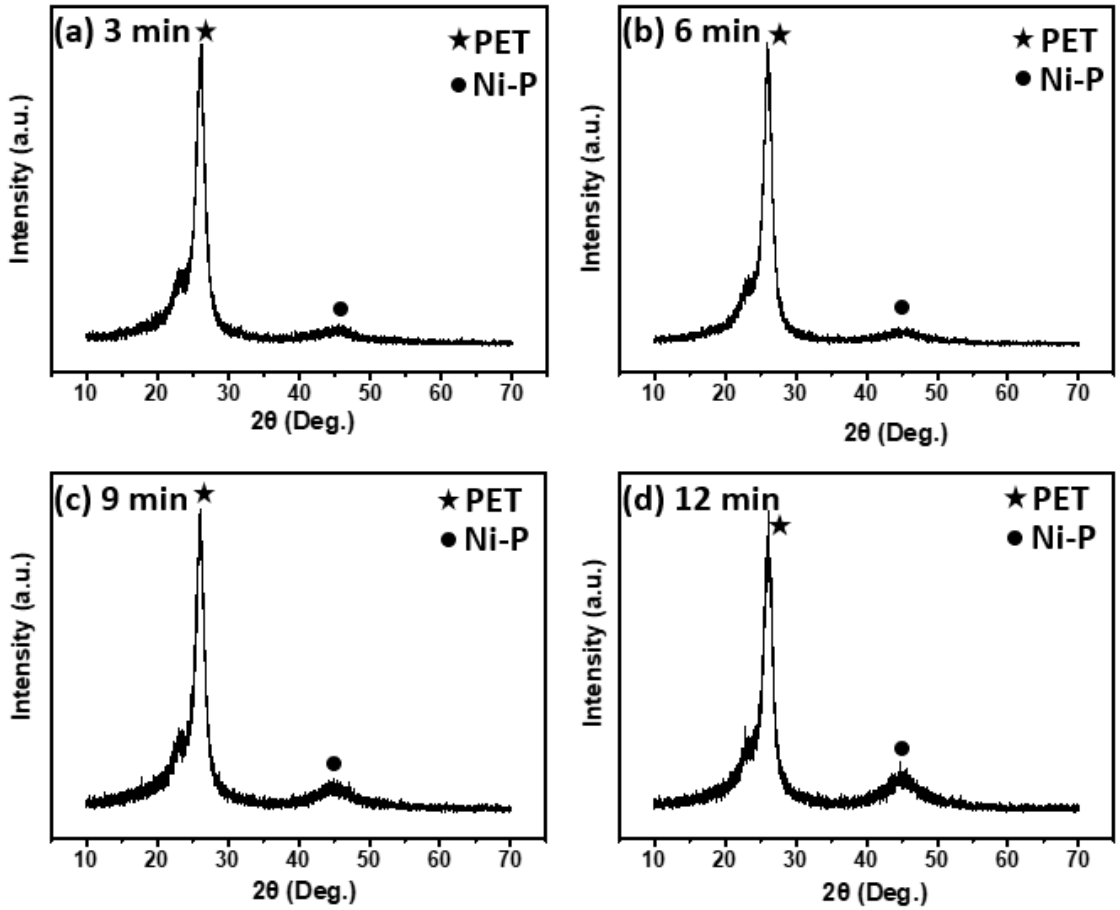


**Figure 2-4**. XRD of the Ni-P/PET composites prepared with (a) 3.0, (b) 6.0, (c) 9.0 and (d) 12.0 min of the Ni-P deposition time.

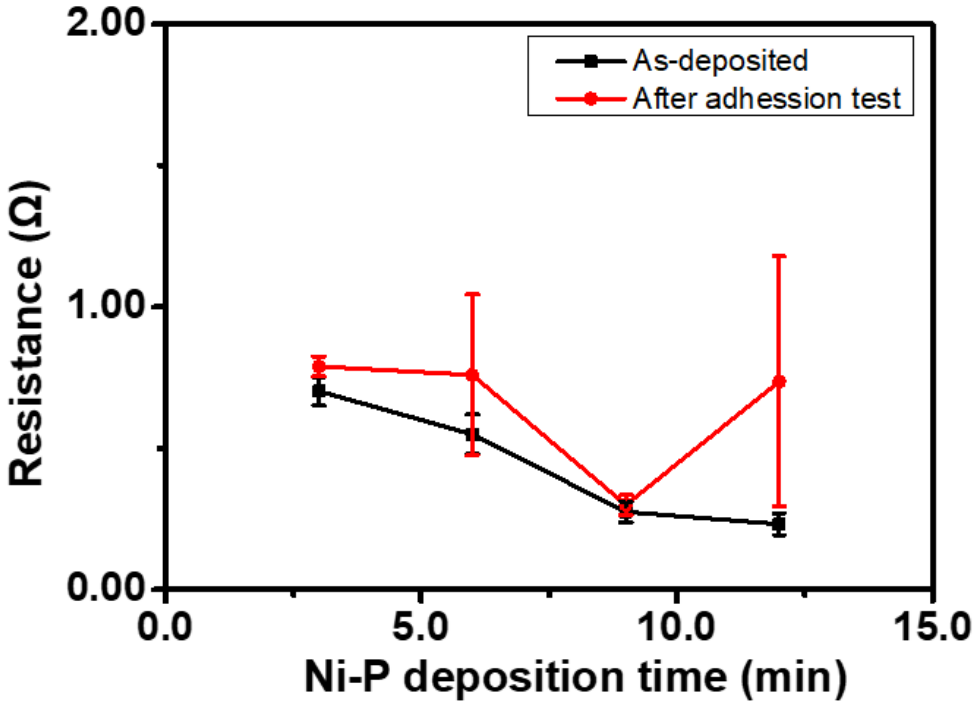


**Figure 2-5**. Plots of the Ni-P deposition time versus the electrical resistance.

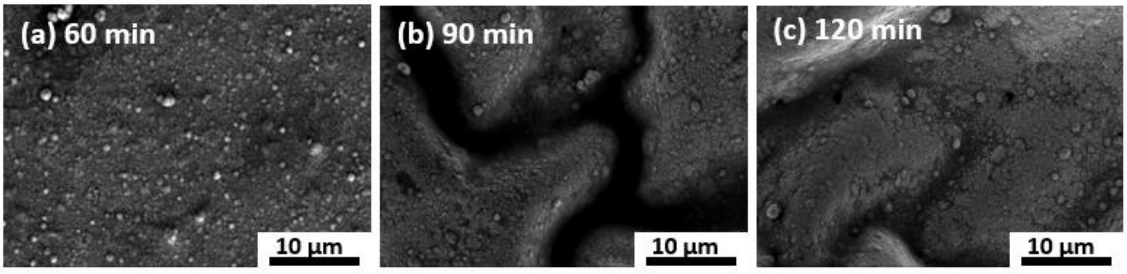


**Figure 2-6**. Surface morphology of the Au/Ni-P/PET composites prepared with (a) 60.0, (b) 90.0 and (c) 120.0 min of the gold deposition time.

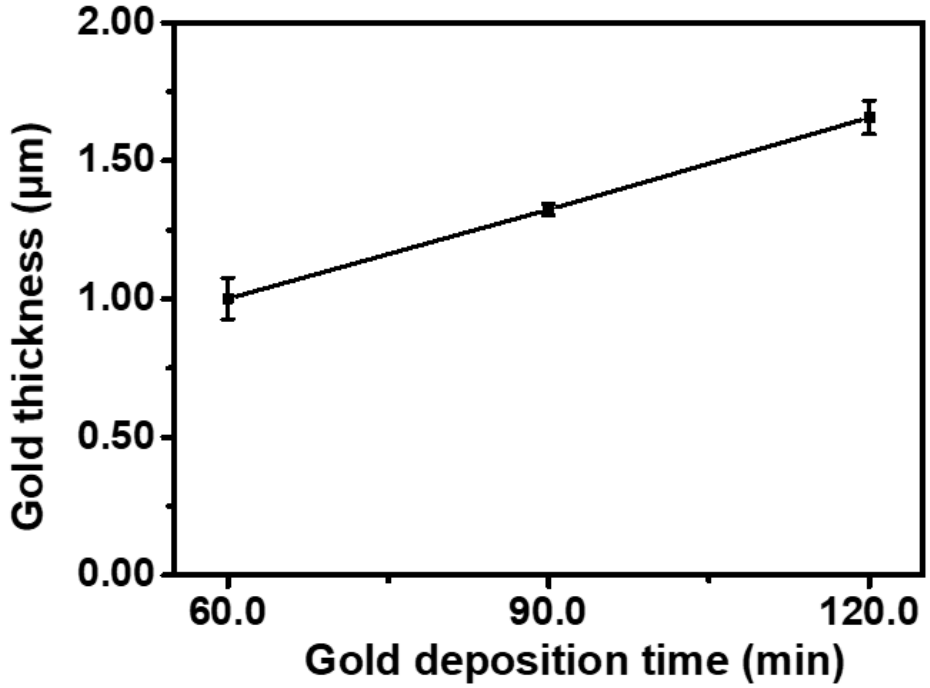


**Figure 2-7**. A plot of the gold deposition time versus the gold layer thickness.

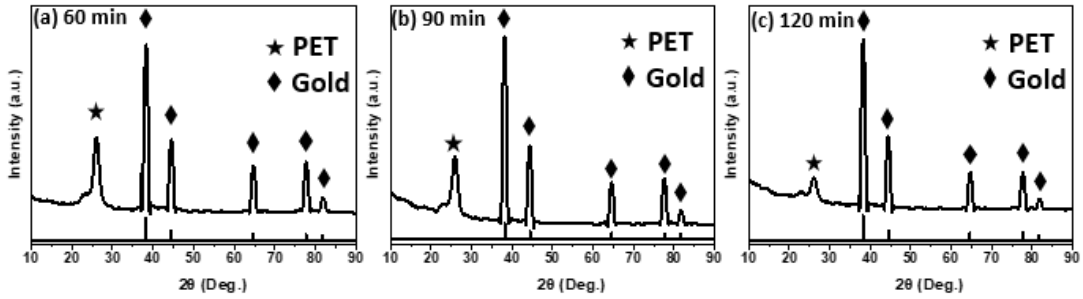


**Figure 2-8**. XRD of Au/Ni-P/PET composites with (a) 60.0, (b) 90.0 and (c) 120.0 min of the gold deposition time. (FCC Au: JCPDS no. 04-0784)

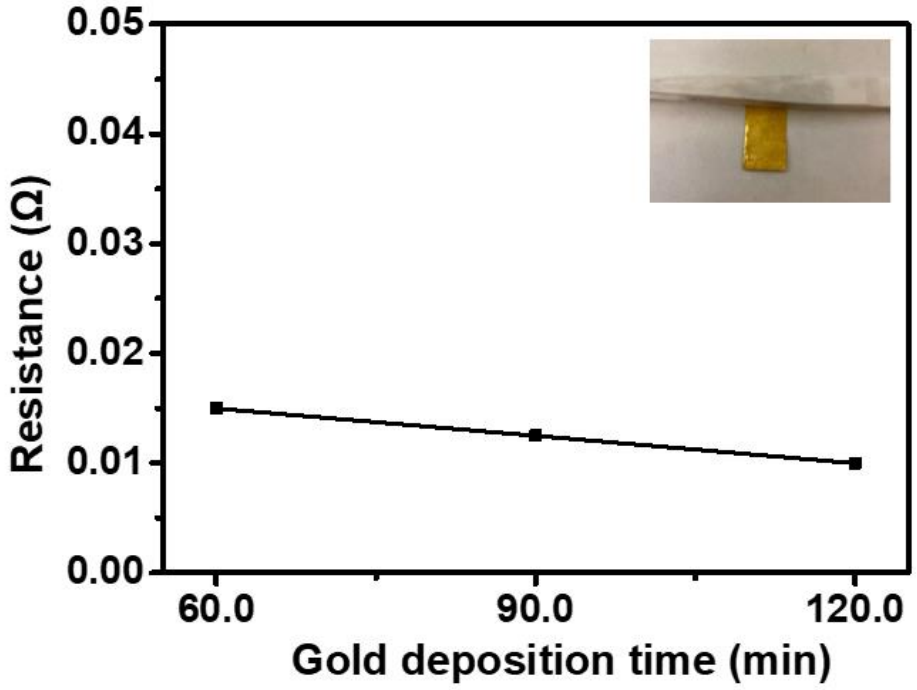


**Figure 2-9**. A plot of the gold deposition time versus the electrical resistance. The insert image shows appearance of the Au/Ni-P/PET composite.

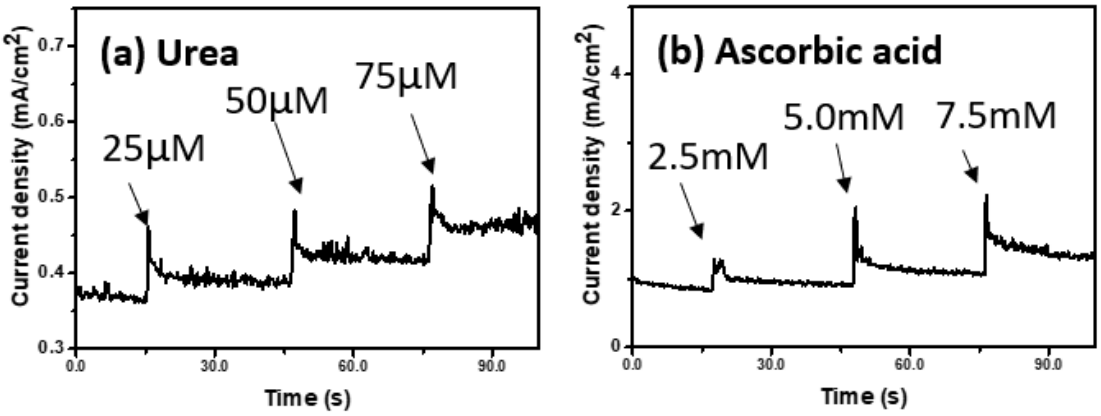


**Figure 2-10**. Amperometric curves generated from oxidation of (a) urea and (b) ascorbic acid in PBS using the Au/Ni-P/PET composite as the catalytic electrode.

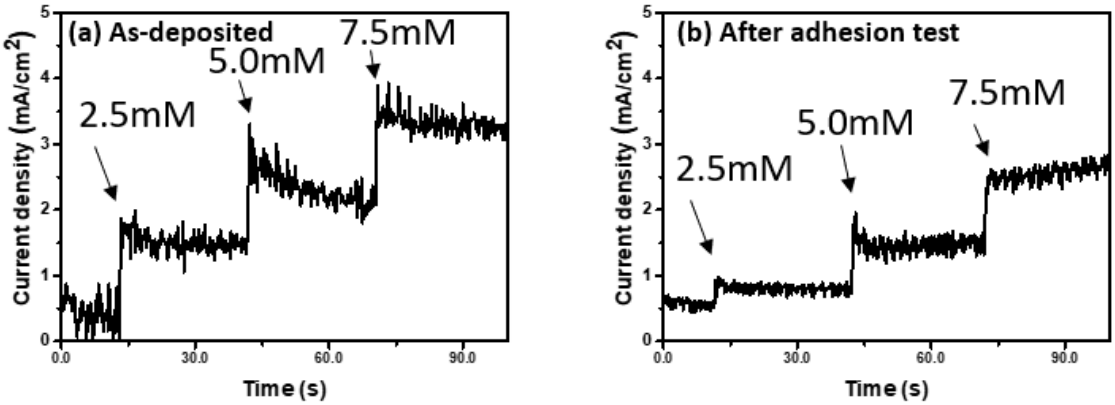


**Figure 2-11**. Amperometric curves generated from oxidation of glucose in PBS using the (a) as-fabricated and the (b) tape adhesion tested Au/Ni-P/PET composite as the catalytic electrode.

CHAPTER 3

# *Platinum metallization of Polyethylene Terephthalate (PET) by sc-$CO_2$ catalyzation and the tensile fracture strength*

## 3.1 Introduction

In the chapter 2, a flexible catalytic electrode composite of Au/Ni-P/PET was successfully fabricated. While gold is commonly used in bioelectronic components, platinum (Pt) is often preferred for its high biocompatibility and ability to avoid allergic reactions in individuals [3-1]. However, Pt electroless plating is rarely reported in metallization of the PET. To expand the range of metalized flexible electronic components for various applications. In this chapter, metallization of biocompatible Pt metal is realized by supercritical $CO_2$ (sc-$CO_2$) assisted electroless plating. The catalyst precursor used in the sc-$CO_2$ catalyzation step is an organometallic compound, palladium (II) acetylacetonate ($Pd(acac)_2$). The electrical resistance is evaluated, and a tape adhesion test is utilized to demonstrate intactness of the Pt layer on the PET film. A tensile test is conducted to evaluate the mechanical strength of the Pt/PET. In-situ electrical resistances of the specimen are monitored during the tensile test. The fracture strength is determined

from the stress value when the short circuit occurred. The promoted fracture strength and the decent electrical conductivity demonstrate the advantages toward biomedical devices.

## 3.2 Experimental

### *3.2.1 Materials*

PET films (Toray Industries, Inc.) were cut into dog-bone shaped specimen as illustrated in Fig. 3-1. In the narrow section, the length was 18 mm, the width was 3 mm, and the thickness was 0.1 mm. The metallization of the PET by a conventional catalyzation step was conducted to be used as comparisons with the sc-$CO_2$ catalyzation step. A commercial catalyzation solution (Okuno Chemical Industries Co., Ltd.: ICP Accera KCR) was used for the conventional catalyzation step. For the sc-$CO_2$ catalyzation, $CO_2$ with a purity of 99.99% was purchased from Nippon Tansan Gas Co., Ltd. Palladium(II) acetylacetonate ($Pd(acac)_2$) and ε-caprolactam (99%) were purchased from Sigma-Aldrich. The Pt electroless plating solution was also a commercial solution (MATEX Japan Co., Ltd.: Non-Cyanide Electroless Platinum Solution.), and the solution contained potassium tetranitroplatinate (0.1% ~ 0.3%), sodium borohydride (0.05% ~ 0.3%), others (0.5% ~ 0.8%). For the tape adhesion test, a 3M Scotch tape (3M: Scotch Magic Tape, 810-1-18D) was used.

### *3.2.2 Conventional and sc-$CO_2$ Catalyzation*

In the conventional catalyzation, the PET specimen was immersed in the catalyzation solution at 30.0 ± 1 °C for 30 min. For the sc-$CO_2$ catalyzation step, the sc-$CO_2$ equipment was provided by Japan Spectra Company. The reaction cell was made of stainless steel 316 lined with polyether ether ketone coatings on the inner wall, and the

inner volume was 50.0 ml. A piece of the PET specimen was placed in the reaction cell with 50.0 mg of $Pd(acac)_2$ and 30.0 mg of ε-caprolactam (99%). The sc-$CO_2$ catalyzation was conducted for 2.0 hr at 120.0 $\pm$ **1** °C and 15.0 MPa.

*3.2.3 Metal deposition*

No additional treatment was conducted after the catalyzation step. The conventionally catalyzed and sc-$CO_2$ catalyzed PET films were immersed into the Pt electroless plating solution for 30 min, 45 min, and 60 min at 70.0 $\pm$ **1** °C.

*3.2.4 Characterization*

The surface morphology and cross-section of the Pt metallized PET (Pt/PET) were observed by an optical microscope (OM, KEYENCE: VHV-5000) and a scanning electron microscope (SEM, HITACHI: S-4300SE). The crystal structure and phase of the Pt/PET were identified by an X-ray diffractometer (XRD, Rigaku: Ultima IV). The thickness of the Pt layers was evaluated by observing the cross-section by the SEM. The electrical resistance was examined by a four-point probe (Mitsubishi Chemical Analytech Co., Ltd.: MCP-T37). The adhesion test was conducted by firmly sticking a piece of the 3M tape with a 1 kg load to the specimen surface [3-2]. After removing the load and peeling the 3M tape off the specimen surface in sequence, the electrical resistance was measured again. To ensure reliability of the result, the adhesion test was conducted three times using different samples prepared under the same conditions. The tensile test was conducted by a universal testing machine (Shimadzu Corp.: Autograph Instron–type AG-1kNI). The electrical resistance of the tensile specimen was monitored by an electrical resistance meter (HIOKI E.E. CORPORATION.: RM3544) during the tensile test. The

fracture point of the specimen was determined by the point when the electrical resistance suddenly increased to an extremely high value as a result of short circuit.

### 3.3 Results and discussion

*3.3.1 Pt metallization of PET*

Surface appearances of the conventionally catalyzed and the sc-$CO_2$ catalyzed PET specimens after 60 min of the Pt deposition time are shown in Fig. 3-1(b). The PET specimen by conventional catalyzation remained clear and transparent showing only features of the as-received PET film. The conventional catalyzation was suggested to be ineffective to catalyze the PET specimen, and lead to the unsuccessful metallization result. On the contrary, the sc-$CO_2$ catalyzed PET specimen was fully covered with a layer of gray metal-like coatings after the Pt deposition step. The metal-like coatings were believed to be metallic Pt, and the metallized PET remained flexible after the Pt deposition step.

XRD patterns of the as-received PET film and the Pt metallized PET specimens prepared with the sc-$CO_2$ catalyzation step are shown in Fig. 3-2. Surfaces of the PET was entirely covered with the metal-like appearance when the Pt deposition time longer than 30 min was used. Therefore, only specimens with the Pt metallization of 30 min, 45 min and 60 min were characterized. The peak at $2\theta = 25°$ revealed the contribution from the PET [3-3]. Signals at around $2\theta = 39.9°$, 46.4°, 67.7°, 82.5° and 85.9° were evidences of the face-centered cubic (FCC) crystal structure of Pt (JCPDS card No 87-0647). Relative intensities of the Pt peaks increased and the PET XRD peaks gradually weakened following an increase in the Pt deposition time, which revealed the amount of Pt on the PET specimen increased with the Pt deposition time. Thickness of the Pt layer is described

in a later section. The Pt (111) peak became the XRD peak with the highest relative intensity when the Pt deposition time reached 45 min. Relative intensities of the Pt peaks did not vary much as the Pt deposition prolonged, which suggests the crystal structure did not change much as the Pt deposition time increased.

Morphologies of the Pt/PET with 30 min, 45 min and 60 min of the Pt deposition time are shown in Fig. 3-3. The surfaces were covered with small and relatively uniform-sized particles and large irregular shaped particles. As the Pt deposition time prolonged, there was no obvious change in the average sizes of the small uniform-sized and large irregular shaped particles, and an increase in the density of the irregular shaped particles was observed.

The thickness of the Pt layer was determined from the cross-sectional images. Examples of the cross-sectional images are shown in Fig. 3-3(d) to (f). The Pt layer thickness reached 0.20 μm after 30 min of the Pt deposition time, and it thickened to 0.32 μm and 0.41 μm when 45 min and 60 min, respectively, of the Pt deposition time was used. Fig. 3-4(a) shows the relationship between the Pt deposition time and the Pt layer thickness. The Pt layer thickness increased almost linearly as the Pt deposition time increased. Regarding the Pt layer growth rate, a complete Pt coverage of the PET surface was not achieved when the Pt deposition time was shorter than 30 min. Hence, the Pt growth rate were determined using the 30 min, 45 min and 60 min specimens. The Pt growth rate was 0.0067 μm/min in the in the first 30 min of the Pt deposition. For the Pt deposition time of 30 min to 45 min, the Pt growth rate was 0.0080 μm/min, and the Pt growth rate decreased to 0.0060 μm/min in the next 15 min interval. A plot of the Pt deposition time versus the Pt growth rate is provided in Fig. 3-4(a). In electroless plating, an incubation time is usually needed before the metal deposition starts, and the growth

rate would gradually decrease when the deposition time is long because of continuous consumption of the metal ions and reducing agents involved in the metal deposition [3-4]. Therefore, generally, the growth rate is expected to be low to almost zero during the period of the incubation time. Then, a constant growth rate is achieved before concentrations of the reactants in the plating solution drop to a certain level. In this study, the incubation time was suggested to be less than 30 min for the sc-$CO_2$ catalyzed PET specimen.

*3.3.2 Electrical resistance of Pt/PET*

The electrical resistances of the Pt/PET were summarized in Fig. 3-4(b). The Pt/PET prepared with 30 min of the Pt deposition time before the adhesion test showed a decent electrical resistance at 0.95 Ω with a small standard deviation. The result confirmed the PET specimen was fully covered by the Pt. As the Pt deposition time extended to 45 min and 60 min, the electrical resistances were reduced to 0.80 Ω and 0.54 Ω, respectively. The reduced electrical resistance was a result of an increase in the amount of Pt on the PET specimen, and this corresponded well the trend of the relative XRD peak intensity observed from the XRD characterization.

Some parts of the metallized Pt could be removed from the PET surface by the peeling motion of the tape in the tape adhesion test if the adhesion between the Pt and Pet is weak. Hence, the tape adhesion test was used to evaluate the reliability of the Pt layer on the PET. After the tape adhesion test, the electrical resistance of the Pt/PET with 30 min of the Pt deposition time increased to 1.76 Ω, which was an 85.3% increase. This increase in the electrical resistance was large, but the electrical resistance was still low and applicable toward electronic devices. For the Pt/PET with 45 min and 60 min of the

Pt deposition time, the electrical resistances increased to 1.50 Ω and 1.09 Ω, respectively, after the adhesion test. The increasing percentages were 87.5% and 101.9% for the Pt/PET with 45 min and 60 min of the Pt deposition time, respectively. Again, the Pt/PET with the longest Pt deposition time showed the lowest electrical resistance after the adhesion test, but the increasing percentage was the highest.

The resistance to the peeling motion of the tape in the tape adhesion test is suggested to be related to the size of the tape, weight applied in the tape adhesion test, interactions between the Pt layer and the PET substrate surface, and surface conditions of the Pt layer. The size of the tape and the weight were the same in evaluations of all specimens. The interaction between the Pt layer and the PET substrate is suggested to be mostly affected by the sc-$CO_2$ catalyzation. Again, the same sc-$CO_2$ catalyzation step was applied in the 30 min, 45 min and 60 min specimens. Therefore, the surface condition illustrated in Fig. 3-3 was thought to be the main cause leading to the increase in the increasing percentage of the electrical resistance after the tape adhesion test. The large irregularly shaped particles are suggested to be more likely to be removed after the tape adhesion test leading to an increase in the electrical resistance. Hence, the 60 min specimen showed the largest increasing percentage after the tape adhesion test.

### *3.3.3 Fracture strength*

Engineering stress-strain (SS) curves generated from the tensile test and the in-situ electrical resistances as the tensile test proceeded are provided in Fig. 3-5. In the three SS curves, the yield point is not clear, and the linearity in the elastic region is poor. The specimens were composite materials composed of an outer Pt layer and PET core in the cross-section, and this resulted the unclear yield point and the poor linearity. Regarding

the in-situ electrical resistances in the three specimens, all three of them increased almost linearily before the short circuit occurred. The short circuit was defined to be the condition when the in-situ electrical resistance suddenly reached an extremely high value during the tensile test.

For the mechanical strength, the unclear yield point and the poor linearity lead to difficulties in determination of the yield strength. The electrical resistance is a key property indicating performance of the Pt/PET in this study. Therefore, the stress value when the short circuit occurred between two ends of the dog-bone shaped specimen was used and reported as the fracture strength in this study. The fracture strengths are provided in Table 1. The fracture strength was 33.9 MPa for the Pt/PET with 30 min of the Pt deposition time. As the Pt deposition time increased to 45 min and 60 min, the fracture strength reached 52.3 MPa and 65.9 MPa.

The overall strength of a composite material is expected to increase when there is an increase in amount of the constituent material with a higher strength. The tensile strength of Pt is much higher than that of PET. Hence, an increase in the amount of the Pt layer in the Pt/PET is expected to cause an increase in the fracture strength. As shown in Fig. 3-4(a), the Pt layer thickness increased almost linearly with the Pt deposition time. Therefore, a positive relationship between the fracture strength and the Pt deposition time was an expected result.

### 3.4 Chapter Summary

Pt metallization of PET film was successfully achieved by electroless plating with the supercritical $CO_2$ catalyzation step. Sc-$CO_2$ functioned as the solvent, and Pd(II) acetylacetonate was used as the Pd catalyst source in the catalyzation step. The thickness

of the Pt layer increased linearly as the Pt deposition increased from 30 min to 60 min. The Pt layer thickness reached 0.20 μm after 30 min of the metal deposition time, and the Pt layer thickened to 0.41 μm as the deposition time extended to 60 min. For the as-metallized Pt/PET with 30 min of the Pt deposition time, the electrical resistance was 0.95 Ω, and the electrical resistance reduced to 0.54 Ω as the Pt deposition time prolonged to 60 min. The thickened Pt layer was the main course of the reduced electrical resistance. For the Pt/PET with 60 min of the Pt deposition, the electrical resistance merely changed to 1.09 Ω after the tape adhesion test, and the fracture strength was at 65.9 MPa. The low electrical resistances before and after the adhesion test and the high tensile strength in the Pt/PET reported in this study all revealed advantages of the sc-$CO_2$ catalyzation step in development of biocompatible and flexible electronics.

### 3.5 References


[3-1] M. Mitsumoto, C.Y. Chen, W.T. Chiu, T.F.M. Chang, Y. Watanabe, A. Jinno, H. Kurosu, M. Sone. Supercritical carbon dioxide-assisted platinum metallization of polyethylene terephthalate textile toward wearable device, Micro Nano Eng. 15 (2022) 100132. https://doi.org/10.1016/J.MNE.2022.100132

[3-2] P.-W. Cheng, C.-Y. Chen, T. Ichibayashi, T.-F.M. Chang, M. Sone, S. Nishimura, Supercritical carbon dioxide-assisted functionalization of polyethylene terephthalate (PET) toward flexible catalytic electrodes. J. Supercrit. Fluids. 180 (2022) 105455. https://doi.org/10.1016/J.SUPFLU.2021.105455.

[3-3] Y. Li, D. J. White, R. L. Peyton, Composite material from fly ash and post-consumer PET. Resour. Conserv. Recycl. 24 (1998) 87-93. https://doi.org/10.1016/S0921-3449(98)00041-X.

[3-4] J. Flis, D.J. Duquette, Catalytic Activity of Iron, Nickel, and Nickel-Phosphorus in Electroless Nickel Plating. J. Electrochem. Soc. 131 (1984) 34. https://doi.org/10.1149/1.2115538.

### 3.6 Figures

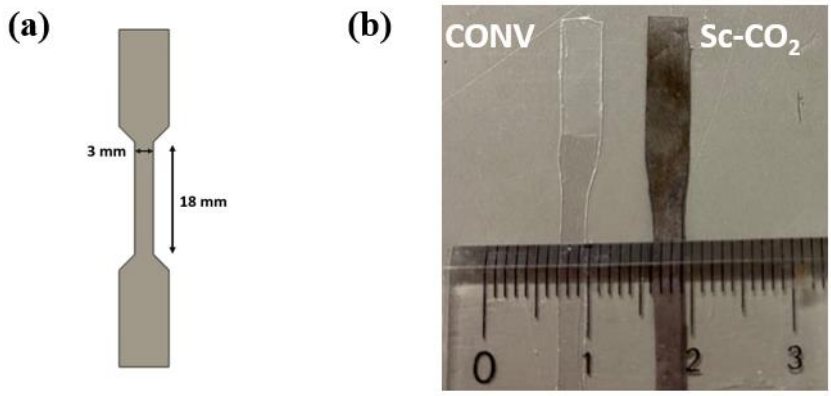


**Figure 3-1**. (a) Illustration of the dog-bone shaped specimen. (b) Appearances of comparison of metalized PET catalyzed in conventional solution and sc-$CO_2$

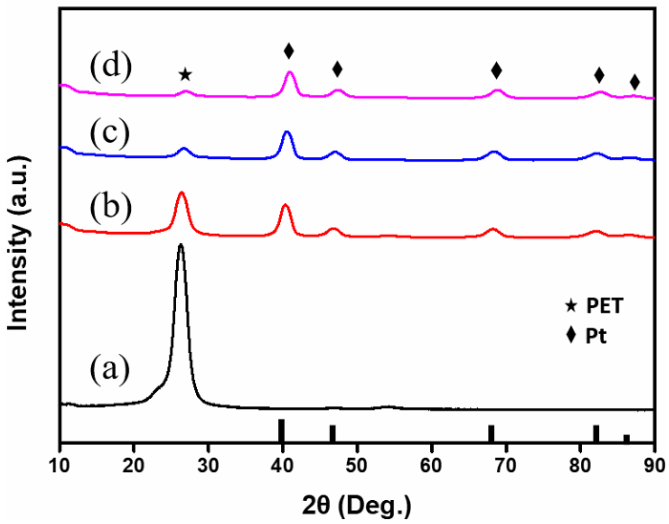


**Figure 3-2**. XRD patterns of the (a) PET film and the Pt/PET prepared with (b) 30 min, (c) 45 min and (d) 60 min of the Pt deposition time. (JCPDS card No 87-0647)

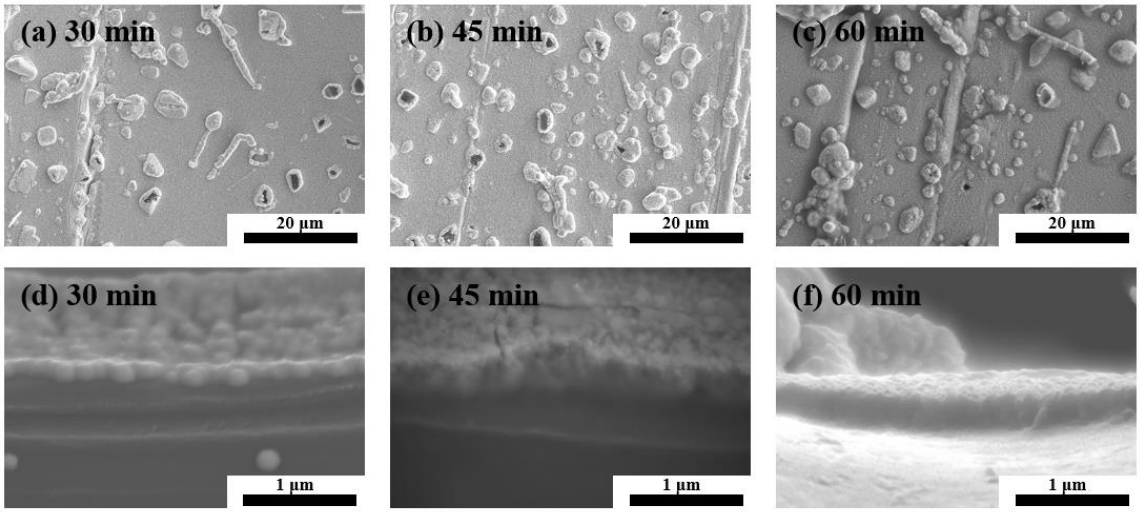


**Figure 3-3**. Surface morphology of Pt metallized PET treated by the sc-$CO_2$ catalyzation follow by (a) 30 min, (b) 45 min, and (c) 60 min of the Pt deposition time, and cross-sectional view of the specimen with (d) 30 min, (e) 45 min, and (f) 60 min of the Pt deposition time.

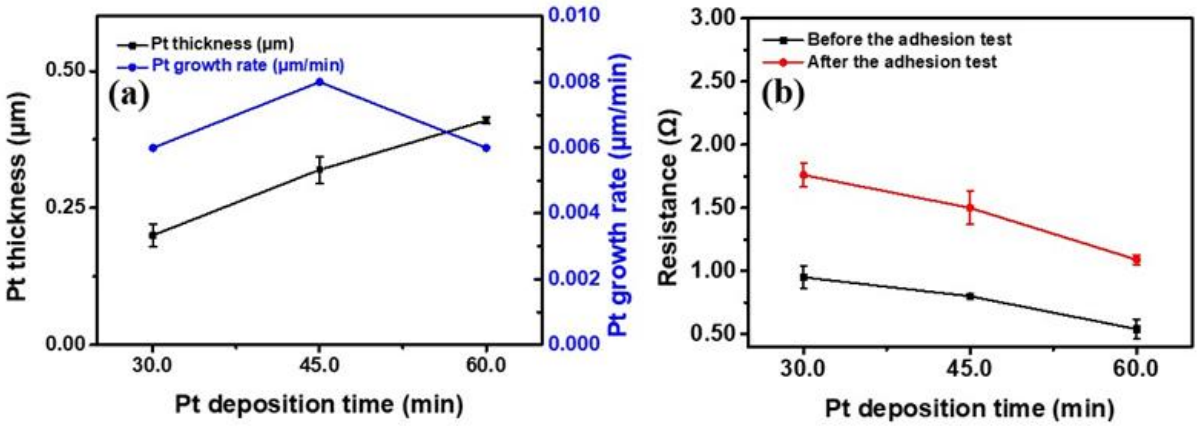


**Figure 3-4**. Plots of the (a) Pt deposition time versus the Pt layer thickness and the Pt growth rate, and the (b) Pt deposition time versus the electrical resistance.

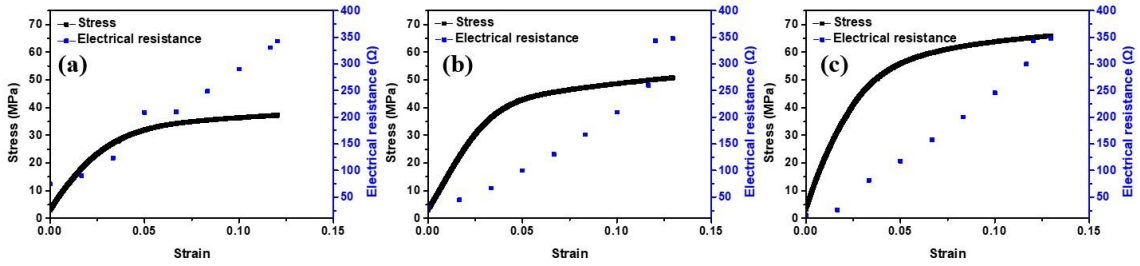


**Figure 3-5.** Engineering stress-strain curve of the engineering stress-strain curves and in-situ electrical resistances of the Pt/PET prepared with (a) 30 min (b) 45 min (c) 60 min of the Pt deposition time.

## 4.7 Tables

**Table 4-1**. Fracture strength of the Pt/PET.

| Pt deposition time (min) | Pt thickness (μm) | Fracture stress (MPa) |
|---|---|---|
| 30 | 0.20 ± 0.019 | 33.9 ± 2.84 |
| 45 | 0.32 ± 0.024 | 52.1 ± 3.42 |
| 60 | 0.41 ± 0.006 | 65.7 ± 8.96 |

CHAPTER 4

# *Metallization of 3D-printed polymer via sc-$CO_2$ assisted electroless plating*

## 4.1 Introduction

In the previous chapter, the flexible electronic components are achieved and demonstrated the exclusive performance by the sc-$CO_2$ treatment. Therefore, the next target is to develop a rapid fabrication approach using 3D printing technology. However, the weak chemical resistance of 3D-printed substrates has made metallization as a challenge. To address this issue, a supercritical carbon dioxide (sc-$CO_2$) assisted electroless plating process was utilized in this chapter to successfully metalize a 3D-printed substrate. Ni-P coatings were deposited onto the catalyzed polymer structure using a commercially available Ni-P solution. Electrical resistance of the Ni-P metallized polymer structure was measured using the four-point probe method, and the adhesion of the Ni-P coating on the polymer structure was evaluated using a tape adhesion test.

## 4.2 Experimental

### *4.2.1 3D printing*

The 3D printer (Mars UV Photocuring LCD MSLA 3D Printer) and photopolymer

resin (Standard LCD UV-Curing Photopolymer Rapid Resin for 3D Printers) were purchased from Elegoo Inc. The 3D-printed polymer structure was prepared by a series of printing and exposure steps. In the printing step, the photopolymer resin would be printed into a layer of square mesh patterns having a resolution of 50 μm by 50 μm in X-Y plane via the LCD active mask and the minimum layer thickness was about 100 μm. Then each layer of the square mesh patterns would be exposed to UV light at $\lambda$ = 405 nm for 6 s. A 3D-printed structure with a desired shape was prepared by repeating the printing and exposure steps controlled by a computer software. Two designs of the 3D-printed polymer structure were prepared. One was with the shape of a hammer to demonstrate the ability to metallize 3D-printed polymer structures having a complex design, the other one was a square-pad for evaluation of the properties as shown in Fig. 4-1. For the hammer, dimensions of the head were 38 mm × 20 mm × 15 mm, and the length and diameter of the handle were 25 and 4.5 mm, respectively. The square-pad was 20 mm on each side, and the thickness was 2 mm.

*4.2.2 Catalyzation*

As a comparison with the sc-$CO_2$ catalyzation, conventional catalyzation was conducted with a commercially available catalyzation solution (ICP Accera KCR, Okuno Chemical Industries Co., Ltd, Japan). The immersion time was 30 min, and the temperature was maintained at 30 °C. The sc-$CO_2$ equipment was purchased from Japan Spectra Company. The reaction cell was made of stainless steel 316 with polyether ether ketone coating on the inner wall, and the inner volume was 50 ml. The temperature and pressure were maintained at 70 °C and 15 MPa, respectively. Density of $CO_2$ at 70 °C and 15 MPa is 0.50588 g/ml [4-1]. 100 mg of $Pd(hfa)_2$ (Sigma-Aldrich, USA) was introduced

into the reaction cell, and the concentration would be 0.4 wt% in sc-$CO_2$. The catalyzation time was 2 hr.

*4.2.3 Metal deposition*

The metal deposition step was conducted with a commercially available Ni-P solution (Top Nicoron VS-LF, Okuno Chemical Industries Co., Ltd, Japan). The Ni-P solution had a composition of nickel chloride (9 wt%), sodium hypophosphite (12 wt%), complexing agent (12 wt%), and ion-exchanged water (67 wt%). Temperature of the Ni-P solution was kept at 70, 80 or 90 °C. The deposition time was 3, 10 or 30 min.

*4.2.4 Characterization*

Surface morphology of the Ni-P metallized 3D polymer structure was observed by a scanning electron microscope (SEM, S-4300SE, HITACHI, Japan). Crystal structure of the deposited Ni-P coating was identified by X-ray diffraction (XRD, Ultima IV, Rigaku, Japan). Thickness of the Ni-P coating was estimated by observing the cross-section of the Ni-P/polymer structure by the SEM. The polymer substrate was hard and brittle after the exposure step, hence the cross-section was prepared by cutting back-side of the Ni-P metallized polymer substrate then break the sample into two halves along the cutting mark. The electrical resistance was evaluated by a four-point probe (MCP-T37, Mitsubishi Chemical Analytech Co., Ltd. Japan). For the tape adhesion test [4-2], a piece of 3M tape (810-1-18D Scotch Magic Tape, 3M, USA) was firmly stuck to the sample surface by applying a 1-kg load and peeled off afterward. The square-pad samples were used in the morphology observation, XRD, electrical resistance and tape adhesion test characterizations.

## 4.3 Results and Discussion

### *4.3.1 Ni-P metallization of 3D-printed polymer*

Overviews of hammer-shaped 3D-printed polymer structures catalyzed by the conventional method and the sc-$CO_2$ catalyzation followed by metal deposition at 90 °C are shown in Fig. 4-2(a) and Fig. 4-2(b), respectively. An US quarter-dollar coin was also demonstrated as a scale and color comparison. Color of the as-prepared photopolymer resin was red with some transparency. Appearance of the 3D-printed hammer hardly changed after the metal deposition step when the conventional catalyzation was used as shown in Fig. 4-2(a), which indicated the conventional catalyzation was ineffective to deposit Pd catalysts on surfaces of the 3D-printed polymer. On the other hand, the 3D-printed hammer catalyzed in sc-$CO_2$ showed metal-like surfaces after the metal deposition step as shown in Fig. 4-2(b), which revealed Pd seeds were successfully decorated on the 3D-printed polymer by the sc-$CO_2$ catalyzation and worked as the catalyst in the later metal deposition step. Appearance of the sample in Fig. 4-2(b) showed similar metallic luster to the metal coin.

The as-deposited Ni-P was expected to be amorphous. The XRD signals at around $2\theta = 20°$ were contributed by the 3D-printed polymer as shown in Fig. 4-2(c) to Fig. 4-2(e). The signals at around $2\theta = 45°$ were caused by the amorphous Ni-P. Intensities of the Ni-P signals increased and the polymer signals decreased along with an increase in the metal deposition time, which suggested an increase in amount of Ni-P deposited on the surface when a longer metal deposition time was applied.

The surface morphology of Ni-P metallized 3D-printed square-pad structures catalyzed in sc-$CO_2$ could be observed from the SEM images shown in Fig. 4-3. The

sample with the deposition temperature at 90 °C and the deposition time at 3 min showed checkerboard-like surface as shown in Fig. 4-3(a), and one side of the square pattern was about 50 μm long, which was the same as the resolution of the square mesh patterns in the printing step of the 3D-printed square-pad structures. This implied the square pattern observed from the SEM was simply reflecting surface conditions of the as-printed sample [4-3,4-4]. The checkerboard morphology became less obvious as the deposition time increased to 10 and 30 min as shown in Fig. 4-3(b) and Fig. 4-3(c), respectively. The surface was found to be covered by cauliflower-like nodules when 30 min of the deposition time was used. The nodule morphology is commonly observed in electroless plated materials [4-5] because of the tendency of deposited Ni-P to have isotropic growth to reduce the surface energy as the deposition proceed [4-6].

The thickness of the Ni-P layer reached 1.7 μm when 3 min of the deposition time was used for the 3D-printed polymer catalyzed in sc-$CO_2$ as shown in Fig. 4-3(d). The thickness increased to 2.4 and 4.3 μm when the deposition time increased to 10 and 30 min, respectively. The effect of the metal deposition time on the Ni-P layer thickness is summarized in Fig. 4-4(a). The increased thickness as the deposition time increase corresponded well to results observed from the XRD (Fig. 4-2(c) to (e)) and the surface morphology (Fig. 4-3(a) to Fig. 4-3(c)), which the XRD responses from the substrate gradually decreased and the peak intensities contributed by the Ni-P gradually increased as the deposition time prolonged. Also, the leveling effect [4-7] observed in the sample with the deposition time at 30 min was also a result of the prolonged metal deposition time, which surface conditions (the square mesh patterns) of the 3D-printed structure became unobservable as the covering Ni-P layer thickened.

*4.3.2 Electrical resistance of Ni-P metalized 3D-printed polymer*

Effects of the deposition temperature on electrical resistance of the Ni-P metallized 3D-printed polymer structures are shown in Fig. 4-4(b). In previous sections, the samples were metallized at a deposition temperature of 90 °C, because this temperature was the optimum temperature found in this study. As shown in Fig. 4-4(b), an increase in the resistance was observed when a lower deposition temperature was used. The resistance was 0.61 Ω when the temperature was at 90 °C, and the resistance increased to 1.77 and 7.27 Ω when 80 and 70 °C was used. As suggested by results shown in Fig. 4-2(a) and (b), conditions of the catalyst deposited on the polymer play an important role on quality of Ni-P deposited on the polymer. According to a study on thermal stability of $Pd(hfa)_2$ [4-8], thermal degradation of $Pd(hfa)_2$ occurs when the temperature reaches 90 °C. As the thermal degradation occurred, Pd embedded in the organometallic complex structure would be released to form metallic Pd. After the sc-$CO_2$ catalyzation step, Pd ions in the Pd(hfa) compounds were expected to stay in the oxides state with no catalytic activity since the temperature used in the sc-$CO_2$ catalyzation was 70 °C and no reducing agent was introduced. After having contact with reducing agents in the Ni-P solution, the $Pd(hfa)_2$ would be decomposed and reduced to release metallic Pd, which became the catalyst in the deposition of Ni-P. This is one of the causes of the incubation time observed in electroless plating [4-9] Therefore, the metal deposition temperature was suggested to have great influence on reduction of the $Pd(hfa)_2$ in the initial state of the metal deposition step, and eventually affected qualities of the Ni-P layer.

In Fig. 4-4(c), electrical resistances of the Ni-P metallized 3D-printed polymer structures were evaluated before and after the tape adhesion test to reveal reliability of

the samples. The resistances were 0.61, 0.15, and 0.03 Ω for the sample with 3, 10, and 30 min of the deposition time, respectively, before the tape adhesion test. The reduced resistance as the deposition time increased was suggested to be results of the thickened Ni-P layer. After the tape adhesion test, the resistances were 0.76, 0.48, and 0.04 Ω for the sample with 3, 10, and 30 min of the deposition time, respectively. Generally, the resistance did not change much after the tape adhesion test revealing advantages of the sc-$CO_2$ assisted electroless plating process in metallization of 3D-printed polymer structures.

### 4.4 Chapter Summary

Metallization of 3D-printed polymer structures was achieved by sc-$CO_2$ assisted electroless plating process to demonstrate the potential for rapid fabrication of electronic components. The catalyzation step was conducted in sc-$CO_2$ with $Pd(hfa)_2$ as source of the Pd catalyst. Thickness of the metallized Ni-P reached 1.7 μm after 3 min of the metal deposition time, and the Ni-P layer thickened to 4.3 μm as the deposition time extended to 30 min. The electrical resistance reached 0.61 Ω after 3 min of metal deposition time, and the resistance was lowered to 0.03 Ω after 30 min of the deposition time. After the tape adhesion test, electrical resistance of the Ni-P metallized 3D-printed polymer structure merely changed to 0.04 Ω for the sample with 30 min of the deposition time.

## 4.5 References


[4-1] E.W. Lemmon, Thermophysical properties of fluid systems. NIST Chemistry WebBook (1998).

[4-2] W.-T. Chiu, C.-Y. Chen, T.-F.M. Chang, T. Hashimoto, H. Kurosu and M. Sone, Ni–P and $TiO_2$ codeposition on silk textile via supercritical $CO_2$ promoted electroless plating for flexible and wearable photocatalytic devices. Electrochim. Acta 294 (2019) 68. https://doi.org/10.1016/j.electacta.2018.10.076

[4-3] Z.-X. Low, Y.T. Chua, B.M. Ray, D. Mattia, I.S. Metcalfe, D.A. Patterson, Perspective on 3D printing of separation membranes and comparison to related unconventional fabrication techniques. J. Membr. Sci. 523 (2017) 596. https://doi.org/10.1016/j.memsci.2016.10.006

[4-4] T. Hermann Becker, D. Dimitrov, The achievable mechanical properties of SLM produced Maraging Steel 300 components. Rapid Prototyp J 22 (2016) 487. https://doi.org/10.1108/RPJ-08-2014-0096

[4-5] A.El-Sherik, U. Erb, Synthesis of bulk nanocrystalline nickel by pulsed electrodeposition. J. Mater. Sci. 30 (1995) 5743. https://doi.org/10.1007/BF00356715

[4-6] S.H.M. Anijdan, M. Sabzi, M.R. Zadeh, M. Farzam, The effect of electroless bath parameters and heat treatment on the properties of Ni-P and Ni-P-Cu composite coatings. Mater. Res. 21 (2018). https://doi.org/10.1590/1980-5373-mr-2017-0973

[4-7] T.-F.M. Chang, M. Sone, A. Shibata, C. Ishiyama, Y. Higo, Bright nickel film deposited by supercritical carbon dioxide emulsion using additive-free Watts

bath. Electrochim. Acta 55 (2010) 6469. https://doi.org/10.1016/j.electacta.2010.06.037

[4-8] X. Zhao, K. Hirogaki, I. Tabata, S. Okubayashi, T. Hori, A new method of producing conductive aramid fibers using supercritical carbon dioxide. Surf. Coat. Technol. 201 (2006) 628. https://doi.org/10.1016/j.surfcoat.2005.12.021

[4-9] K. Tokuoka, C.-Y. Chen, T.-F.M. Chang, W.-T. Chiu, H. Kurosu, M. Sone, Metallization of PET textile utilizing supercritical $CO_2$ catalyzation. Microelectron Eng 223 (2020) 111233. https://doi.org/10.1016/j.mee.2020.111233

## 4.6 Figures

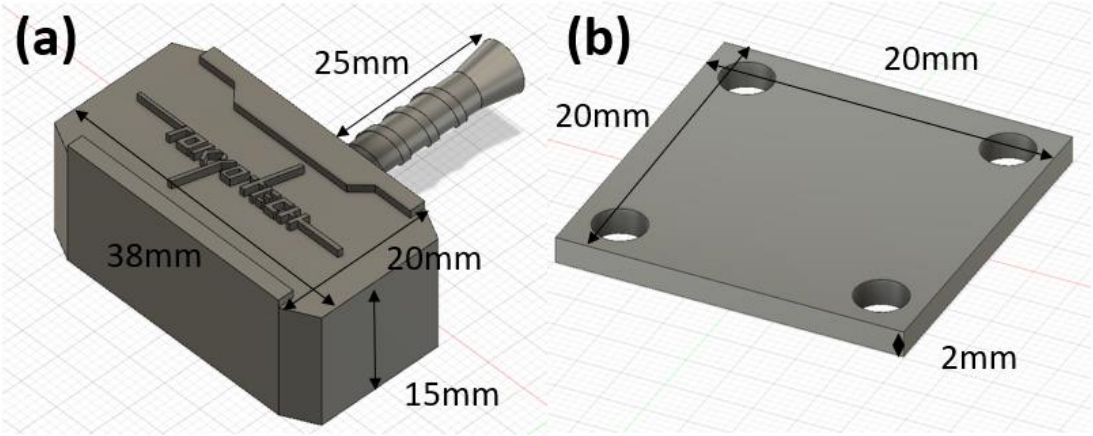


**Figure 4-1**. Schematic diagrams of the 3D-printed (a) hammer and (b) square-pad structures.

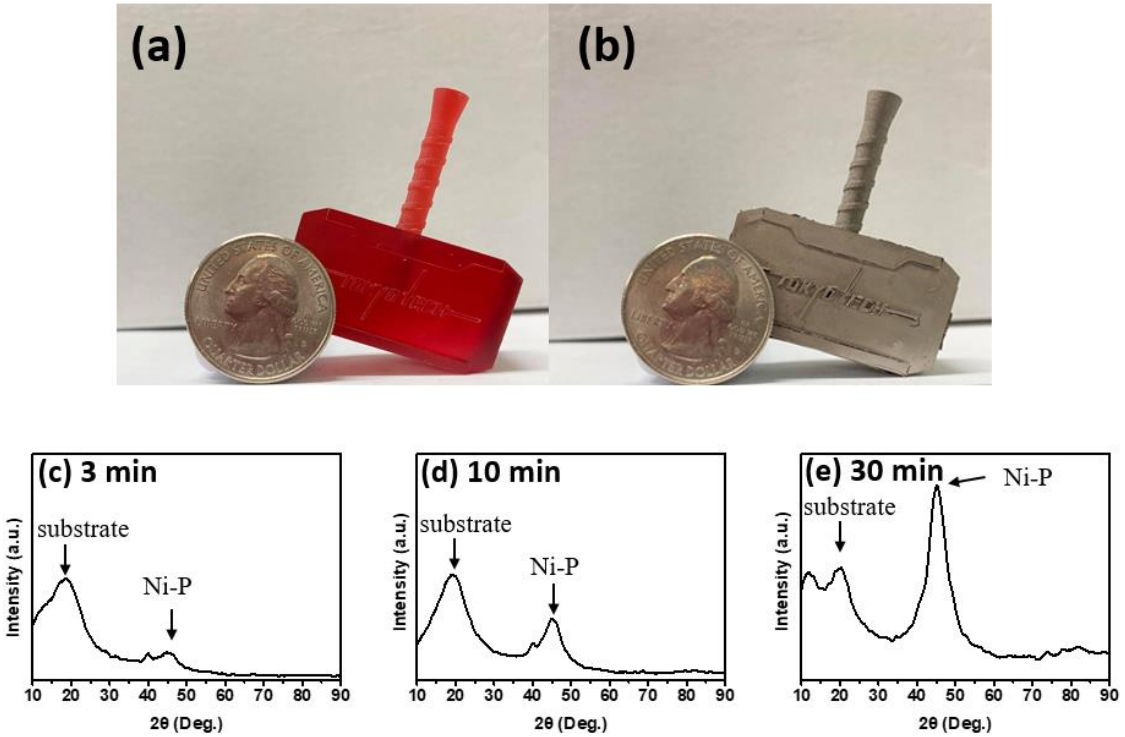


**Figure 4-2**. Metalized 3D-printed hammer structures catalyzed in (a) conventional solution and (b) sc-$CO_2$, and XRD of the metallized 3D-printed square-pad structures treated by the sc-$CO_2$ catalyzation follow by (c) 3, (d) 10, and (e) 30 min of the metal deposition time and the deposition temperature at 90 °C.

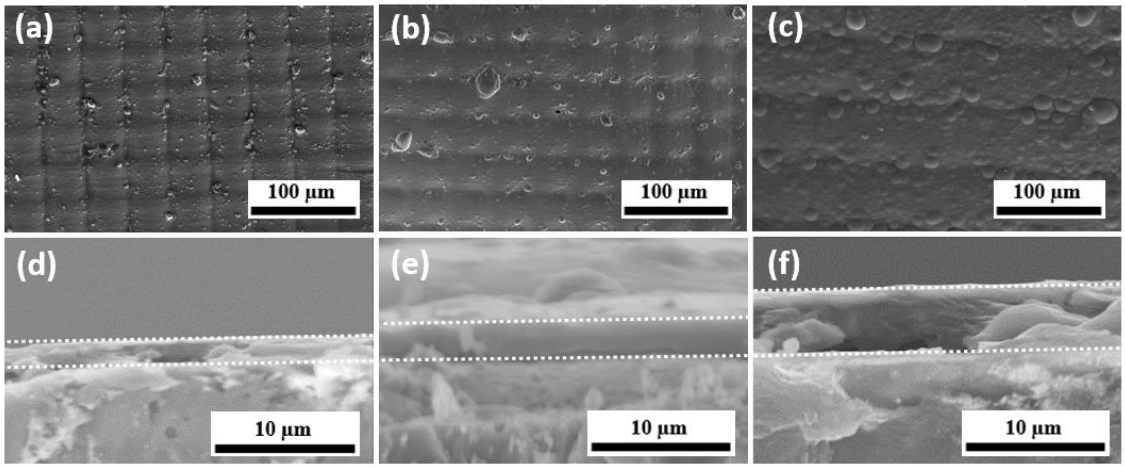


**Figure 4-3**. Surface morphology of Ni-P metallized 3D-printed square-pad structures treated by the sc-$CO_2$ catalyzation follow by (a) 3, (b) 10, and (c) 30 min of the metal deposition time, and cross-sectional view of the samples with (d) 3, (e) 10, and (f) 30 min of the metal deposition time and the deposition temperature at 90 °C.

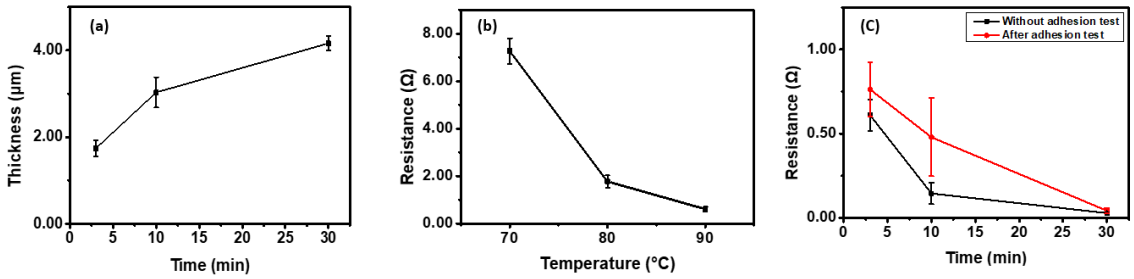


**Figure 4-4**. Plots of (a) the metal deposition time versus the Ni-P layer thickness with the deposition temperature at 90 °C, (b) the metal deposition temperature versus the electrical resistance with the deposition time fixed at 3 min, and (c) the metal deposition time versus the electrical resistance with the deposition temperature maintained at 90 °C.

CHAPTER 5

# *Sc-$CO_2$ assisted gold metallization of 3D-printed polymer and the tensile strength*

## 5.1 Introduction

In chapter 5, successful Ni-P metallization of 3D-printed polymer structures by a supercritical carbon dioxide (sc-$CO_2$) assisted electroless plating process demonstrated the potential for rapid fabrication of electronic components. However, to advance the results towards practical applications, the mechanical properties need to be evaluated. In addition to the adhesion test, a tensile test was conducted in this chapter. Furthermore, the application fields of the 3D-printed substrate were expanded by depositing a sacrificial Ni-P layer for sequential gold deposition.

## 5.2 Experimental

### *5.2.1 3D printing*

The 3D printer (MARS 2 PRO MONO LCD MSLA resin 3D printer) and photopolymer resin (Standard LCD UV-Curing Photopolymer Rapid Resin for 3D Printers) were purchased from Elegoo Inc. The resin was composed of phenolic epoxy

resin (40-50 wt%), 6-hexanediol diacrylate (20-40 wt%), color pigment (2-5%), and 1-hydroxycyclohexyl phenyl ketone (3-5 wt%). UV light at $\lambda$ = 405 nm was used as the light source in photopolymerization of the resin. For the tensile test, a dog-bone shaped structure was prepared. A schematic diagram of the dog-bone shaped structure is provided in Fig. 5-1(a).

*5.2.2 Catalyzation*

A commercial catalyzation solution (Okuno Chemical Industries Co., Ltd.: ICP Accera KCR) was used to catalyze the 3D printed polymer structures to be used as comparison treated by the sc-$CO_2$ catalyzation. For the conventional catalyzation step, the experimental conditions were 30°C and 30 min. For the sc-$CO_2$ catalyzation step, the sc-$CO_2$ equipment was provided by Japan Spectra Company. The reaction cell was constructed by stainless steel 316 with polyether ether ketone coating on the inner wall, and the inner volume was 50.0 ml. The 3D printed polymer structure and 50 mg of palladium bis-hexafluoroacetylacetonate ($Pd(hfa)_2$, Sigma-Aldrich) were placed in the reaction cell. After sealing the reaction cell properly, liquidized $CO_2$ was pumped into the reaction. The pressure was controlled at 15 MPa, and the temperature was at 70 °C. The catalyzation time was 1.0 hr.

*5.2.3 Metal deposition*

After the catalyzation step, the catalyzed 3D printed polymer structures were immersed into a Ni-P electroless plating solution (Okuno Chemical Industries Co., Ltd: Top Nicoron VS-LF) for 3.0 min at 70.0°C. The Ni-P plating solution is composed of nickel chloride (9 wt%), sodium hypophosphite (12 wt%), complexing agent (12 wt%), and ion-exchanged water (67 wt%). In electroless plating of gold [1], decoration of less

noble metals on the catalyzed substrate is required to be used as the sacrificial material before deposition of gold. And, Ni-P was chosen as the sacrificial material in this study. In addition, a sensitization step by immersing the Ni-P decorated 3D printed polymer structures in a 0.1 mM $KAuCl_4$ (99.995%, Sigma-Aldrich) solution for 1hr at 30.0 °C was conducted. Then the Ni-P decorated/$KAuCl_4$ sensitized/3D printed polymer structures were placed in a commercially available gold electroless plating solution (MATEX Japan Co., Ltd.: Non-Cyanide Electroless Solution, and the solution contained 2 g/L of Au and pH at 7) for 15.0 min, 30.0 min and 45.0 min at 65° C to cover the entire surface with gold.

*5.2.4 Characterization*

Surface morphologies and cross-section of the gold metallized 3D printed polymer structures were observed by a scanning electron microscope (SEM, HITACHI: S-4300SE). The thickness of the gold layer was determined through observing the cross-section, and the thickness of at least five locations was obtained and averaged to be used as the reported thickness. Crystal structures and phase of the gold metallized 3D printed polymer structures were identified by X-ray diffraction (XRD, Rigaku: Ultima IV). The electrical resistance was examined by a four-point probe (Mitsubishi Chemical Analytech Co., Ltd.: MCP-T37). Intactness of the gold layer on the 3D printed polymer structures was investigated by a tape adhesion test [5-1, 5-2]. The tape adhesion test was conducted by firmly sticking a piece of 3M Scotch® tape onto the gold metallized sample surface with a 1 kg load. After removing the load and peeling the tape off the sample surface in sequence, the electrical resistance was measured again. The tape adhesion test was conducted three times using different samples prepared under same conditions to provide

a reliable result. The tensile test was conducted by a universal testing machine (Shimadzu Corp.: Autograph Instron–type AG-500NI). The electrical resistance of the dog-bone shaped structure was monitored by an electrical resistance meter (HIOKI E.E. CORPORATION.: RM3544) during the tensile test to determine the fracture point. Also, a video (Canon: HFR32) was taken during the tensile test.

## 5.3 Results and discussion

### *5.3.1 Au metallization of 3D-printed polymer*

Surface appearances of the 3D printed dog-bone shaped structures after the gold deposition step are provided in Fig. 5-1(b). The original color of the photopolymer resin is grey. The conventional catalyzation treated sample remained the color of the photopolymer resin after the gold deposition step, and this revealed unsuccessful metallization of the 3D printed polymer structures. On the other hand, the gold metallization was successful for the sc-$CO_2$ catalyzed samples, which showed metal-like golden color after the gold deposition step. The results suggested the conventional catalyzation was ineffective in decoration of Pd catalyst seeds on the 3D printed polymer structure, hence, the gold deposition was not possible for the conventional catalyzation treated sample.

X-ray diffraction patterns of the as-printed polymer structure is provided in Fig. 6-2(a). Signals at around $2\theta = 20°$ were contributed by the solidified photopolymer resin. After decoration of Ni-P on the sc-$CO_2$ catalyzed sample (Fig. 5-2(b)), a broad peak at signals at around $2\theta = 45°$ was observed, and this suggested presence of amorphous Ni-P, which is commonly acquired in Ni-P obtained by electroless plating [5-3]. After the gold deposition, the XRD patterns are shown in Fig. 5-2(c) to (e). Signals at around $2\theta =$

40°, 45°, 65°, 78° and 83° could be assigned to face-centered cubic (FCC) crystal structure of gold (JCPDS card No 46-1043). In Fig. 5-2(c), contributions from the photopolymer resin were obvious, and the two FCC gold peaks at $2\theta = 40°$ and 45° were not that sharp, which is suggested to be influenced by the amorphous Ni-P, in the 15.0 min gold metallized sample. As the gold deposition time increased to 30.0 min and 45.0 min, relative intensities of the photopolymer resin gradually decreased, and influences of the amorphous Ni-P became less observable. These findings suggested an increasing trend of the amount of gold deposited on the sample.

Surface conditions of the gold metallized samples were evaluated from the SEM images shown in Fig. 5-3(a) to (c). In Fig. 5-3(a), surfaces of the 15.0 min sample were covered with many tiny particles, and these particles were believed to be gold. Some portion of the surface showed a darker color than the color of the tiny particles, and this was suggested to be regions still not covered with gold. As the gold deposition time increased to 30.0 min, sizes of the particles increased, and the entire surface was covered with the particles as shown in Fig. 5-3(b). In Fig. 5-3(c), the average size of the particles did not change much, but boundaries of the particles became less obvious as the gold deposition time extended to 45.0 min.

Examples of the cross-sectional images used to determine the gold layer thickness are provided in Fig. 5-3(d) to (f). The gold layer thickness reached 0.48±0.11 μm after 15.0 min of the gold deposition time, and it thickened to 0.92±0.12 μm and 1.23±0.26μm as the gold deposition time prolonged to 30.0 min and 45.0 min, respectively. An increase in the gold layer thickness corresponded well with the relative XRD signal intensity (Fig. 5-2(c) to (e)) and surface condition (Fig. 5-3(a) to Fig. 5-3(c)) results, which the amount of gold on the sample increased following an increase in the gold deposition time. The

relationships between the gold deposition time, gold layer thickness and gold growth rate were plotted and shown in Fig. 5-4(a). The gold growth rate in the first 15.0 min interval of the gold deposition time was calculated to be 0.032 μm/min, and the gold growth rate gradually decreased to 0.029 μm/min and 0.021 μm/min for the second and third 15.0 min interval, respectively, of the gold deposition time. Reduction of the gold growth rate was suggested to be a result of a decrease in the concentration of reactive species in the gold electroless plating solution.

*5.3.2 Electrical resistance of Au Metalized 3D-printed polymer*

The electrical resistance of the 15.0 min sample was 0.70 Ω, and it reduced to 0.28 Ω and 0.15 Ω, indicating an improved electrical conductivity, as the gold deposition time extended to 30.0 min and 45.0 min, respectively. After the tape adhesion test, the electrical resistances slightly increased to 0.83 Ω, 0.35 Ω and 0.18 Ω for the 15.0 min, 30.0 min and 45.0 min samples, respectively. The results are summarized in Fig. 5-4(b). Generally, the electrical resistance remained at a low level after the tape adhesion test, and this demonstrated the strong interaction between the gold layer and the 3D printed structure by the sc-$CO_2$ catalyzation in metallization of 3D printed polymer structures.

*5.3.3 Fracture strength*

The fracture strength ($\sigma_F$) of the as-printed dog-bone shaped structure was 23.0 MPa. After the gold metallization, the fracture strength increased to 34.9 MPa for the 15.0 min sample, and the fracture strength reached 39.7 MPa and 47.6 MPa as the gold deposition time increased to 30.0 min and 45 min, respectively. The engineering stress-engineering strain curves for each sample are provided in Fig. 5-5. Fig. 5-4(c) shows the

relationship between the gold layer thickness and the fracture strength. In general, strengthening of the 3D printed structure was obtained by depositing more gold on the sample. The fracture strength of pure gold is 120 MPa [5-4], which is much larger than the fracture strength then the as-printed dog-bone shaped structure. Therefore, it was expected to see an increase in the fracture strength after the gold metallization.

In a further analysis on the contribution of the metallized gold to the fracture strength, a value of the fracture force divided by the area of the metallized gold in the cross-section ($\sigma_{F,Au}$) was calculated as indicated in the following equation:

$$\sigma_{F,Au} = \frac{The\ force\ when\ fracture\ occurs}{Cross\text{-}seciontal\ area\ of\ the\ \ gold\ in\ the\ sample}$$

A plot of the gold layer thickness versus the $\sigma_{F,Au}$ is provided in Fig. 5-4(c). A decreasing trend was observed following an increase in the amount of gold metallized onto the 3D printed structure. In mechanical characterization of small-sized metal-based materials, the mechanical strength is reported to be dependent on the size of the sample used in the mechanical test, which is known as the sample size effect [5-5]. Usually, a smaller-is-stronger is reported when reducing the sample size from bulk-size to micro-scale or smaller. The higher $\sigma_{F,Au}$ obtained as the gold layer thickness decreased is to some extend similar to the smaller-is-stronger phenomenon in the sample size effect.

## 5.4 Chapter summary

Additive manufacturing of gold metallized 3D structures was demonstrated in this study. Complete gold metallization of the 3D printed structures was realized by sc-$CO_2$ assisted electroless plating. The sc-$CO_2$ was employed as a solvent to promote interaction between the Pd catalyst and surfaces of the 3D printed structures in the catalyzation step, and this eventually contributed to the complete gold metallization.

Thickness of the gold layer reached 0.48 μm after 15.0 min of the gold deposition time, and the thickness was elevated to 1.23 μm as the gold deposition time increased to 45.0 min. The electrical resistance showed a negative correlation with the gold deposition time. The sample with 15.0 min of the gold deposition time showed the electrical resistance at 0.70 Ω, and it was reduced to 0.15 Ω when the gold deposition time was extended to 45.0 min. For the 45.0 min sample, the electrical resistance slightly worsened to 0.18 Ω. In addition, the strengthening was observed in the gold metallized samples, and the highest fracture strength was 47.6 MPa for the 45.0 min sample. In conclusion, the gold metallized 3D printed structures reported in this study are promising materials toward electronic components by the low electrical resistance, resistant again the tape adhesion test, and promoted tensile fracture strength.

## 5.5 References


[5-1] P.W. Cheng, C.Y. Chen, T. Ichibayashi, T.F.M. Chang, M. Sone, S. Nishimura, Supercritical carbon dioxide-assisted functionalization of polyethylene terephthalate (PET) toward flexible catalytic electrodes. J. Supercrit. Fluids 180 (2022) 105455. https://doi.org/10.1016/J.SUPFLU.2021.105455

[5-2] P.W. Cheng, C.Y. Chen, T. Ichibayashi, T.F.M. Chang, M. Sone, S. Nishimura, Metallization of 3D-printed polymer structures via supercritical carbon dioxide-assisted electroless plating. *MRS Commun*. 11 (2021) 278. https://doi.org/10.1557/S43579-021-00022-2

[5-3] J.Y. Song, J. Yu, Thin Solid Films 415 (1984) 167.https://doi.org/10.1016/S0040-6090(02)00556-4

[5-4] S.B. Son, H, Roh. S.H. Kang, H.S. Chung, D.H. Kim, Y.S. Choi, J.S. Cho, J. T. Moon, K.H. Oh, Relationship between microstructure homogeneity and bonding stability of ultrafine gold wire. Gold Bull. 44 (2011) 231-237. https://doi.org/10.1007/s13404-011-0035-4

[5-5] A.T. Jennings, M.J. Burek, J.R. Greer, Microstructure versus Size: Mechanical properties of electroplated single crystalline Cu nanopillars. Phys. Rev. Lett. 104 (2010) 135503.https://doi.org/10.1103/PhysRevLett.104.135503

## 5.6 Figures

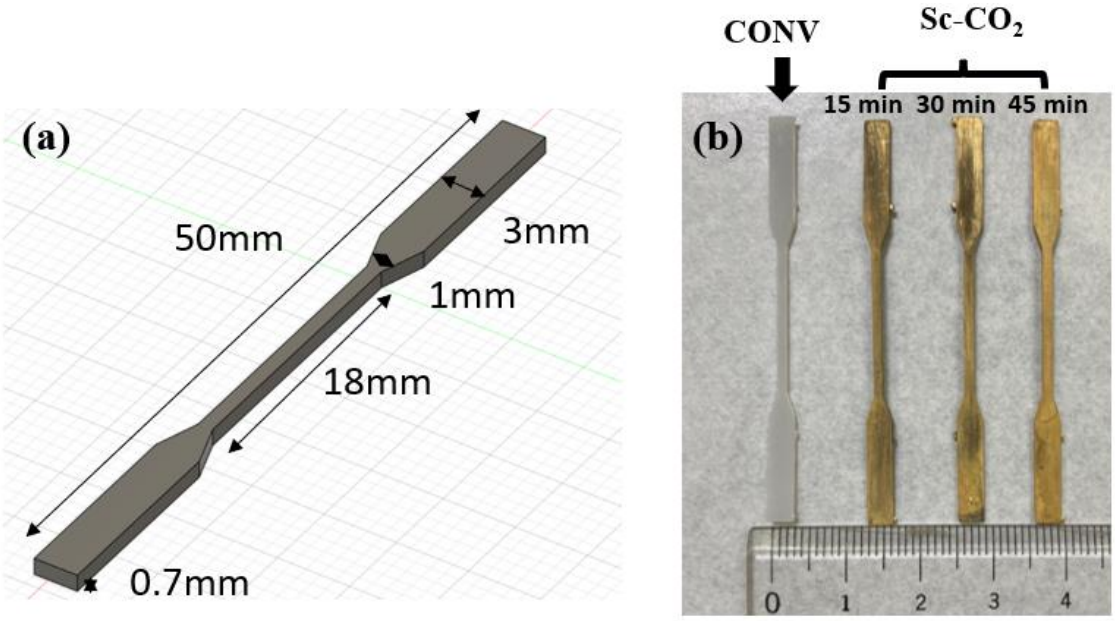


**Figure 5-1**. (a) A schematic design of the 3D printed dog-bone structure and (b) images of the 3D printed dog-bone structures after the gold deposition step.

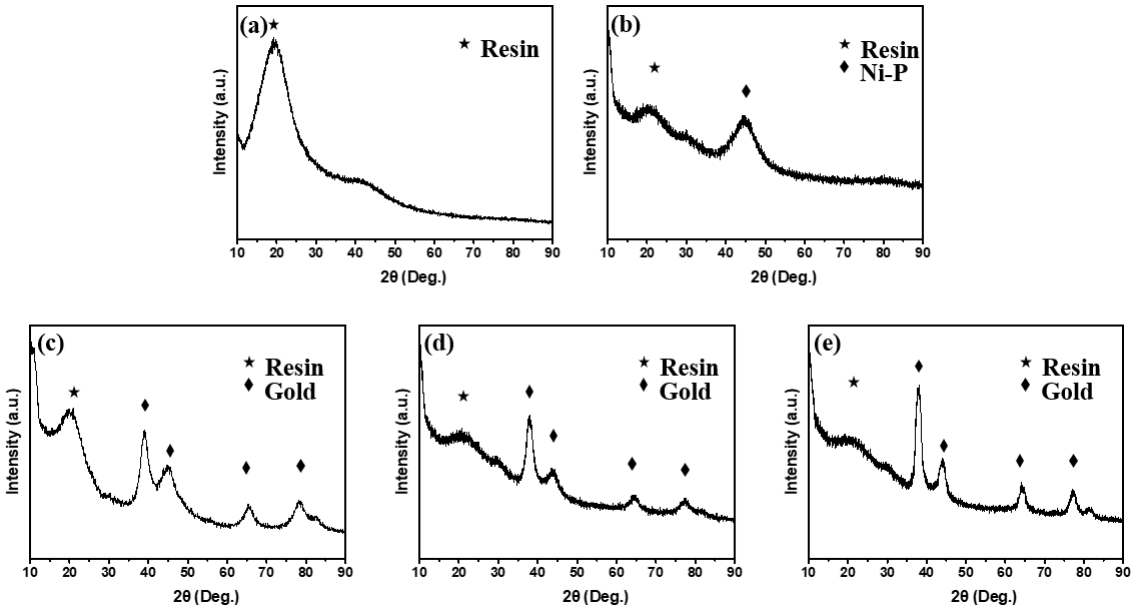


**Figure 5-2**. XRD of (a) 3D printed polymer structure, (b) Ni-P decorated and sc-$CO_2$ catalyzed sample, and gold metallized 3D printed polymer structure with (c) 15.0 min, (d) 30.0 min and (e) 45.0 min of the gold deposition time.

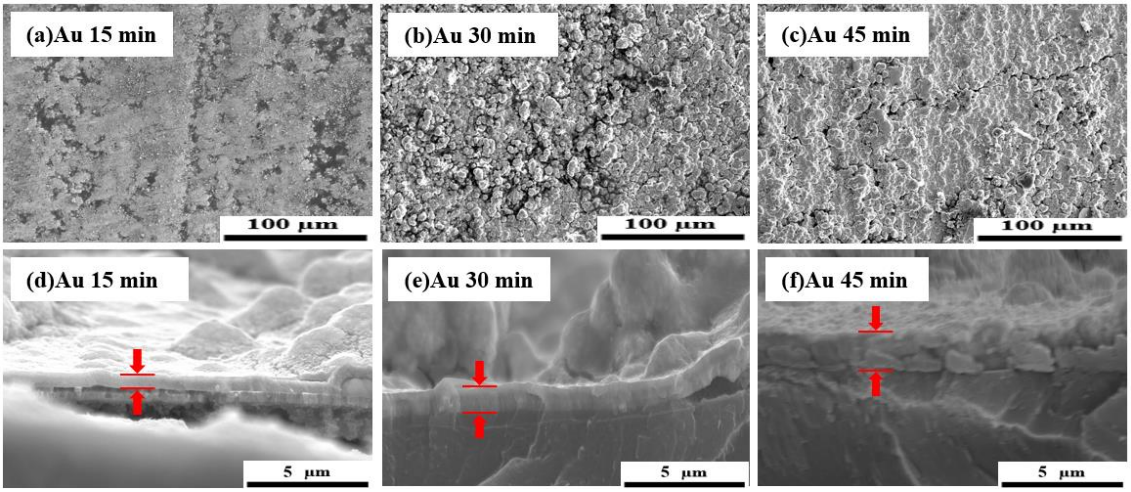


**Figure 5-3**. Surface conditions of the gold metallized 3D printed polymer structures prepared with (a) 15.0 min, (b) 30.0 min and (c) 45.0 min of the gold deposition time, and cross-sectional view of the samples with (d) 15.0 min , (e) 30.0 min, and (f) 45.0 min of the gold deposition.

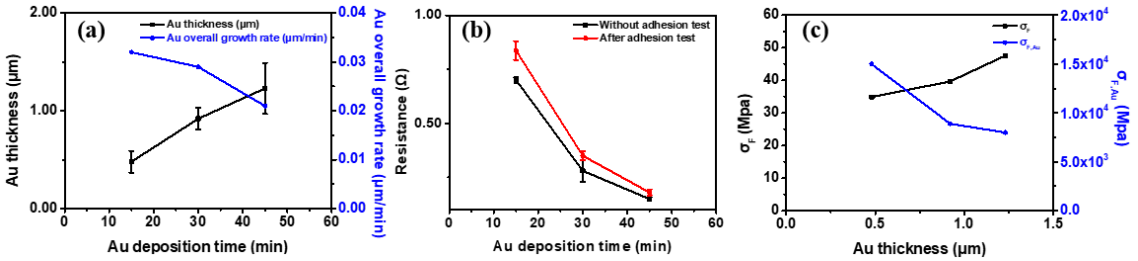


**Figure 5-4**. Plots of (a) the gold deposition time versus the gold layer thickness and gold growth rate, (b) the gold deposition time versus the electrical resistance, and the (c) gold layer thickness versus and the two fracture strengths ($\sigma_F$ and $\sigma_{F,Au}$).

CHAPTER 6

# *Selective pattern achieved by sc-$CO_2$ assisted metallization of microstructure on 3D-printed polymer*

## 6.1 Introduction

Selective patterning is a popular issue in the electroless plating field due to the requirement for integrated circuits. Additional treatments are introduced in the catalyzation step to ensure that the metal is deposited only in the required area. Published methods such as photolithography, which involves using photoresist polymers [6-1], or utilizing a laser to induce the required pattern for metallization [6-2], are effective in achieving selective patterning. However, they are relatively complex. In this chapter, the simple structures fabricated using 3D printing technology were utilized to achieve selective patterning based on differences in surface roughness.

## 6.2 Experimental

### *6.2.1 3D printing*

The 3D printer (Saturn 2 MONO LCD MSLA resin 3D printer) and photopolymer resin (Standard LCD UV-Curing Photopolymer Rapid Resin for 3D

Printers) were purchased from Elegoo Inc. The resin was composed of phenolic epoxy resin (40-50 wt%), 6-hexanediol diacrylate (20-40 wt%), color pigment (2-5%), and 1-hydroxycyclohexyl phenyl ketone (3-5 wt%). UV light at $\lambda$ = 405 nm was used as the light source in photopolymerization of the resin. A schematic diagram of the rectangle, pillar, and cone-shaped structure with different space interval (0.3, 0.15, 0.075mm) is provided in Fig. 6-1(a).

*6.2.2 Catalyzation*

To compare with the sc-$CO_2$ catalyzation, a commercial catalyzation solution (ICP Accera KCR by Okuno Chemical Industries Co., Ltd.) was used to catalyze the 3D-printed polymer structures. The conventional catalyzation was conducted at 30°C for 30 minutes.

For the sc-$CO_2$ catalyzation, a sc-$CO_2$ equipment provided by Japan Spectra Company was used. The reaction cell was made of stainless steel 316 with a polyether ether ketone coating on the inner wall, and its inner volume was 50.0 ml. A 3D-printed polymer structure and 50 mg of palladium bis-hexafluoroacetylacetonate ($Pd(hfa)_2$, Sigma-Aldrich) were placed in the reaction cell. After sealing the cell properly, liquid $CO_2$ was pumped into the reaction, and the pressure was controlled at 15 MPa while the temperature was set at 70 °C for 1.0 hour.

*7.2.3 Metal deposition*

Following the catalyzation step, the 3D-printed polymer structures were immersed in a Ni-P electroless plating solution (Top Nicoron VS-LF by Okuno Chemical Industries Co., Ltd.) at 90.0°C for 4.0, 6.0, 8.0 minutes. The Ni-P plating solution

consisted of nickel chloride (9 wt%), sodium hypophosphite (12 wt%), complexing agent (12 wt%), and ion-exchanged water (67 wt%). In this study, Ni-P was chosen as the sacrificial material for electroless plating of gold [6-3], where less noble metals are required to be decorated on the catalyzed substrate before deposition of gold.

After the Ni-P decoration, a sensitization step was conducted by immersing the structures in a 0.1 mM $KAuCl_4$ solution (99.995%, Sigma-Aldrich) at 30.0°C for 30 min. Subsequently, the $KAuCl_4$ sensitized/Ni-P/3D-printed polymer structures were immersed in a commercially available gold electroless plating solution (Non-Cyanide Electroless Solution by MATEX Japan Co., Ltd.), which contained 2 g/L of Au and had a pH of 7, for 1 hour at 65°C to ensure complete surface coverage of the pattern with gold.

*6.2.4 Characterization*

The surface morphologies and cross-section of the 3D-printed polymer structures with gold were observed by an optical microscope (OM, KEYENCE: VHV-5000) and a scanning electron microscope (SEM, HITACHI: S-4300SE). The thickness of the Ni-P layer was determined through observing the cross-section, and the thickness of at least five locations was obtained and averaged to be used as the reported thickness. Crystal structures and phase of the Ni-P metallized 3D-printed polymer structures were identified by X-ray diffraction (XRD, Rigaku: Ultima IV). The electrical resistance was examined by a Digital multimeter (SANWA SUPPLY INC.: PC-710). By exploiting differences in adhesion, unwanted portions were removed using tape to achieve a patterned effect. The tape was conducted by firmly sticking a piece of 3M Scotch® tape onto the Ni-P metallized sample surface.

## 6.3 Result and discussion

### *6.3.1 Conventional and sc-$CO_2$ Catalyzation*

Overviews of various 3D-printed patterns catalyzed by the conventional method and the sc-$CO_2$ catalyzation followed by Ni-P metallization at 90 °C are shown in Fig. 6-2(a) and Fig. 6-2(b), respectively. The original color of the photopolymer resin is grey. The 3D-printed patterns treated by conventional catalyzation remained original color of photopolymer after Ni-P metallization step, which indicated that the unsuccessful catalyzation was conducted. On the contrary, Ni-P metallization of the 3D-printed pattern treated by sc-$CO_2$ catalyzation was successfully performed, which showed the metal bright-like surface with clear pattern in Fig. 6-2(b). As a result, the conventional catalyzation was ineffective in the decoration of Pd catalyst seeds on the 3D-printed pattern. The metallization certainly could not be achieved for the conventional catalyzation treated sample.

### *6.3.2 Morphology of 3D-printed pattern*

The surface morphology of rectangle, pillar and cone with space interval of 0.3, 0.15, 0.075 mm were observed by OM in Fig. 6-3(a) to (i). In addition, the surface roughness of each pattern was measured. The surface roughness of rectangle pattern with space interval of 0.3 was 14. 23 μm. Upon reducing the pace interval to 0.15 mm, the roughness increased to 15.56 μm. When the space interval was further decreased to 0.075 mm, the roughness reduced to 12.63 μm. This reduction in roughness is likely due to overlapping that occurred during the printing process, which caused the leakage of radicals generated from the UV-exposed resin. Delicate 3D-printed designs are more susceptible to this issue, as the radicals can easily accumulate on the undesired structures

that were not UV-exposed. On the other hand, the pillar pattern showed a different trend compared to the rectangle pattern. When the space interval was 0.3 μm, the roughness of the pillar was 18.21 μm, and as the space interval decreased, the roughness increased. Even in Fig. 6-3(f), where a slight overlap appears to have occurred again, the roughness was still higher. The cone pattern showed a similar trend to the rectangle pattern, with roughness increasing from 5.29 μm to 13.46 μm as the space interval decreased. However, when the space interval was decreased to 0.075 mm, the roughness of the cone pattern decreased as well. This is likely due to the printing resolution being sufficient for the peak of the cone, and the height of the cone not being achieved as expected.

*6.3.3 Metallization of 3D-printed pattern*

Appearance of the 3D-printed pattern samples after Ni-P metallization for 4,6,8 min was shown in Fig. 6-4(a) to (c). The surface of 3D-printed pattern was fully covered by Ni-P metal layer. However, with prolonged deposition time, the surface of Ni-P appeared to have some crack which was suspected that be caused by the high internal stress of Ni-P [6-4]. In Fig. 6-4(d) to (f) were the Ni-P metalized 3D-ptinted pattern after being peeled off with tape. The metal layers on the smooth surface and low roughness part of pattern were removed by the tape. From the result of tape peeled-off metalized 3D-printed pattern, despite the metal deposition time extended, the pattern of pillar with 0.075 space interval remained more metal than other patterns. The result corresponded well to roughness results observed from the OM. The higher roughness surface provided more contact area for Ni-P metal to attach, despite the high internal stress of Ni-P usually caused weak adhesion.

The Ni-P layer deposited in this study was expected to be amorphous. Fig. 6-5

shows that the XRD signals at around 2θ = 20° were contributed by the 3D-printed polymer, while the signals at around 2θ = 45° were caused by the amorphous Ni-P. Intensities of the Ni-P signals increased and the polymer signals decreased along with an increase in the metal deposition time, which suggested an increase in amount of Ni-P deposited on the surface.

Fig. 6-6(a) summarizes the thickness of the Ni-P layer for different deposition times. The thickness of the Ni-P layer was 1.58 μm when a deposition time of 2 min was used for the 3D-printed pattern catalyzed in sc-$CO_2$. When the deposition time was increased to 6 and 8 min, the thickness of the Ni-P layer increased to 2.2 and 2.81 μm, respectively. This trend in thickness increase with longer deposition times corresponded well to the results observed from the XRD (Fig. 6-5), where the XRD responses from the substrate gradually decreased, and the peak intensities contributed by the Ni-P gradually increased as the deposition time prolonged.

The electrical resistance of the 4.0 min sample was initially measured to be 16.61 Ω. However, as the Ni-P deposition time was extended to 6.0 min and 8.0 min, the electrical resistance reduced to 7.32 Ω and 3.77 Ω, respectively, indicating an improvement in electrical conductivity. After the tape peeled-off process, the electrical resistances of the 4.0 min, 6.0 min, and 8.0 min samples increased to 23.8 Ω, 13.65 Ω, and 7.95 Ω, respectively, as shown in Fig. 6-6(b).

### *6.3.4 Au/Ni-P/3D-printed pattern*

To achieve selective metallization in electroless plating, a combination of a highly rough 3D-printed pattern and a metal with relatively weak adhesion is essential. If the adhesion between the metal and 3D-printed pattern is too strong, selective

metallization cannot be achieved. Thus, the ideal combination of design for the 3D-printed pattern and Ni-P deposition time was determined based on the results from Fig. 6-3 and Fig. 6-4. The pillar with a 0.075 μm space interval and a 6 min Ni-P deposition time were selected to achieve a selective metalized pattern. The surface morphology observed from SEM in Fig. 6-7(f) showed that the pillar with a 0.075 μm space interval and 6 min metalization time retained the most Ni-P after being peeled off with tape. This result reveals the possibility of achieving a selective metallization using electroless plating.

A circuit-like 3D-printed pattern was designed, as shown in Fig. 6-8(a). The pattern was treated with sc-CO catalyzation and then subjected to Ni-P metallization for 6 min, as shown in Fig. 6-8(b). The resulting metalized circuit-like 3D-printed pattern was achieved, and the electrical resistance was measured from point A to point B as labeled in Fig. 6-8(c). The electrical resistance was found to be 170 Ω, which was too high for practical use. Therefore, Au was deposited for 1 hour to improve the electrical resistance from 170 Ω to 1.7 Ω, as shown in Fig. 6-8 (d).

## 6.4 Chapter summary

This study demonstrated the use of additive manufacturing for gold metallized circuit production, achieved through sc-$CO_2$ assisted electroless plating. By utilizing sc-$CO_2$ as a solvent, the Pd catalyst was able to effectively interact with the surfaces of the 3D printed structures during the catalyzation step, leading to complete gold metallization. The roughness of the 3D-printed patterns was found to play a critical role, as the internal stress of Ni-P was leveraged to enhance the importance of roughness in adhesion. As a result, a selective pattern of gold metallization was achieved in a convenient and efficient

process.

## 6.5 References


[6-1] Garcia, J.P. Maris, P. Viel, S. Palacin, T. Berthelot, Localized Ligand Induced Electroless Plating (LIEP) Process for the Fabrication of Copper Patterns Onto Flexible Polymer Substrates. Adv. Funct. Mater. 21 (2011) 2096–2102. https://doi.org/10.1002/adfm.201100041

[6-2] H. Xu, J. Feng, F. Yu, J. Huang, T. Zhou, Laser-Induced Selective Metallization on Polymers for Both NIR and UV Lasers: Preparing 2D and 3D Circuits. Ind. Eng. Chem. Res. 62 (2023) 395–404. https://doi.org/10.1021/acs.iecr.2c03367

[6-3] P.W. Cheng, C.Y. Chen, T. Ichibayashi, T.F.M. Chang, M. Sone, S. Nishimura, Supercritical carbon dioxide-assisted functionalization of polyethylene terephthalate (PET) toward flexible catalytic electrodes. J. Supercrit. Fluids 180 (2022) 105455. https://doi.org/10.1016/J.SUPFLU.2021.105455

[6-4] J. Sudagar, J. Lian, W. Sha, Electroless nickel, alloy, composite and nano coatings – A critical review. J. Alloys Compd. 571 (2013) 183-204. https://doi.org/10.1016/j.jallcom.2013.03.107

## 6.6 Figures

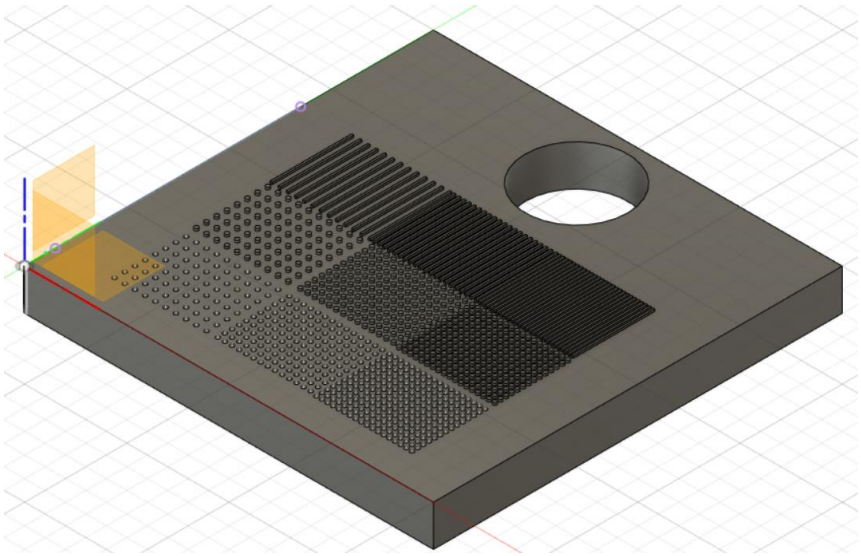

**Figure 6-1.** A schematic design of the 3D-printed patterns.

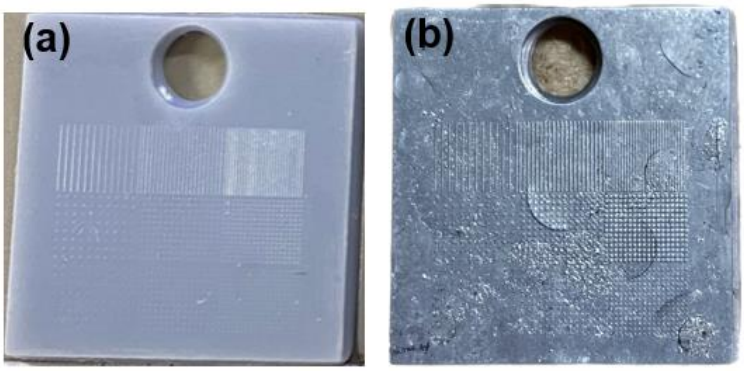


**Figure 6-2.** Metalized 3D-printed patterns catalyzed in (a) conventional solution and (b) sc-$CO_2$.

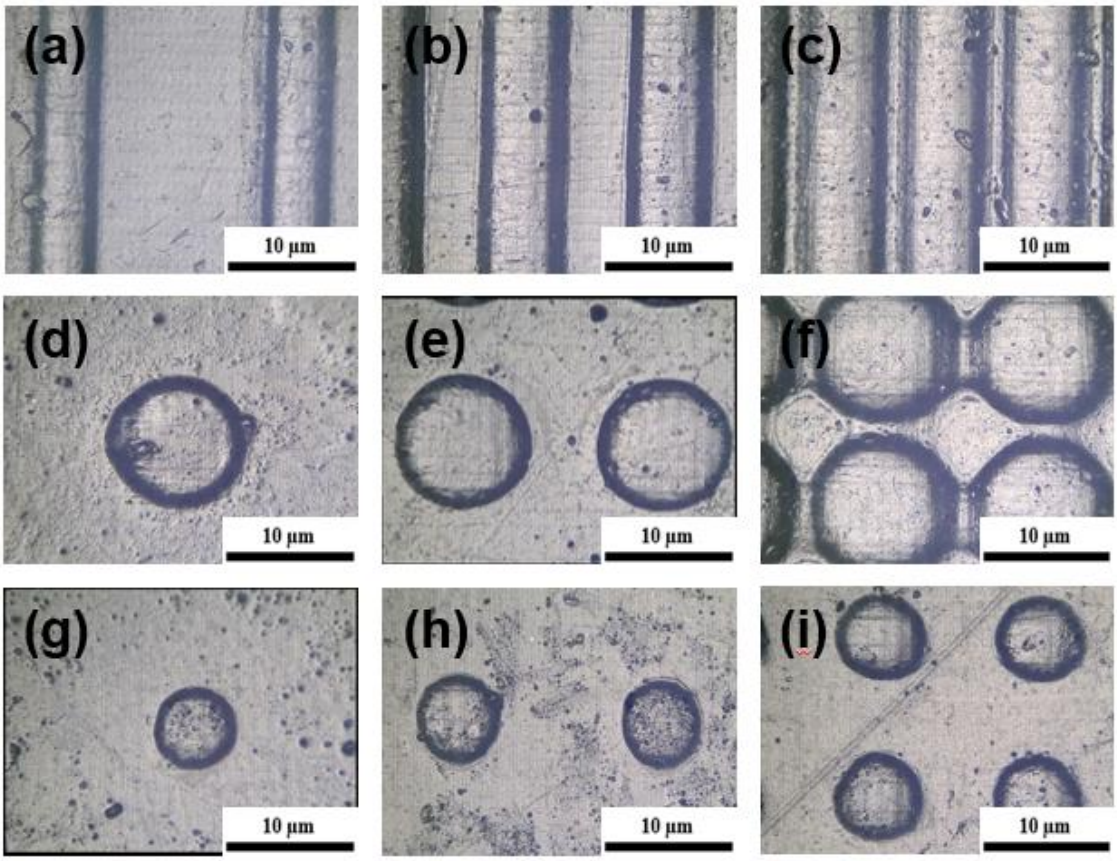


**Figure 6-3.** OM images of top views 3D-printed rectangle with (a) 0.3, (b) 0.15 and (c) 0.075 µm space interval, pillar with (d) 0.3, (e) 0.15 and (f) 0.075 µm space interval, and cone with (g) 0.3, (h) 0.15 and (i) 0.075 µm space interval.

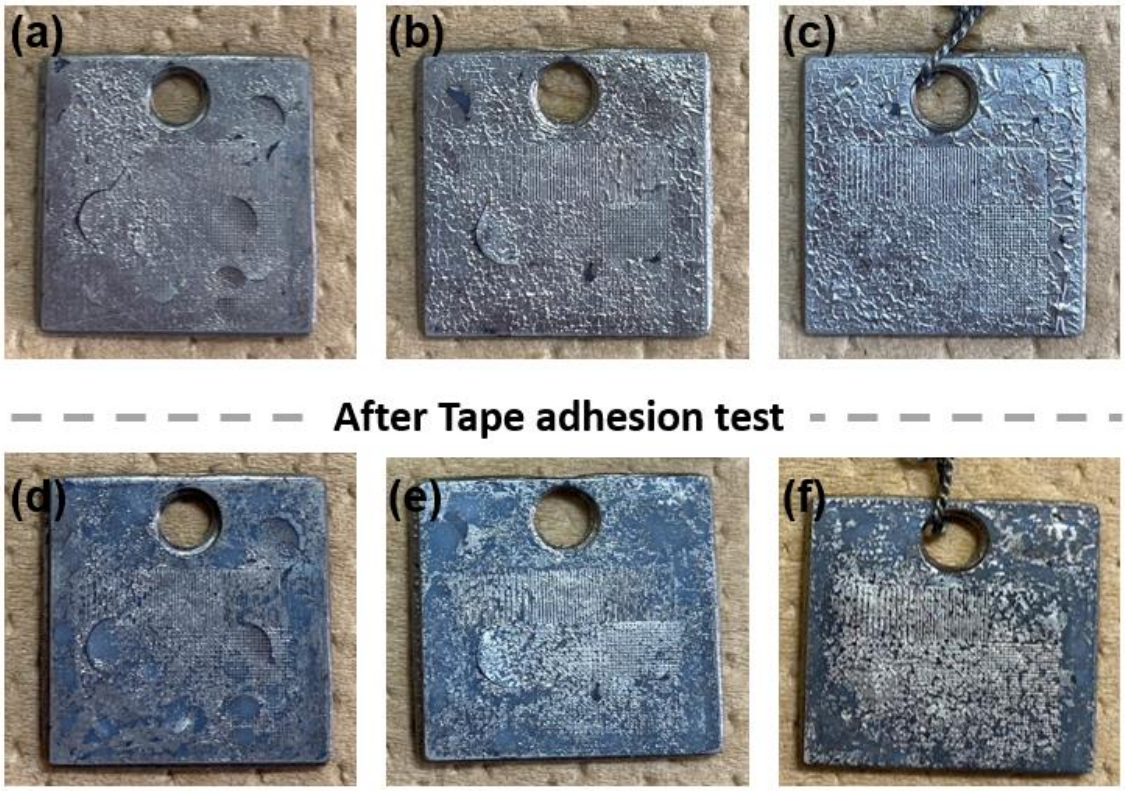


**Figure 6-4.** Images of Ni-P metallized 3D-printed pattern for (a) 4, (b) 6, and (c) 8 min of the metal deposition time, and after tape peeled off (d) 4, (e) 6, and (f) 8 min of the metal deposition time.

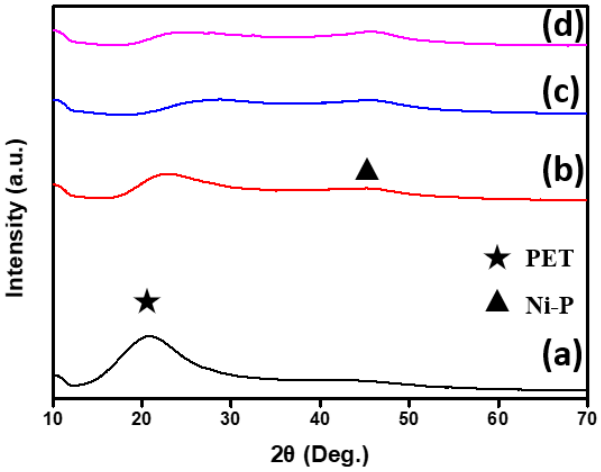


**Figure 6-5.** XRD patterns of the (a) 3D-printed pattern and the Ni-P/3D-printed pattern prepared with (b) 4 min, (c) 6 min and (d) 8 min of the Ni-P deposition time.

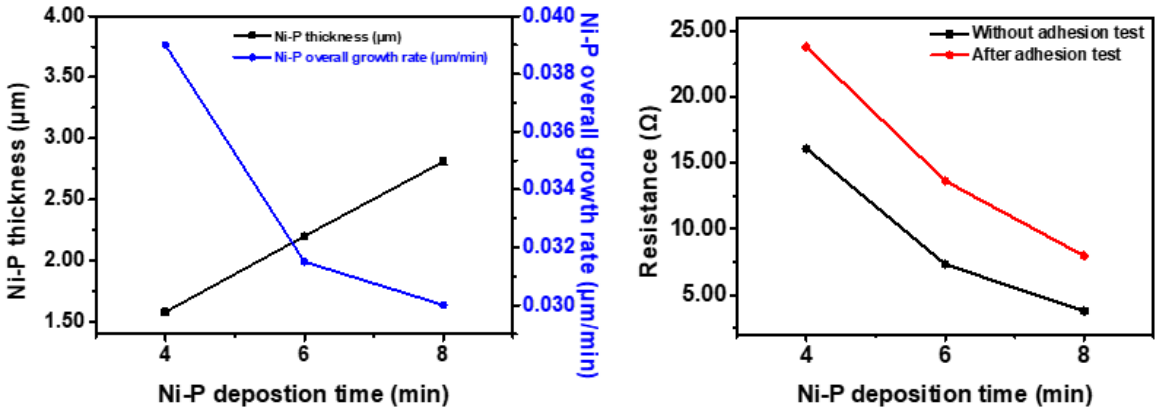


**Figure 6-6.** Plots of (a) the Ni-P deposition time versus the Ni-P layer thickness and Ni-P growth rate, (b) the Ni-P deposition time versus the electrical resistance.

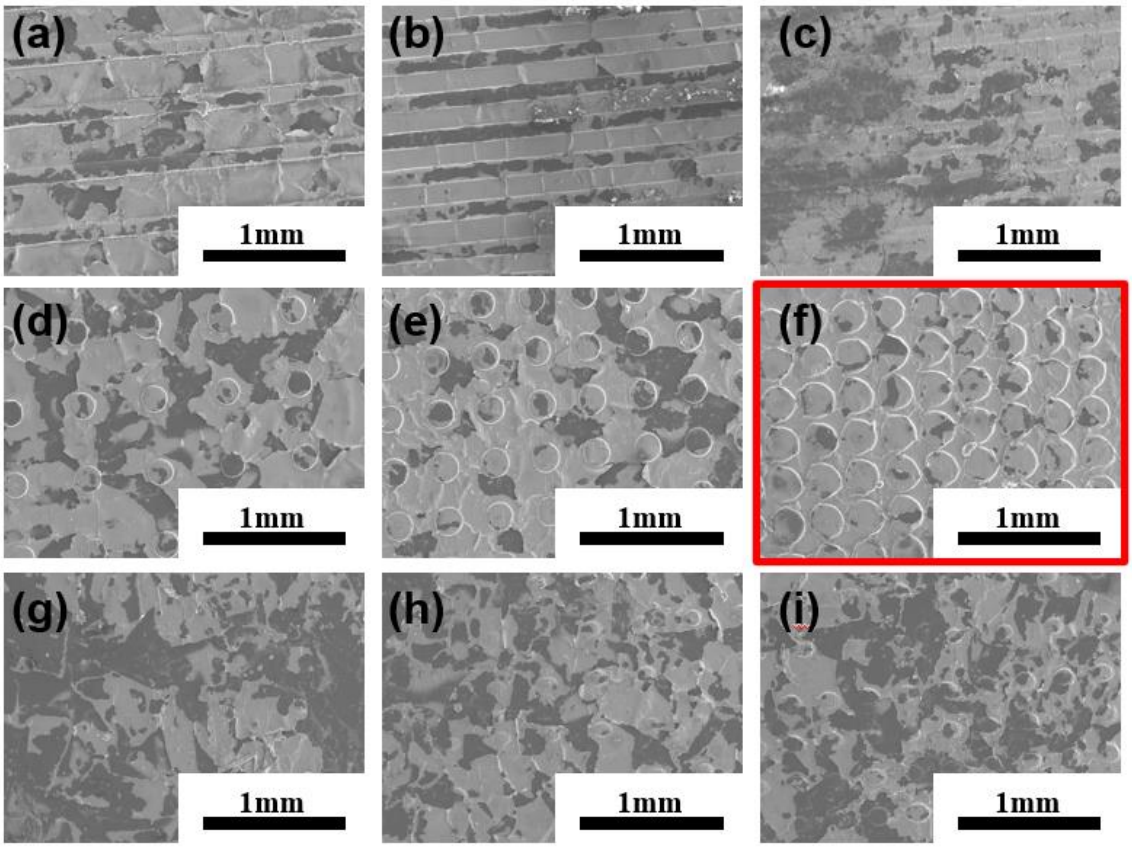


**Figure 6-7.** SEM images of top views of the Ni-P/3D-printed rectangle with (a) 0.3, (b) 0.15 and (c) 0.075 μm space interval, pillar with (d) 0.3, (e) 0.15 and (f) 0.075 μm space interval, and cone with (g) 0.3, (h) 0.15 and (i) 0.075 μm space interval.

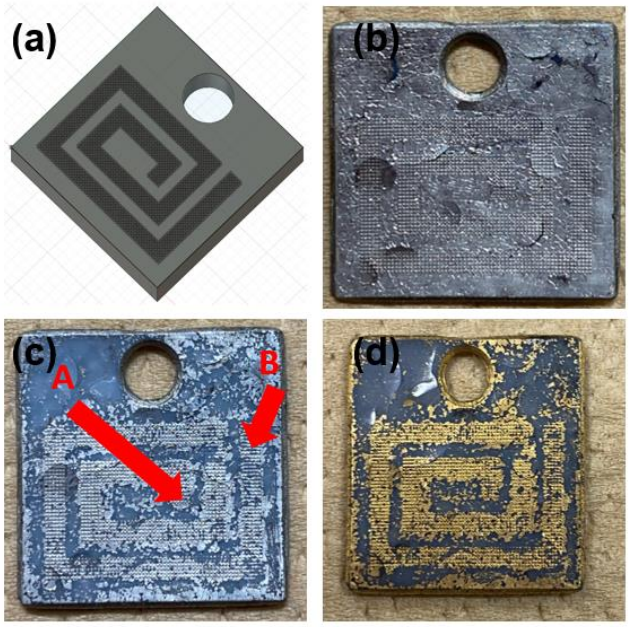


**Figure 6-8.** (a) A schematic design of the 3D-printed circuit. Images of the (b) Ni-P/3D-printed composition, (c) following tape peeled off, and (d) Au/Ni-P/3D-printed composition.

CHAPTER 7

# *Effects of sc-$CO_2$ Catalyzation in Metallization of 3D Complex Polymer Structure*

## 7.1 Introduction

Throughout the thesis, I have extensively examined a metallization methodology for various polymeric structures using supercritical carbon dioxide (sc-$CO_2$) and successfully demonstrated its effectiveness. However, a significant issue remains regarding the variability of sc-$CO_2$ effects on polymer metallization, which strongly depends on the type of polymer. In the conducted studies [7-1, 7-2, 7-3], we employed sc-$CO_2$ as a solvent for catalysis and utilized sc-$CO_2$ solutions containing organometallic compounds such as $Pd(acac)_2$ or $Pd(hfa)_2$ as catalytic media.

In this chapter, I aim to elucidate the effect of sc-$CO_2$ on a metallization methodology of several polymeric structures. This investigation involves an in-depth analysis of the fundamental properties of sc-$CO_2$, which possesses intermediate characteristics between a gas and a liquid. In its supercritical state, $CO_2$ exhibits unique properties that make it a versatile solvent for various applications, including the modification and processing. The impact of sc-$CO_2$ on polymers can be highly diverse and relies on several factors, including the type of polymer, molecular weight,

temperature, pressure, and the specific application at hand [7-4]. To discuss the effect of sc-$CO_2$ on a metallization methodology of polymeric materials, I discussed the effect of solvent and gas effect on polymer processing as compared with that of sc-$CO_2$.

### 7.1.1 *Effects of solvent on polymeric materials*

As mentioned above, sc-$CO_2$ possesses intermediate characteristics between a gas and a liquid. Solvents can play a significant role on the crystallization of polymers. The choice of solvent and its properties can influence the rate of crystallization, the crystal structure, and the overall quality of the resulting crystals. Here are some key effects that solvents can have on the crystallization of polymers [7-5–7-7].

(1) Solubility into polymeric materials

Solvents can affect the solubility of polymer chains, which in turn affects the crystallization process. If a solvent has high solubility for a polymer, it can hinder or prevent the formation of crystalline structures. On the other hand, a solvent with low solubility for a polymer can promote crystallization by facilitating the aggregation of polymer chains.

(2) Nucleation

Solvents can influence the nucleation stage of crystallization. Certain solvents may act as nucleating agents, promoting the formation of nuclei and enhancing the rate of crystal growth. Nucleating agents provide sites for the polymer chains to align and initiate crystal formation. The solvent's properties, such as its polarity and viscosity, can affect the formation and stability of nuclei.

(3) Chain Mobility

Solvents can affect the mobility of polymer chains, which plays a crucial role in the crystallization process. A solvent that interacts strongly with the polymer chains can reduce their mobility, impeding the formation of crystalline structures. Conversely, a solvent with low interaction or weak solvation with the polymer can enhance chain mobility and facilitate the formation of well-defined crystals.

(4) Cooling Rate

Solvents can influence the cooling rate during crystallization. Different solvents have varying heat capacities and thermal conductivities, affecting the rate at which the polymer solution or melt cools. The cooling rate can influence the nucleation and crystal growth stages. Rapid cooling can lead to a higher rate of nucleation and smaller crystal size, while slower cooling may favor larger crystals.

(5) Solvent Evaporation

In some cases, solvent evaporation plays a role in the crystallization process. If a polymer is dissolved in a solvent and the solvent is allowed to evaporate, the gradual removal of the solvent can induce the polymer chains to aggregate and crystallize. Solvent evaporation can result in the formation of thin films, fibers, or other morphologies that exhibit enhanced crystallinity.

### 7.1.2 *Effects of gas on polymeric materials*

The effects of gases on polymeric materials can vary depending on the type of gas, the specific polymer, and the environmental conditions. Here are some general effects that gases can have on polymeric materials [7-8–7-10]:

(1) Permeation

Gases can permeate through polymers, meaning they can diffuse into and through

the material. This can lead to changes in the properties of the polymer, such as dimensional changes, mass loss or gain, and altered mechanical or electrical properties. For example, the permeation of oxygen or moisture into certain polymers can degrade their mechanical strength or cause oxidation reactions.

(2) Swelling

Some gases can cause swelling of polymers, leading to an increase in volume or dimensional changes. The swelling effect occurs when the gas molecules penetrate the polymer structure, breaking the intermolecular forces and causing expansion. This can affect the mechanical integrity of the polymer and lead to changes in its physical properties.

(3) Plasticization

Certain gases can act as plasticizers for polymers, similar to the effect of supercritical $CO_2$. They can reduce the glass transition temperature (Tg) of the polymer, making it more flexible and easier to process. This can lead to increased ductility, improved moldability, and changes in the polymer's mechanical properties.

### *7.1.3 Effects of sc-$CO_2$ on polymeric materials*

The effect of solvent leads to crystallization while the gas effect to plasticization. Supercritical fluids possess intermediate characteristics between a gas and a liquid, then have the opposite effects between gas and liquid. As widely accepted, there are four effects of sc-$CO_2$ on polymeric materials including (1) polymer swelling and solubility, (2) plasticization, (3) enhanced mass transfer and (4) supercritical foaming as summarized below [7-11–7-14].

(1) Polymer swelling and solubility

Sc-$CO_2$ can cause the swelling or dissolution of certain polymers. It can penetrate the polymer matrix, disrupting the intermolecular forces and increasing the free volume within the polymer. This can lead to increased polymer chain mobility, changes in polymer morphology, and altered physical properties.

(2) Plasticization

Sc-$CO_2$ can act as a plasticizer for polymers. It can reduce the glass transition temperature (Tg) of the polymer, making it more flexible and easier to process. This plasticizing effect can be beneficial for improving polymer processing techniques such as extrusion, injection molding, or coating.

(3) Enhanced mass transfer

Sc-$CO_2$ has excellent mass transfer properties due to its low viscosity and high diffusivity. It can efficiently penetrate and permeate polymers, facilitating the extraction of impurities, residual monomers, or additives. This makes sc-$CO_2$ a potential environmentally friendly alternative to traditional organic solvents in extraction processes.

(4) Supercritical foaming

When a polymer is saturated with sc-$CO_2$ and rapidly depressurized, the dissolved $CO_2$ can expand and form gas bubbles, leading to the creation of a foam structure within the polymer. This process is known as supercritical foaming and is used to generate polymer foams with controlled cellular structures and improved mechanical properties.

Therefore, this chapter aims to analyze the effect of sc-$CO_2$ treatment on polymer substrates using X-ray diffraction (XRD) patterns to determine changes in crystallinity.

## 7.2 Experimental

### *7.2.1 Materials*

PET films provided by Toray Industries, Inc. were cut into small pieces measuring 2.0 cm x 2.0 cm and used as substrates. $CO_2$ used in the sc-$CO_2$ catalyzation step was provided by Nippon Tansan Gas Co., Ltd. and had a purity of 99.99%. Palladium bis-hexafluoroacetylacetonate ($Pd(hfa)_2$) (<=100%), Palladium(II) acetylacetonate ($Pd(acac)_2$) and ε-caprolactam (99%) were purchased from Sigma-Aldrich.

### *7.2.2 sc-$CO_2$ Catalyzation*

For the sc-$CO_2$ catalyzation step, a high-pressure apparatus (Japan Spectra Company, Japan) was utilized. The reaction cell was made of stainless steel 316 with polyether ether ketone coating on the inner wall, and the inner volume was 50.0 ml. A piece of the PET film and 50.0 mg of $Pd(hfa)_2$, 50.0 mg of $Pd(acac)_2$ and 50.0 mg of $Pd(acac)_2$ with 30.0 mg of ε-caprolactam were separately placed in the reaction cell before pressurizing $CO_2$ into the reaction cell. The each catalyzation was conducted at 15.0 MPa and 70.0 °C for 1.0 hr. 50.0 mg of $Pd(hfa)_2$ in the reaction cell implied the concentration in sc-$CO_2$ was 0.4 wt%.

### *7.2.3 Characterization*

Crystallinity of the PET treated by sc-$CO_2$, PET treated by sc-$CO_2$ with $Pd(hfa)_2$, PET treated by sc-$CO_2$ with $Pd(acac)_2$, and PET treated by sc-$CO_2$ with $Pd(acac)_2$ + ε-caprolactam, as well as each sample metallized by Ni-P also were identified by X-ray diffraction (XRD, Ultima IV, Rigaku). The XRD patterns were deconvoluted using OriginPro 9.0 software (OriginLab Corporation). A curve-fitting process involving

Gaussian functions was applied to the diffractograms to extract individual crystalline and amorphous peaks. It was assumed that the sharp peaks represented crystalline domains, while the broad peaks represented the amorphous contribution. The crystallinity was measured by the following equation [7-15]:

$$\text{Crystallinity (\%)} = \frac{Sc}{St} \times 100$$

Sc and St represent the area of the crystalline domain and the area of the complete domain (crystalline + amorphous), respectively.

## 7.3 Results and Discussion

### *7.3.1. Morphology changes of PET by* sc-$CO_2$ *treatments*

Figure 7-1 shows the photo images of PET and PET treated by sc-$CO_2$ with different catalysts. In the Fig. 7-1(a) to (c) represent PET film before and after sc-$CO_2$ treatment, and with $Pd(hfa)_2$, respectively, and no noticeable difference was observed between the untreated PET. However, The PET film treated by sc-$CO_2$ with $Pd(acac)_2$ in Fig. 7-1(d) and $Pd(acac)_2$ + ε in Fig. 7-1(e) exhibited a light-yellow appearance, which is due to their relatively low solubility in sc-$CO_2$ compared with $Pd(hfa)_2$. Other than the color change attributed to the catalyst type, no significant appearance changes were observed after sc-$CO_2$ treatment.

### *7.3.2 Crystallinity changes of PET by* sc-$CO_2$ *treatments*

PET is a semicrystalline material comprising crystalline and amorphous reigns [7-16], where is recognized that mass transfer of sc-$CO_2$ mainly occurs into the amorphous phase. The amorphous region is more favorable for the diffusion of substances than the crystalline region. This is because in the amorphous region of PET, the molecular

arrangement is more loosely packed, resulting in more pores and voids that facilitate the diffusion and transport of substances into the interior of PET. In contrast, the molecular arrangement in the crystalline region of PET is more densely packed, resulting in lower porosity and slower diffusion rates of substances [7-16].

Fig. 7-2 (a) and Fig. 7-2 (b) show the XRD patterns of the PET film and PET film treated by sc-$CO_2$ for 1hr, respectively. The crystallinity of untreated PET was 64.9 %, while the crystallinity of sc-$CO_2$ treated was 63.56 %. The crystallinity of PET decreased after the sc-$CO_2$ treatment and this decrease can be due to the effect of absorption of $CO_2$ molecules into polymer structure [7-10]. When the PET was arranged in $CO_2$ environments, the glass transition temperature also can be reduced and lead to the increase of amorphous regions, as illustrated in Fig. 7-3. This behavior can be explained as the gaseous properties of sc-$CO_2$ and the density of sc-$CO_2$ is close to density of the gas state (about 1.0 x $10^{-3}$ g/$ml^3$).

XRD patterns of the PET film treated by sc-$CO_2$ with $Pd(hfa)_2$, $Pd(acac)_2$, and $Pd(acac)_2$+ ε-caprolactam were shown in Fig 7-4 (a), (b) and (c), respectively. The crystallinity of PET after sc-$CO_2$ treatment with $Pd(hfa)_2$ was enhanced to 64.14 %. Thus the solvent effect of sc-$CO_2$ solution with $Pd(hfa)_2$. This is because the dissolution of $Pd(hfa)_2$ in sc-$CO_2$ led to an increase in density of sc-$CO_2$, resulting in exhibiting more liquid-like properties. Moreover, PET is known to crystallize when it comes into contact with solvents [7-10]. Therefore, the observed increase in crystallinity aligns with expectations illustrated in Fig. 7-5.

The crystallinity of PET after sc-$CO_2$ treatment with $Pd(acac)_2$ was merely enhanced to 63.73 % which revealed that sc-$CO_2$ solution with $Pd(acac)_2$ is closed to gaseous state of $CO_2$ as discussed about sc-$CO_2$ treatment. Also $Pd(acac)_2$ has about 1/100

times lower solubility than $Pd(hfa)_2$ into sc-$CO_2$ solvent and thus the light-yellow colored $Pd(acac)_2$ deposits on PET after sc-$CO_2$ treatment as shown in Fig. 7-1. The sc-$CO_2$ solution of $Pd(acac)_2$ can have gaseous property.

The solubility of $Pd(acac)_2$ is lower than $Pd(hfa)_2$ in sc-$CO_2$ and the dissolution of $Pd(hfa)_2$ in sc-$CO_2$ led to a less increase in density of sc-$CO_2$. Also, the interaction between PET and $Pd(acac)_2$ was not compatible, making it difficult for $Pd(acac)_2$ to remain on the PET. Therefore, the addition of ε-caprolactam, which is rich in $NH^-$ functional groups to enhance interaction with the PET substrate, is necessary when choosing $Pd(acac)_2$ as the catalyst. The crystallinity of PET after sc-$CO_2$ treatment with $Pd(acac)_2$+ε-caprolactam was increased to 66.96%. The polar solvent in PET induced an increase in crystallinity [7-17]. This results support the above models as shown in Fig. 7-3 and 7-5.

### *7.3.3 Effect of PET Crystallinity by* sc-$CO_2$ *treatments on metallization*

On these studies as mentioned above, the concentration of metal complex as $Pd(acac)_2$ and $Pd(hfa)_2$ into polymeric materials influenced metallization by electroless plating. Moreover, metallization on amorphous polymeric materials is difficult because of the difference in mechanical property between soft amorphous materials and hard metals electroplated. Thus, crystallinity of polymeric materials can strongly affect the metallization on polymer.

Pure sc-$CO_2$ treatments decreased the crystallinity of polymeric substrates. When we use the sc$CO_2$ solutions with $Pd(hfa)_2$ for sc$CO_2$ catalyzation, the crystallinity of polymer increases and metallization on polymeric materials becomes realized.

### 7.4 Chapter summary

The effect of sc-$CO_2$ treatment on the crystallinity of PET was investigated. The crystallinity of PET could be modified based on the properties of sc-$CO_2$. The density of sc-$CO_2$ close to gas tended to facilitate plasticization, resulting in an increase in the amorphous region. Conversely, the density of organometallic compounds dissolved in sc-$CO_2$, similar to liquid solvent, favored the induction of crystallization. The adjustment of PET crystallinity through sc-$CO_2$ treatment has important implications for its properties and applications. The presence of crystallinity in PET contributes to its metallization on the polymer. By controlling the density and properties of sc-$CO_2$, it becomes possible to tailor the crystallinity of PET to meet specific requirements.

## 7.5 References


[7-1] W.-T. Chiu, C.-Y. Chen, T.-F.M. Chang, T. Hashimoto, H. Kurosu and M. Sone, Ni–P and TiO2 codeposition on silk textile via supercritical CO2 promoted electroless plating for flexible and wearable photocatalytic devices. Electrochim. Acta 294 (2019) 68. https://doi.org/10.1016/j.electacta.2018.10.076

[7-2] K. Tokuoka, C.-Y. Chen, T.-F.M. Chang, W.-T. Chiu, H. Kurosu, M. Sone, Metallization of PET textile utilizing supercritical CO2 catalyzation. Microelectron Eng 223 (2020) 111233. https://doi.org/10.1016/j.mee.2020.111233

[7-3] M. Sano, Y. Tahara, C.-Y. Chen, T.-F. M. Chang, T. Hashimoto, H. Kurosu, T. Sato, M. Sone, Application of supercritical carbon dioxide in catalyzation and Ni-P electroless plating of nylon 6, 6 textile. Surf. Coat. Technol. 302 (2016) 336-343. https://doi.org/10.1016/j.surfcoat.2016.06.037

[7-4] Y.-T. Shieh, J.-H. Su, G. Manivannan, P. H. C. Lee, S. P. Sawan, W. D. Spall, Interaction of supercritical carbon dioxide with polymers. I. Crystalline polymers. J. Appl. Polym. Sci. 59 (1996) 695-705. https://doi.org/10.1002/(SICI)1097-4628(19960124)59:4<695::AID-APP15>3.0.CO;2-P

[7-5] Z. Shi, S. Zhang, J. Qiu, M. Li, H. Xing, T. Tang, Striking effect of carbon nanotubes on adjusting sc-CO2 foaming performance of PS/LLDPE blends and forming semi-open cellular structure. Polymer 207 (2020) 112896. https://doi.org/10.1016/j.polymer.2020.122896

[7-6] Ž. Knez, E. Markočič, Z. Novak, M. K. Hrnčič, Processing Polymeric Biomaterials using Supercritical CO2, Chem. Ing. Tech. 83 (2011) 1371-1380. https://doi.org/10.1002/cite.201100052

[7-7] I. Ahmad, A. Sabah, Z. Anwar, A. Arif, A. Arsalan, K. Qadeer, Effect of solvent polarity on the extraction of components of pharmaceutical plastic containers. Pak. J. Pharm. Sci. 30 (2017) 247-252.

[7-8] L. Ansaloni, B. Alcock, T. A. Peters, Effects of CO2 on polymeric materials in the CO2 transport chain: A review. Int. J. Greenh. Gas Control. INT J GREENH GAS CON. 94 (2020) 102930. https://doi.org/10.1016/j.ijggc.2019.102930

[7-9] B. D. Freeman, I. Pinnau, Polymeric Materials for Gas Separations. Polymer Membranes for Gas and Vapor Separation Chapter 1 pp 1-27. https://doi.org/10.1021/bk-1999-0733.ch001

[7-10] J. P. Jog, Crystallization of Polyethyleneterephthalate. J. macromol. sci., Polym. rev. 35:3 (1995) 531-553. https://doi.org/10.1080/15321799508014598

[7-11] M. Sauceau, J. Fages, A. Common, C. Nikitine, E. Rodier, New challenges in polymer foaming: A review of extrusion processes assisted by supercritical carbon dioxide. Prog. Polym. Sci. 36 (2011) 749-766. https://doi.org/10.1016/j.progpolymsci.2010.12.004

[7-12] V.P. Shantarovich, V. Bekeshev, N. Belov, I. Kevdina, M. Filimonov, I. Ronova, A. Nikolaev, On the Limits of Sensitivity of PALS to Incorporated Free Volume Holes in Polymeric Membranes and Sorbents: Effect of sc-CO2 in Polyhexafluoropropylene. Defect Diffus. Forum 373 (2017) 261-264. https://doi.org/10.4028/www.scientific.net/DDF.373.261

[7-13] Z. Shi, S. Zhang, J. Qiu, M. Li, H. Xing, T. Tang, Striking effect of carbon nanotubes on adjusting sc-$CO_2$ foaming performance of PS/LLDPE blends and forming semi-open cellular structure. Polymer 207 (2020) 112896. https://doi.org/10.1016/j.polymer.2020.122896

[7-14] Ž. Knez, E. Markočič, Z. Novak, M. K. Hrnčič, Processing Polymeric Biomaterials using Supercritical CO2, Chem. Ing. Tech. 83 (2011) 1371-1380. https://doi.org/10.1002/cite.201100052

[7-15] E.S. Wibowo, B.D. Park, Determination of Crystallinity of Thermosetting Urea-Formaldehyde Resins Using Deconvolution Method. Macromol. Res. 28 (2020) 615-624. https://doi.org/10.1007/s13233-020-8076-2

[7-16] J.V. Schnitzler, R. Eggers, Mass transfer in polymers in a supercritical $CO_2$-atmosphere, J. Supercrit. Fluids 16 (1999) 81–92. https://doi.org/10.1016/S0896-8446(99)00020-0

[7-17] W. Zhai, J. Yu, W. Ma, J. He, Cosolvent Effect of Water in Supercritical Carbon Dioxide Facilitating Induced Crystallization of Polycarbonate. Polym. Eng. Sci. 47 (2007) 1338- 1343. https://doi.org/10.1002/pen.20816

## 7.6 Figures

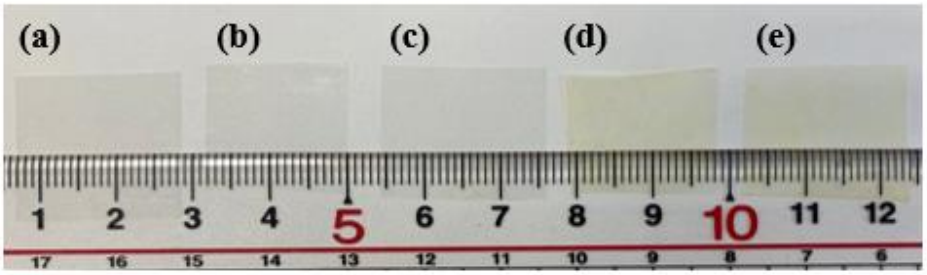


**Figure 7-1**. Images of the (a) PET, (b) PET film treated by sc-$CO_2$, (c) PET film treated by sc-$CO_2$ with $Pdhfa_2$, (d) $Pd(acac)_2$, and (e) $Pd(acac)_2$+ ε-caprolactam for 1 hr.

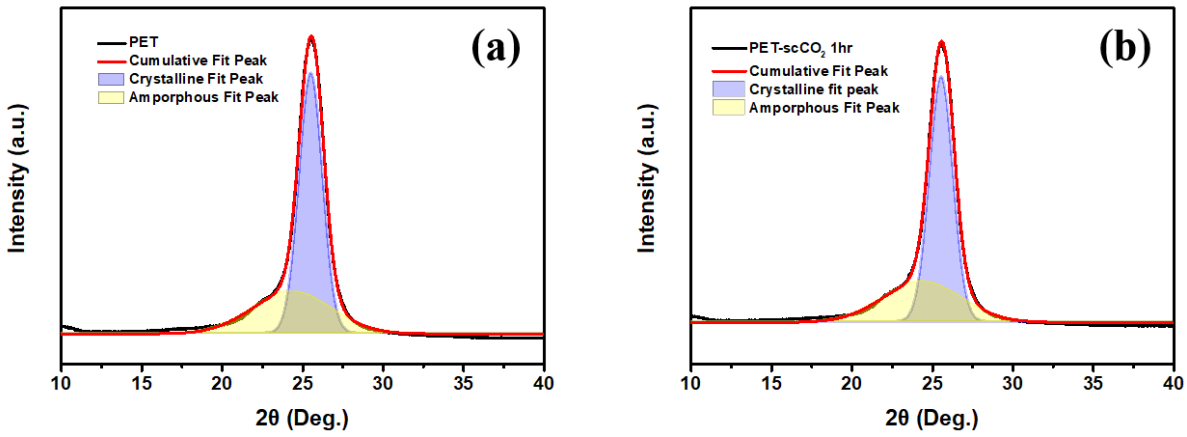


**Figure 7-2**. XRD patterns of the (a) PET film and the PET film treated by sc-$CO_2$ for (b) 1hr.

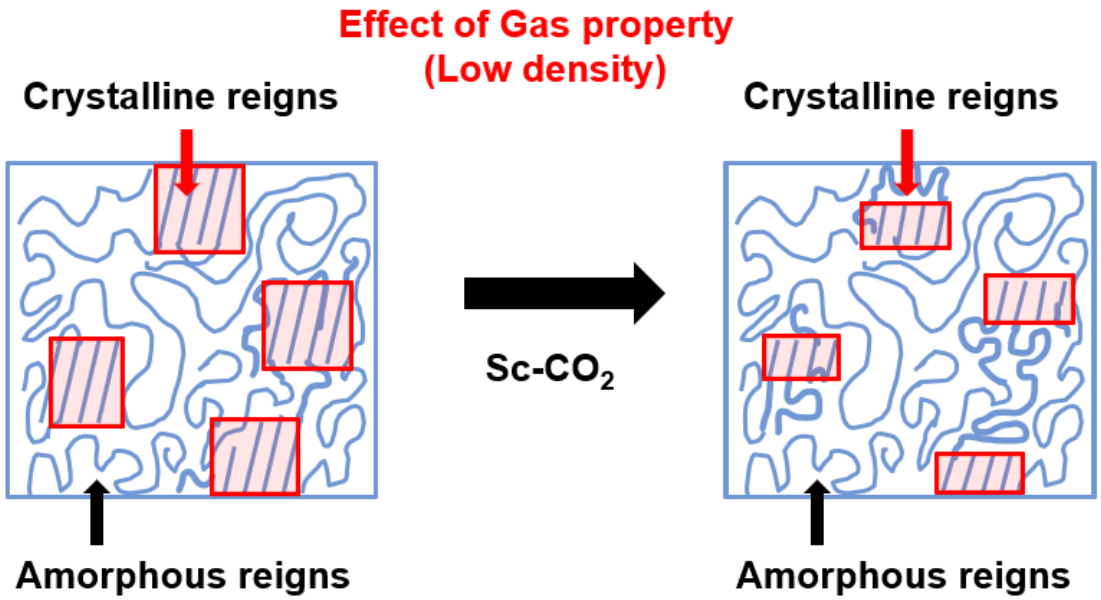


**Figure 7-3**. Transformation in the crystallinity of PET is induced by the gas-like property of sc-$CO_2$.

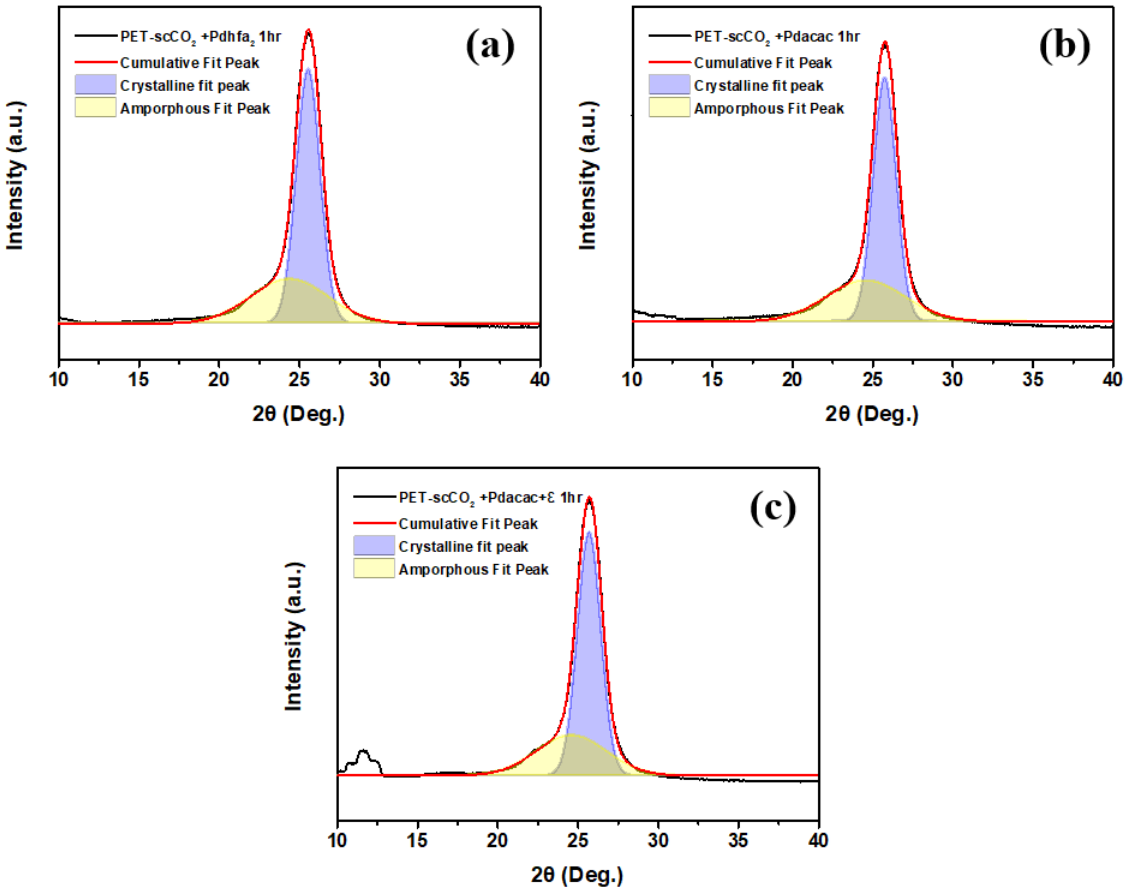


**Figure 7-4**. XRD patterns of the (a) PET film treated by sc-$CO_2$ with $Pdhfa_2$, (b) $Pd(acac)_2$, and (c) $Pd(acac)_2$+ ε-caprolactam for 1 hr.

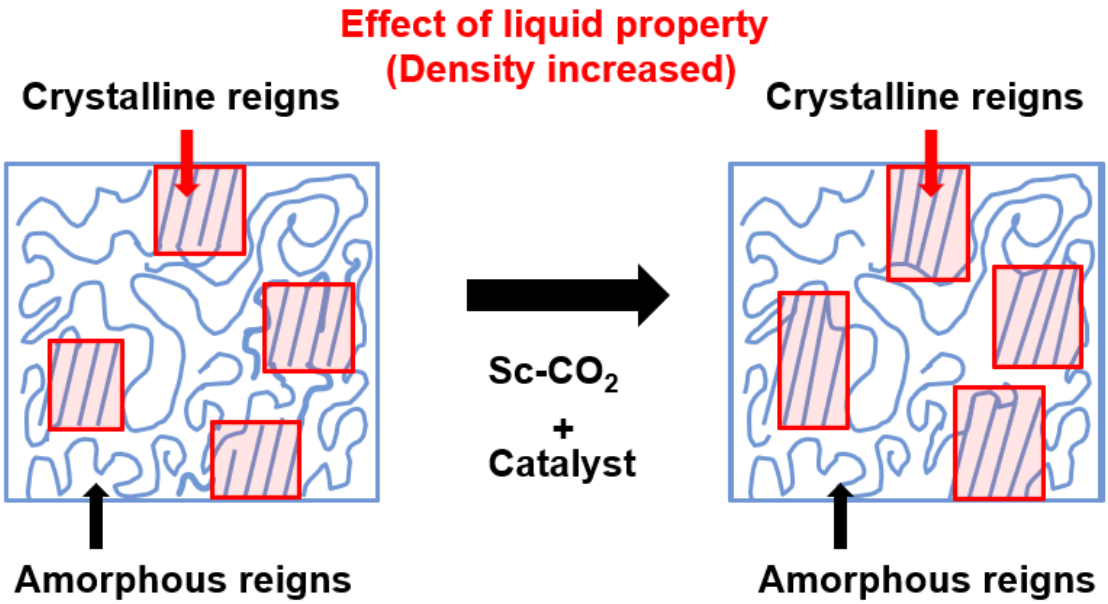


**Figure 7-5**. Transformation in the crystallinity of PET is induced by the liquid-like property of sc-$CO_2$.

CHAPTER 8

# *General conclusions*

## 8.1 Conclusions

In this thesis, effects of metallization of PET and 3D-printed polymer treated by the sc-$CO_2$ assisted electroless plating are investigated. Explanations on effects of the Sc-$CO_2$ in polymer substrates and selection in catalysts are provided. The electrical resistance, adhesion ability and tensile ability are evaluated to demonstrate the advantage in practical applications.

In chapter 2, Functionalization of PET films were achieved by an electroless plating process involving a sc-$CO_2$ catalyzation step to demonstrate the potential in preparation of flexible catalytic electrodes. Metallization of the PET catalyzed by conventional method was not successful. The sc-$CO_2$ catalyzation step was conducted in sc-$CO_2$ containing $Pd(hfa)_2$ as the source of the palladium catalyst for the later Ni-P deposition. The Ni-P layer was used as the sacrificial layer in deposition of the gold layer. By the sc-$CO_2$ catalyzation, the electrical resistance of the Ni-P/PET reached 0.27 Ω after 9.0 min of the Ni-P deposition time. The electrical resistance merely changed to 0.30 Ω after the tape adhesion test, which confirmed contributions of the sc-$CO_2$ catalyzation on the reliability of the Ni-P/PET composite. Gold was deposited on the Ni-P/PET composite

also by an electroless plating process, and the electrical resistance was lowered to 0.015 Ω after 60.0 min of the gold deposition. The catalytic activity of the Au/Ni-P/PET composites in oxidation of urea, ascorbic acid and glucose were confirmed, which demonstrate the potential as flexible catalytic electrodes in biosensors.

In chapter 3, Pt metallization of PET film was successfully achieved by electroless plating with the supercritical $CO_2$ catalyzation step. Sc-$CO_2$ functioned as the solvent, and Pd (II) acetylacetonate was used as the Pd catalyst source in the catalyzation step. The thickness of the Pt layer increased linearly as the Pt deposition increased from 30 min to 60 min. The Pt layer thickness reached 0.20 μm after 30 min of the metal deposition time, and the Pt layer thickened to 0.41 μm as the deposition time extended to 60 min. For the as-metallized Pt/PET with 30 min of the Pt deposition time, the electrical resistance was 0.95 Ω, and the electrical resistance reduced to 0.54 Ω as the Pt deposition time prolonged to 60 min. The thickened Pt layer was the main course of the reduced electrical resistance. For the Pt/PET with 60 min of the Pt deposition, the electrical resistance merely changed to 1.09 Ω after the tape adhesion test, and the fracture strength was at 65.9 MPa. The low electrical resistances before and after the adhesion test and the high tensile strength in the Pt/PET reported in this study all revealed advantages of the sc-$CO_2$ catalyzation step in development of biocompatible and flexible electronics.

In chapter 4, Metallization of 3D-printed polymer structures was achieved by sc-$CO_2$ assisted electroless plating process to demonstrate the potential for rapid fabrication of electronic components. The catalyzation step was conducted in sc-$CO_2$ with $Pd(hfa)_2$ as source of the Pd catalyst. Thickness of the metallized Ni-P reached 1.7 μm after 3 min of the metal deposition time, and the Ni-P layer thickened to 4.3 μm as the deposition time extended to 30 min. The electrical resistance reached 0.61 Ω after 3 min of metal

deposition time, and the resistance was lowered to 0.03 Ω after 30 min of the deposition time. After the tape adhesion test, electrical resistance of the Ni-P metallized 3D-printed polymer structure merely changed to 0.04 Ω for the sample with 30 min of the deposition time.

In chapter 5, Additive manufacturing of gold metallized 3D structures was demonstrated in this study. Complete gold metallization of the 3D printed structures was realized by sc-$CO_2$ assisted electroless plating. The sc-$CO_2$ was employed as a solvent to promote interaction between the Pd catalyst and surfaces of the 3D printed structures in the catalyzation step, and this eventually contributed to the complete gold metallization. Thickness of the gold layer reached 0.48 μm after 15.0 min of the gold deposition time, and the thickness was elevated to 1.23 μm as the gold deposition time increased to 45.0 min. The electrical resistance showed a negative correlation with the gold deposition time. The sample with 15.0 min of the gold deposition time showed the electrical resistance at 0.70 Ω, and it was reduced to 0.15 Ω when the gold deposition time was extended to 45.0 min. For the 45.0 min sample, the electrical resistance slightly worsened to 0.18 Ω. In addition, the strengthening was observed in the gold metallized samples, and the highest fracture strength was 47.6 MPa for the 45.0 min sample. In conclusion, the gold metallized 3D printed structures reported in this study are promising materials toward electronic components by the low electrical resistance, resistant again the tape adhesion test, and promoted tensile fracture strength.

In chapter 6, This study demonstrated the use of additive manufacturing for gold metallized circuit production, achieved through sc-$CO_2$ assisted electroless plating. By utilizing sc-$CO_2$ as a solvent, the Pd catalyst was able to effectively interact with the surfaces of the 3D printed structures during the catalyzation step, leading to complete

gold metallization. The roughness of the 3D-printed patterns was found to play a critical role, as the internal stress of Ni-P was leveraged to enhance the importance of roughness in adhesion. As a result, a selective pattern of gold metallization was achieved in a convenient and efficient process.

In chapter 7, The effect of sc-$CO_2$ treatment on the crystallinity of PET was investigated. The crystallinity of PET could be modified based on the properties of sc-$CO_2$. The density of sc-$CO_2$ close to gas tended to facilitate plasticization, resulting in an increase in the amorphous region. Conversely, the density of organometallic compounds dissolved in sc-$CO_2$, similar to liquid solvent, favored the induction of crystallization. The adjustment of PET crystallinity through sc-$CO_2$ treatment has important implications for its properties and applications. The presence of crystallinity in PET contributes to its metallization on the polymer. By controlling the density and properties of sc-$CO_2$, it becomes possible to tailor the crystallinity of PET to meet specific requirements.

# *Acknowledgements*

Three and a half years may seem like a long time, but looking back, it went by very quickly. Especially since I was constantly challenged and pushing myself to progress in all aspects, the journey was tough, but it was also the most enjoyable three and a half years of my academic career. Although I had already obtained a Master's degree in Taiwan, it was only after coming to Japan that I truly engaged in research and academic discussions and received excellent training in logical thinking. The greatest achievement I gained was in learning how to effectively present and describe my research, and how to explain my knowledge in a clear and concise manner. I would like to thank my past self who, despite feeling small and insignificant, refused to settle for the status quo. I hope to maintain this attitude and continue pushing boundaries in my future work.

First and foremost, I would like to express my deepest gratitude to Professor Masato Sone and Professor Tso-Fu Mark Chang for their guidance and continuous encouragement throughout the study. I am truly grateful to Professor Sone for giving me the opportunity to attend the prestigious Tokyo Institute of Technology, even though my performance during the interview might not be ideal three years ago. It was something that I never dared to dream of. During our breaks, he would often chat with us and join us for meals,

providing not only academic advice and encouragement, but also sharing his life experiences. I am truly thankful for his guidance and care. From now on, let me pick up the bill whenever we dine together in Taiwan. Professor Tso-Fu Mark Chang is a teacher whom I deeply admire. He excels in all aspects, including academia, language, and interpersonal relationships, and these are areas where I continue to strive for improvement. Whenever I discuss with him, he always points out my shortcomings and logical inconsistencies, which is invaluable guidance for me. I am truly grateful to have him as my teacher.

Dr. Shiah is not just a good friend, but also a big brother to me. We first met at NTUST, and he has been a constant source of help and encouragement throughout all the different stages of my life, even into my professional career. I am thrilled to join the same company as him, and I know I can count on him for support and guidance. Thank you for everything, and I look forward to continuing to work with you in the future.

Finally, I would like to express my gratitude to my family and girlfriend. Even though you may not have been able to help me directly, your unwavering support and encouragement have been the greatest help to me. I love you all, and I will do my best to take care of everything from now on.

*Po-Wei Cheng*

# *Appendix A List of achievements and others*

## A.1 Awards

- Taiwan Association for Coating and Thin Film Technology (TACT) 2021
  Best Poster Award
  *Nov. 2021*
- The 12th International Conference on Supercritical Fluids (Supergreen 2022)
  Best Oral Presentation Award
  *Nov. 2022*
- Interchange Association international student scholarship, Japan–Taiwan Interchange Association
  *Apr. 2022-Sep. 2023*
- Research Fellow, Institute of Innovative Research, Tokyo Tech
  *Sep. 2021-Mar. 2022*
- Tsubame Scholarship, Tokyo Tech
  *Sep. 2021-Mar. 2022*

## A.2 First author publications

### *A.2.1 International journal papers*

1. **P.-W. Cheng**, C.-Y. Chen, T. Ichibayashi, T.-F.M. Chang, M. Sone, S. Nishimura: Metallization of 3D-printed polymer structures via supercritical carbon dioxide-assisted electroless plating, MRS Commun. 11 (2021) 278-282.

2. **P.-W. Cheng**, C.-Y. Chen, T. Ichibayashi, T.-F.M. Chang, M. Sone, S. Nishimura: Supercritical Carbon Dioxide-Assisted Functionalization of Polyethylene Terephthalate (PET) toward Flexible Catalytic Electrodes, J. Supercritical fluids 180 (2022) 105455.
3. C.-Y. Chen, **P.-W. Cheng**, T. Ichibayashi, T.-F.M. Chang, Masato Sone, S. Nishimura. Metallization of 3D-Printed UV Photopolymer Structures by the Incorporation of Pd-Decorated Carbon Nanotubes. ACS Appl. Nano Mater. 6 (2023) 4584-4593.
4. **P.-W. Cheng**, T. Kurioka, C.-Y. Chen, T.-F.M. Chang, W.-T. Chiu, H. Hosoda, K. Takase, H. Ishihata, H. Kurosu, M. Sone: Platinum metallization of Polyethylene terephthalate by Supercritical Carbon Dioxide Catalyzation and the Tensile Fracture Strength, Materials 16 (2023) 2377.
5. **P.-W. Cheng**, T. Kurioka, C.-Y. Chen, T.-F.M. Chang, W.-T. Chiu, H. Hosoda, K. Takase, H. Ishihata, H. Kurosu, M. Sone: Supercritical Carbon Dioxide Assisted Gold Metallization of 3D Printed Structure and the Tensile Strength, MRS Commun.
6. (Under review) **P.-W. Cheng**, T. Kurioka, C.-Y. Chen, W.-T. Chiu, K. Tokuoka, M. Sano, M. Sone T.-F.M. Chang: エレクトロニクス部品設計のための超臨界二酸化炭素を利用した金属堆積技術，日本金属学会誌

*A.2.2 International conferences*

1. **P.-W. Cheng**, C.-Y. Chen, T. Ichibayashia, T.-F.M. Chang, M. Sone, S. Nishimura: Supercritical Carbon Dioxide Assisted Metallization of 3D-Printed Polymer Structure as Functional Components in Electronic Devices, The 2021 International Thin Film Conference (TACT 2021), November 15-18, 2021 [Poster]. *Best Poster Award
2. **P.-W. Cheng**, C.-Y. Chen, T. Ichibayashia, T.-F.M. Chang, M. Sone, S. Nishimura: Metallization of 3D Printed Polymer Structures via Supercritical Carbon Dioxide

Assisted Electroless Plating, Taiwan Supercritical Fluid Association, December 11, 2021[Oral].

3. **P.-W. Cheng**, C.-Y. Chen, T. Ichibayashia, T.-F.M. Chang, M. Sone, S. Nishimura: Supercritical Carbon Dioxide Assisted Electroless Plating of 3D-Printed Polymer Structure, The 2021 International Chemical Congress of Pacific Basin Societies (Pacifichem 2021), December 16-21, 2021 [Poster].
4. **P.-W. Cheng**, T. Kurioka, C.-Y. Chen, Y. Jiang, W.-T, Chiu, M, Tahara, H, Hosoda, T. Ichibayashia, S. Nishimura, M. Sone, T.-F.M. Chang: Tensile Strength of Pt Metallized Polyethylene terephthalate (PET) by Supercritical CO2-assisted Metallization for Design of Flexible Electronic Components, 48th International Conference on Micro and Nano Engineering, September 19-23, 2022 [Poster].
5. **P.-W. Cheng**, C.-Y. Chen, Tomoyuki Kurioka, M. Sone, T.-F.M. Chang: Supercritical carbon dioxide functionalization of polyethylene terephthalate (PET) for flexible biosensors, 12th International Conference on Supercritical Fluids (Supergreen 2022), October 29, 2022 [Oral]. *Best Oral Presentation Award.